The ^{3}H(α,γ)^{7}Li Reaction at Low Energies

Thesis by
Carl Richard Brune

In Partial Fulfillment of the Requirements
for the Degree of
Doctor of Philosophy

California Institute of Technology
Pasadena, California

1994
(Submitted 17 May, 1994)

Acknowledgments

I would like to thank the faculty, staff, and students of Kellogg Radiation Laboratory for creating a productive and enjoyable environment for carrying out research. Particularly, I would like to thank Ralph Kavanagh, my advisor, for his guidance, support and assistance. His knowledge and confidence were especially important for undertaking the tritium-target fabrication at Caltech. It was a pleasure to collaborate with Claus Rolfs in the early stages of this experiment. I have benefited from several enlightening discussions with Charles Barnes and Karlheinz Langanke.

My work would not have been as productive or enjoyable, were it not for my colleagues in the sub-basement: Steve Kellogg, T. R. Wang, Michael Smith, Patricia Wrean, and Kevin Hahn. I would also like to acknowledge the technical contributions of several people: Bob Carr, for maintaining the accelerator, and assistance designing equipment; Pat Huber, for help with the computer systems; Al Massey, for his electronics expertise; Jim Pendlay, for fixing things that broke, and also for teaching me AutoCAD; Jack Richards, for his work in the machine shop; and Dick Azuma, for supplying the titanium-tritide targets used in the preliminary phase of this work.

I would like to thank my parents, who throughout my life have been a constant source of encouragement. I am grateful to my wife Roxanne, for all of her love and support.

Financial support for this work was provided in part by the National Science Foundation, Grant Numbers PHY88-17297 and PHY91-15574.

Abstract

The absolute cross section of the ^{3}H$(\alpha,\gamma)^7$Li reaction has been measured for $50 \leq E_{c.m.} \leq 1200$ keV. Specially prepared Ti–^{3}H targets were bombarded with an α^+ beam, and γ rays were detected using an 85% high-purity germanium detector. Total S-factors and the branching ratios for radiative capture to the two final bound states are reported for the entire energy range. Angular distributions of the capture γ rays were measured for nine energies in the range $115 \leq E_{c.m.} \leq 1200$ keV. Legendre coefficients extracted from fits to the angular distributions are also reported. The preparation and characterization of the radioactive Ti–^{3}H targets are discussed.

This experiment is motivated by models of big-bang nucleosynthesis, which require the ^{3}H$(\alpha,\gamma)^7$Li reaction rate for computing the primordial ^{7}Li abundance. Our results have considerably smaller uncertainties and reach lower energies than previous experiments. For $E \leq 150$ keV, we find the S-factor to be considerably smaller than indicated by previous experiments. The measured branching ratio is found to be approximately energy independent, with a value of 0.45. The energy dependence of the measured S-factors is in agreement with existing theoretical calculations. The new results are used to calculate the thermonuclear reaction rate for temperatures below 10 GK.

Contents

List of Tables

List of Figures

Chapter 1

Introduction

Observational evidence supporting the big-bang model of the universe comes primarily from four sources: (1) the Hubble expansion, (2) the age of the universe, (3) the cosmic microwave background radiation, and (4) the relative abundances of the light elements ^{1}H, ^{2}H, ^{3}He, ^{4}He, and ^{7}Li. The role of ^{7}Li in the big bang, and in particular its synthesis via the ^{3}H$(\alpha,\gamma)^7$Li reaction, is the primary motivation for this thesis. We describe laboratory measurements of the ^{3}H$(\alpha,\gamma)^7$Li cross section, at energies relevant for big-bang nucleosynthesis.

1.1 Big-Bang Cosmology

An important cosmological quantity is the critical density,

$$\rho_c = \frac{3H_0^2}{8\pi G}, \tag{1.1}$$

where H_0 is the Hubble constant and G is the gravitational constant. The density parameter Ω is defined by

$$\Omega = \frac{\rho}{\rho_c}, \tag{1.2}$$

where ρ is present density of the universe. The cases $\Omega > 1$, $\Omega = 1$, and $\Omega < 1$ correspond to a closed universe (which will eventually recontract), a flat universe (which will expand forever), and an open universe (which will expand forever), respectively. Models of inflationary cosmology predict an $\Omega = 1$ universe. Clearly, a firm observational determination of Ω would be very interesting, but this has proven very difficult. Observations of luminous matter find $\Omega_{LUM} \approx 0.01$ or less, but other determinations (for example the matter distribution inferred from the IRAS survey) indicate values up to $\Omega \approx 1$ [Kol90].

The first big-bang nucleosynthesis calculations were made by Alpher, Bethe, and Gamow [Alp48], who assumed only neutrons for the initial state. Hayashi [Hay50] pointed out that neutrons and protons will be in statistical equilibrium for sufficiently high temperatures and densities. Further refinements were made by Alpher, Follin and Herman [Alp53] and Hoyle and Tayler [Hoy64]. The discovery of the cosmic microwave background at ≈ 3 K in 1965 by Penzias and Wilson [Pen65] provided incentive for further calculations. Peebles [Pee66] and Wagoner, Fowler and Hoyle [Wag67] made detailed calculations of the resulting light-element abundances. Since this time the input data have undergone much improvement, but the essential physics has remained unchanged. Recent standard big-bang reviews have been published by Krauss and Romanelli [Kra90], Riley and Irvine [Ril91], Walker *et al.* [Wal91], and Smith, Kawano, and Malaney [Smi93].

Primordial-nucleosynthesis calculations provide some stringent tests of several of the assumptions underlying the standard big-bang model. A wide selection of variant models has been reviewed by Malaney and Mathews [Mal93]. Considerable recent attention has been focussed on the "inhomogeneous big-bang models," which take into account the effects of baryon-density inhomogeneity resulting from a phase transition (or transitions) in the early universe (for example, the quark-hadron transition). In the remainder of this Section we outline several aspects of standard big-bang nucleosynthesis.

Standard calculations assume the correctness of general relativity, and the homogeneity and isotropy of space. Important input data include the known particles (e.g., three neutrino species), nuclear reaction rates, and the neutron lifetime (used

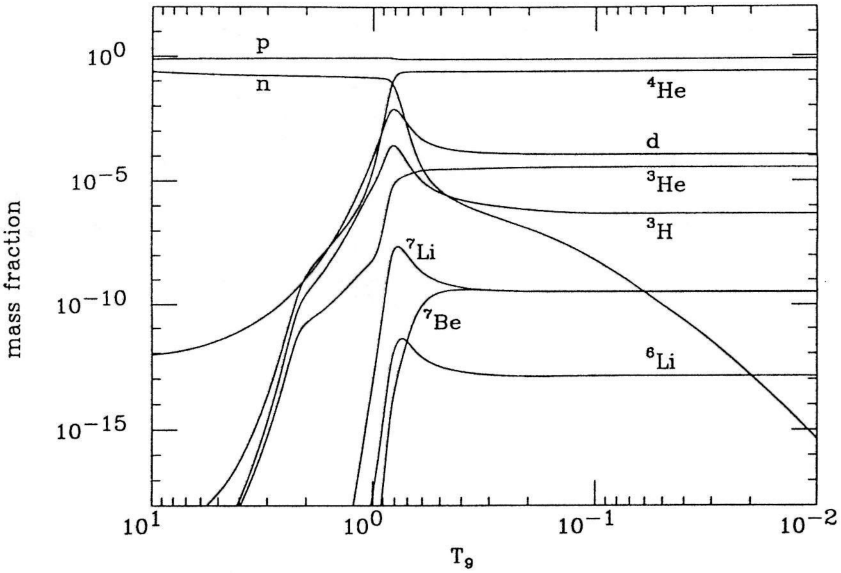

Figure 1.1: Evolution of the light-element abundances with temperature (measured in GK) in the big bang, for $\eta_{10} = 3.0$.

to determine the rates for weak $n \leftrightarrow p$ processes). The present number density of background photons, n_γ, can be determined from the measured temperature of the background radiation ($T_\gamma = 2.736 \pm 0.017$ K [Gus90]) using

$$n_\gamma = 16\pi\zeta(3)\left(\frac{kT_\gamma}{hc}\right)^3, \tag{1.3}$$

where $\zeta(3) = 1.20206$. The ratio of baryons to photons, $\eta = n_B/n_\gamma$, is expected to have been constant since $e^+ - e^-$ annihilation [Kol90]. The calculated abundances are normally presented as a function of η, the only free parameter in the standard big-bang model. The baryon density parameter Ω_B can be calculated from T_γ and η using Equations 1.1–1.3; however, the present factor of two uncertainty in H_0 introduces a factor of four uncertainty in Ω_B.

A sample calculation for $\eta_{10} = 3.0$ is shown in Figure 1.1 ($\eta_{10} \equiv 10^{10}\eta$). This calculation and the one shown in Figure 1.3 were made using Kawano's nucleosynthesis program [Kaw92], with reaction rates from Caughlan and Fowler [Cau88], and a neutron lifetime of 888.5 sec. It is seen that the big bang produces mostly ^{1}H, with some ^{4}He (about 25% by mass), and traces of other isotopes. Note that the radioactive isotopes ^{3}H and ^{7}Be decay eventually to ^{3}He and ^{7}Li.

Walker *et al.* found that the calculated abundances of ^{2}H, ^{3}He, and ^{7}Li (relative to ^{1}H) agreed with observations for

$$2.8 \leq \eta_{10} \leq 4.0, \tag{1.4}$$

corresponding to

$$0.01 \leq \Omega_B \leq 0.10. \tag{1.5}$$

The ^{4}He abundance is only weakly dependent upon η. Including the uncertainties in η (Equation 1.4) and the neutron lifetime, Walker *et al.* found the calculated ^{4}He mass fraction, Y_p, to be bounded by

$$0.236 \leq Y_p \leq 0.243, \tag{1.6}$$

in good agreement with the observational value $Y_p^{obs} = 0.23 \pm 0.01$. Understandably, the observational determinations of the abundances of less common isotopes are more difficult, and have larger uncertainties. The reader is referred to the recent reviews [Kra90, Ril91, Wal91, Smi93] for detailed comparisons between observation and calculation. The arguments supporting the observational determination of the primordial ^{7}Li abundance are outlined in the following paragraph.

The "lithium plateau" in metal-poor halo stars was discovered in 1982 by Spite and Spite [Spi82]. Over a wide range of temperatures they found a constant Li abundance, $[\mathrm{Li}] \approx 2.0$, where $[\mathrm{Li}] \equiv 12 + \log_{10}(\mathrm{Li/H})$. Their work has subsequently been confirmed by many observers; data from several sources have been compiled by Walker *et al.*, and are displayed in Figure 1.2. The data set has been restricted to very metal-poor stars, $[\mathrm{Fe/H}] \leq -1.3$, where $[\mathrm{Fe/H}] \equiv \log_{10}(\mathrm{Fe/H})_* - \log_{10}(\mathrm{Fe/H})_\odot$. The stars with effective temperature $T_{eff} > 5500$ K show a constant Li abundance. The spread in the data appears to be consistent with the observational errors, although there may be some evidence for underlying dispersion [Del93]. The observed Li is

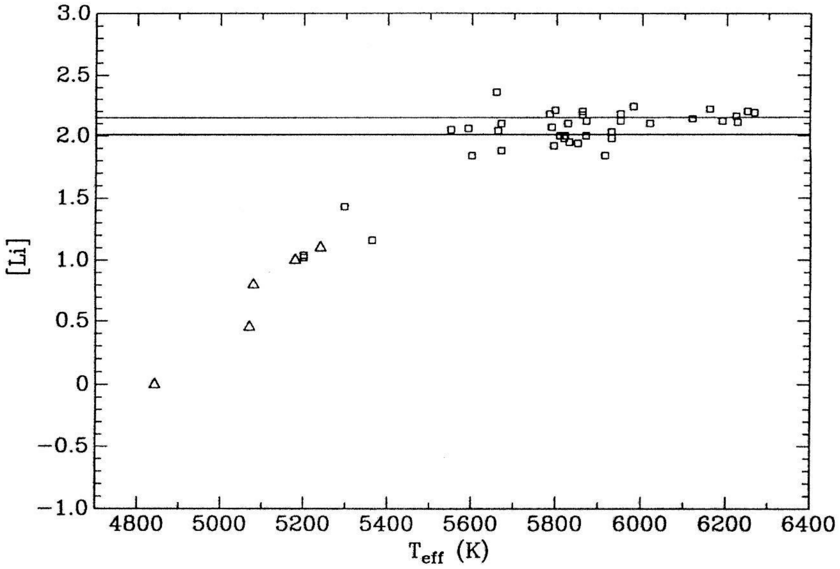

Figure 1.2: Observed Li abundance versus T_{eff}, for the most metal-poor stars ([Fe/H] ≤ -1.3). The diamonds are upper limits to [Li]. The horizontal lines correspond to Equation 1.7. (Adapted from Walker *et al.* [Wal91].)

believed to be essentially ^{7}Li [Spi82, Reb88]; also note that the calculated big-bang ^{6}Li yield is predicted to be negligible compared to ^{7}Li (Figure 1.1). The observed plateau supports the hypothesis that the abundance of Li in halo stars (Population II) is of primordial origin. Using stars with $T_{eff} > 5500$ K, Walker *et al.* find a mean value of

$$[\mathrm{Li}] = 2.08 \pm 0.07, \tag{1.7}$$

where the error represents a 2σ uncertainty. This 2σ range is shown as horizontal lines in Figures 1.2 and 1.3. A larger range, $2.04 \leq [\mathrm{Li}] \leq 2.36$, has been derived by allowing for some depletion during stellar evolution [Del89].

The ^{7}Li abundance calculated as a function of η is shown in Figure 1.3. The separate contributions of ^{7}Li and ^{7}Be are shown as dashed lines. The calculated abundance agrees with the observations (horizontal lines) only for a narrow range of η, consistent with Equation 1.4. (Note that Equation 1.4 allows for some uncertainty in the reaction rates.) It is seen that ^{7}Li production dominates for $\eta_{10} \lesssim 3$, while ^{7}Be dominates for $\eta_{10} \gtrsim 3$. It is interesting to note that the observed ^{7}Li abundance

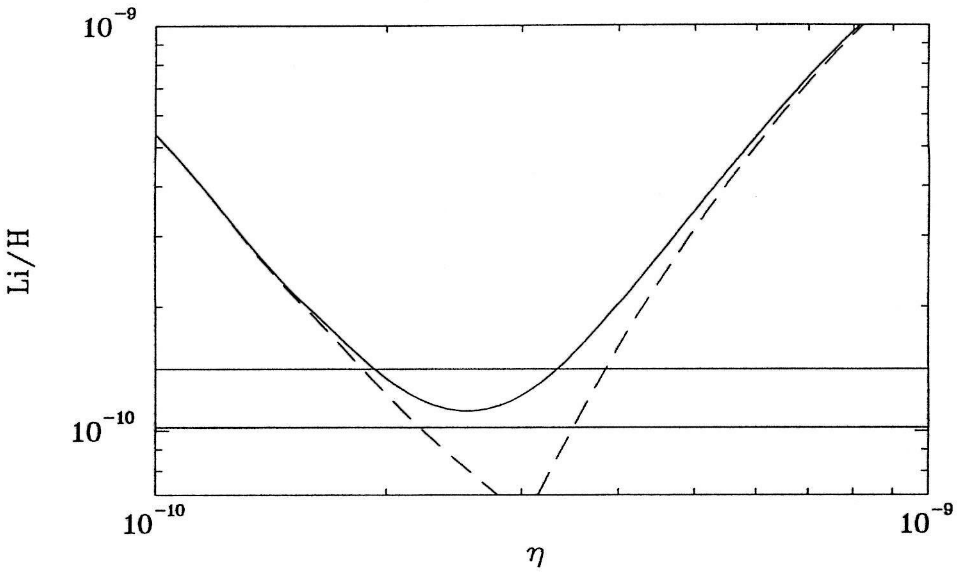

Figure 1.3: Calculated ^{7}Li abundance as a function of the baryon-to-photon ratio η (solid curve). The dashed curves on the left and right show the separate contributions of ^{7}Li and ^{7}Be, respectively. The horizontal lines correspond to limits on the ^{7}Li abundance from observations (Equation 1.7).

coincides with the minimum in the calculated abundance at $\eta_{10} \sim 3$ (this minimum is absolute for at least $0.1 \leq \eta_{10} \leq 100$; see Figure 12 of Walker *et al.*).

The two-body thermonuclear reaction rate $N_A\langle\sigma v\rangle$ used in astrophysical calculations is calculated from the cross section σ using [Fow67]

$$N_A\langle\sigma v\rangle = \left(\frac{8}{\pi\mu}\right)^{1/2} \frac{N_A}{(kT)^{3/2}} \int_0^\infty E\,\sigma(E)\exp\left(-\frac{E}{kT}\right) dE, \tag{1.8}$$

where N_A is Avogadro's number, μ is the reduced mass in the entrance channel, k is Boltzmann's constant, T is temperature, and E is the center-of-mass energy. The uncertainties in the abundance calculations arising from nuclear-data input have been studied in detail by Krauss and Romanelli [Kra90] and Smith, Kawano, and Malaney [Smi93]. Smith, Kawano, and Malaney have identified 12 reactions which significantly affect light-element production in the big-bang; all of these reactions were found to affect ^{7}Li production. Of the 12, ^{3}H$(\alpha,\gamma)^7$Li is by far the most uncertain; the authors estimated a 2σ uncertainty of up to 55% in the cross section. Note also

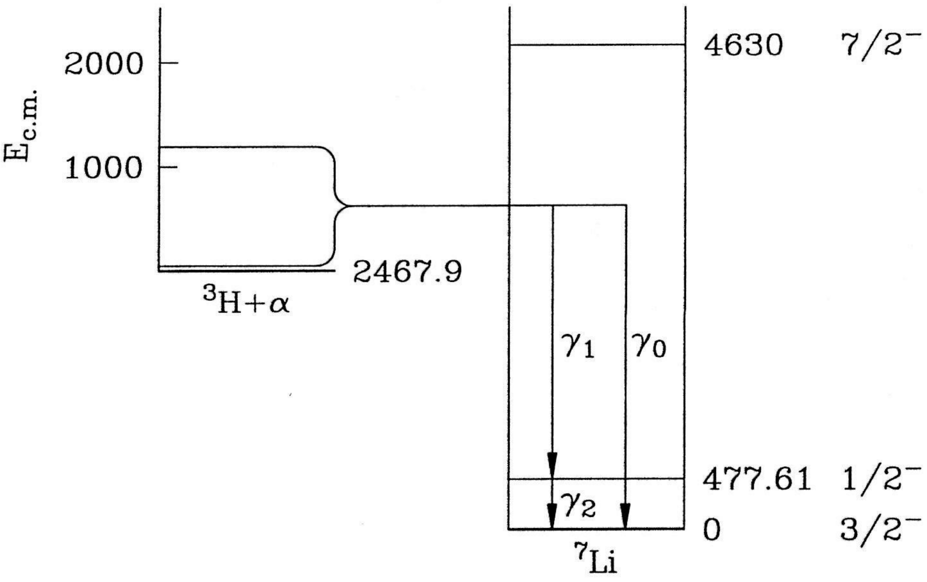

Figure 1.4: ^{7}Li energy level diagram (all energies are given in keV).

that ^{3}H$(\alpha,\gamma)^7$Li is most important for $\eta_{10} \lesssim 3$, as ^{7}Be production dominates at higher η.

An investigation of the sensitivity of the abundance calculations to the ^{3}H$(\alpha,\gamma)^7$Li rate is presented in Appendix A. We find that calculated ^{7}Li abundance is sensitive to $N_A\langle\sigma v\rangle$ for $0.1 \lesssim T_9 \lesssim 0.6$, where T_9 is the temperature in GK. These temperatures provide guidance as to what energies in Equation 1.8 are important for determining the big-bang ^{7}Li yield, as discussed below.

1.2 Nuclear Physics

The energy-level diagram for ^{7}Li is shown in Figure 1.4. The ^{3}H$(\alpha,\gamma)^7$Li reaction proceeds by γ emission to the two bound states: the $\frac{3}{2}^-$ ground state (γ_0) or the $\frac{1}{2}^-$ first excited state (γ_1). The first excited state decays by γ emission (γ_2) to the ground state. The (α,γ) cross section is expected to be non-resonant for $E <$ 2100 keV, since there is no energy level between the first excited state and the $\frac{7}{2}^-$ state ($\Gamma_{c.m.} = 93 \pm 8$ keV [Ajz88]) at 4630 keV. The next channel, ^{6}Li$+n$, opens at an excitation energy of 7250 keV. In this work, energies without a subscript label refer to the center-of-mass system.

At low energies, the reaction cross section for charged particles is conveniently parameterized in terms of the S-factor $S(E)$, defined by

$$\sigma(E) = \frac{S(E)}{E} \exp\left(-\sqrt{\frac{E_G}{E}}\right), \tag{1.9}$$

where E_G is the Gamow energy,

$$E_G = 2\pi^2 Z_1^2 Z_2^2 \alpha^2 \mu, \tag{1.10}$$

and Z_1 and Z_2 are the charges of the reacting nuclei, α is the fine-structure constant, and μ is reduced mass (in energy units) of the reacting nuclei (E_G = 6735.0 keV for $^3\text{H} + \alpha$). This parameterization removes two energy-dependent factors: the de Broglie wavelength factor $1/E$ and the (approximate) Coulomb-barrier penetration factor $\exp(-\sqrt{E_G/E})$. The S-factor for a non-resonant reaction such as $^3\text{H}(\alpha,\gamma)$ is expected to be a slowly varying function of energy.

The partial S-factors S_i for the $^3\text{H}(\alpha,\gamma)$ reaction are calculated from the cross sections σ_i for producing γ_i, where i = 0, 1, or 2. Note that S_1 equals S_2 since the first excited state always decays by γ emission. The total S-factor $S = S_0 + S_1$ is the important quantity for astrophysics since it determines the fusion rate for $^3\text{H} + {}^4\text{He} \rightarrow {}^7\text{Li}$. The cross sections σ_i then determined by S and the branching ratio $R = \sigma_1/\sigma_0$.

For constant $S(E)$, the integrand in Equation 1.8 peaks at

$$E_0 = E_G^{1/3}\left(\frac{kT}{2}\right)^{2/3} \tag{1.11}$$

and has an approximate $1/e$ width

$$\Delta = 4\left(\frac{E_0 kT}{3}\right)^{1/2}. \tag{1.12}$$

The temperature range $0.1 \lesssim T_9 \lesssim 0.6$ found above corresponds to $50 \lesssim E_0 \lesssim 165$ keV. For $T_9 = 0.1$, $\Delta = 48$ keV, and for $T_9 = 0.6$, $\Delta = 213$ keV. Thus knowledge of the ^{3}H$(\alpha,\gamma)^7$Li cross section over the range $25 \lesssim E \lesssim 270$ keV is most important for the standard big bang. We will not confine our interest to this range, as alternative big-bang models may have different requirements. Measurements over a wide range of energies are also useful for testing theoretical calculations. While most of the energy range can be covered by laboratory measurements, energies as low as 25 keV will require some extrapolation of the experimental data, so a validation of the theoretical extrapolation is valuable.

1.2.1 Previous Experiments

Direct Measurements

The first measurements of the ^{3}H(α,γ) reaction were reported in 1959 by Holmgren and Johnston [Hol59]. The experiment was performed using ^{3}H-filled gas cell which was bombarded though a Ni entrance foil by an α beam. The γ rays were detected using an NaI scintillator. The experiment covered the range $200 \leq E \leq 560$ keV, and claimed to achieve 30% precision. The measured values of S varied between $S(200\text{ keV}) = 0.040$ and $S(560\text{ keV}) = 0.023$ keV-b. The ^{3}H areal density was determined by measuring the absolute pressure in the gas cell.

Improved measurements were made by Griffiths *et al.* [Gri61], who bombarded solid Zr–^{3}H targets with an α beam, and again detected γ rays with a NaI scintillator. The measurements covered $150 \leq E \leq 780$ keV, with an estimated error in S of 20-25%. Their results for S and R are reproduced in Figure 1.5. The results for S were a factor of 2 to 2.5 higher than found by Holmgren and Johnston; within the accuracy of the measurement, S was found to be constant with a mean value of 0.064 keV-b. From the γ_0 and γ_1 yields, the branching ratio was found to be independent of angle (within 5%) and approximimately independent of energy, with an average value of $R \approx 0.40$. The separation of γ_1 from γ_0 required the use of a lineshape fit to the NaI spectra,

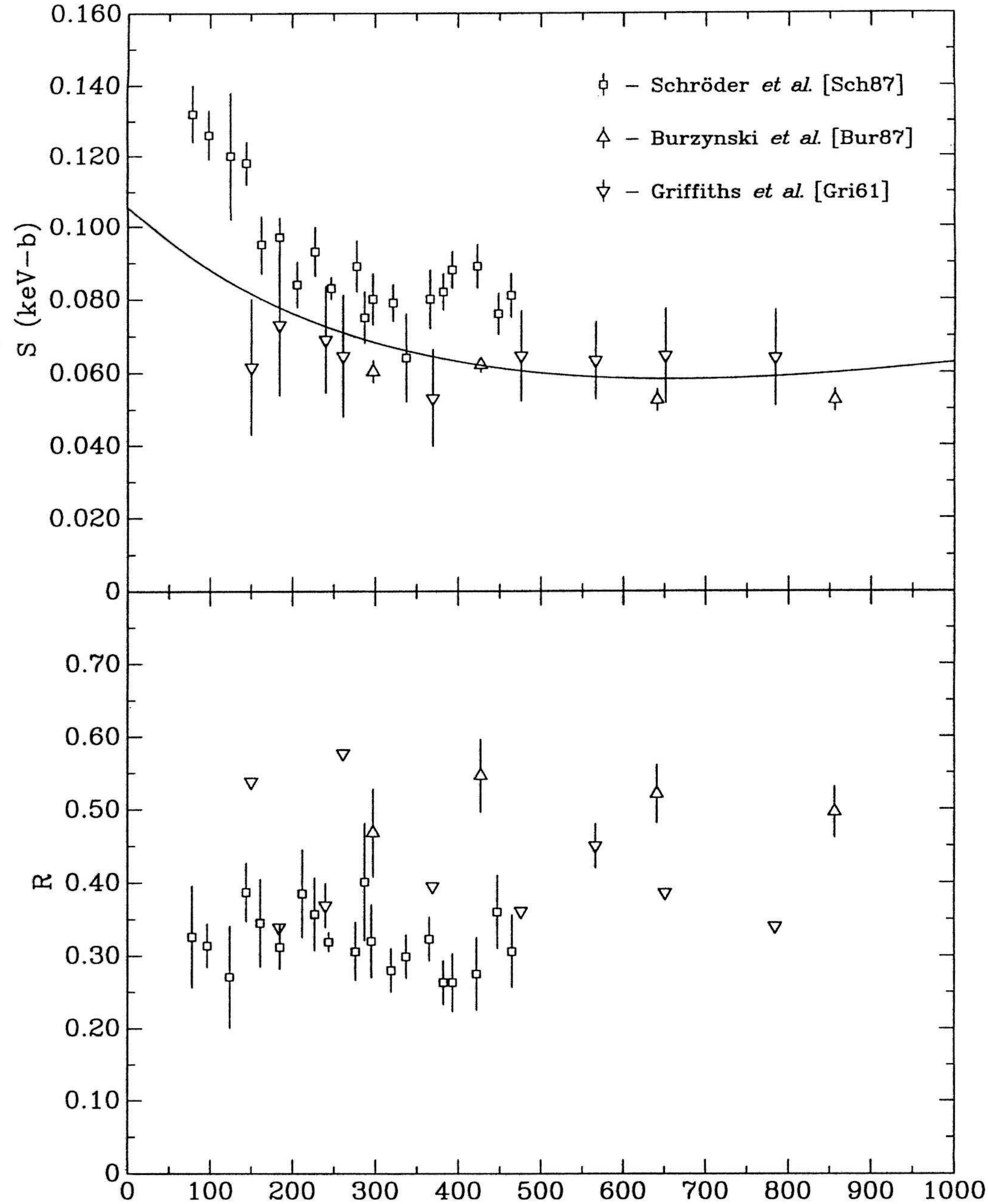

Figure 1.5: The previous results [Sch87, Bur87, Gri61] for S and R as a function of the center-of-mass energy E. The errors on the S data points of Schröder *et al.* and Burzynski *et al.* do not include respective systematic errors of 15% and 14%. Griffiths *et al.* only quoted uncertainties for a few R data points. The solid curve in the upper panel is Equation 1.16, normalized to $S(500\text{ keV}) = 0.060$ keV-b.

due to the proximity of γ_1 to the γ_0 first-escape peak in the NaI spectrum. Two measurements of the γ_0 angular distribution were also reported: relative intensities at 0° and 90° (angles relative to the incident-beam direction) were determined for $E = 241$ keV, and relative intensities at 0°, 45°, 90°, and 135° were determined for $E = 567$ keV. The ^{3}H areal density was determined by measuring the $^3\mathrm{H}(p,\gamma)$ yield at $E_p = 800$ keV, and using the (p,γ) cross section found by Perry and Bame [Per55].

Two new measurements have been reported in the late 1980's, undertaken as a result of the importance of $^3\mathrm{H}(\alpha,\gamma)$ for big-bang nucleosynthesis. The new measurements were improved by using thinner Ti–^{3}H targets and by detecting γ rays with solid-state Ge detectors. The primary advantage of Ge detectors is the greatly improved γ-ray energy resolution, which allows the γ-ray lines of interest to be unambiguously separated from various background sources, with a much improved signal-to-noise ratio. The γ_1 line is separated from the troublesome γ_0 first-escape peak by ≈ 33 keV under ideal circumstances. The experimental resolution for these peaks is determined by three factors: (1) resolution in the center-of-mass energy, (2) energy spread from angle-dependent Doppler shift, and (3) detector resolution (≈ 3 keV at $E_\gamma = 3$ MeV for Ge detectors). The use of thinner targets reduces the amount of energy lost by the beam in the target, and hence the energy resolution in the $^3\mathrm{H} + \alpha$ center of mass. The improved center-of-mass resolution also reduces the error in the determination of the effective reaction energy. The determination of the effective energy at low energies is very important due to the strong energy dependence of the cross section. Using Equation 1.9 and neglecting the energy dependence of $S(E)$ one finds

$$\frac{1}{\sigma}\frac{d\sigma}{dE} = \frac{1}{E}\left(-1 + \frac{1}{2}\sqrt{\frac{E_G}{E}}\right). \tag{1.13}$$

For example, a 1-keV error in E at $E = 100$ keV translates to a 3% error in σ (or S).

Measurements for $79 \leq E \leq 464$ keV were published by Schröder *et al.* in 1987. The results for S and R are shown in Figure 1.5; the errors on the S data points do not include an additional 15% systematic uncertainty. The results for S show a significant increase with decreasing energy (in contrast with the data of Griffiths *et* *al.*); the authors estimated $S(0) = 0.14 \pm 0.02$. Using γ_0 and the weighted average of γ_1 and γ_2, the branching ratio was found to be independent of energy with an average value of 0.32 ± 0.01, a significantly lower result than that found by Griffiths *et al.* Angular distribution measurements showed the yield to be isotropic (within 20% [Rol91]). The reported results were based upon 0° data, analyzed assuming isotropy. The effective reaction energy was determined using the measured γ_0 energy. The ^{3}H areal density was determined in a manner similar to that of Griffiths *et al.*, by measuring the $^3\mathrm{H}(p,\gamma)$ yield at $E_p = 1000$ keV and using the (p,γ) cross section of Perry and Bame.

Also reported in 1987 was the experiment of Burzynski *et al.* [Bur87], over the energy range $297 \leq E \leq 856$ keV. The results for S and R are shown in Figure 1.5; the errors in S do not include an additional 14% systematic error. Using γ_0 and γ_1, the branching ratio was found to be energy independent, with an average value of 0.51 ± 0.04. The measurements were performed at 0°; the $E < 500$-keV data were analyzed assuming isotropy, and the $E > 500$-keV data were analyzed using the angular distribution found by Griffiths *et al.* at $E = 567$ keV. The ^{3}H areal density was determined by measuring the 90° $^3\mathrm{H}(d,n)$ yield at $E_d = 1000$ keV and using the known (d,n) differential cross section. While this technique should be reliable, it could give misleading results if there is any ^{3}H distributed in the backing of the target, as has been encountered previously in our laboratory [Bru91].

The agreement between the measurements of S over the range of their mutual overlap is reasonable if the systematic errors are taken into account (not including the early results of Holmgren and Johnston). However, only the experiment of Schröder *et al.* reaches the low energies needed to determine big-bang ^{7}Li production. The disagreement between the various branching-ratio measurements (results vary between 0.25 and 0.55) is rather puzzling.

Another disturbing development is the new measurement by Feldman *et al.* [Fel90] of the $^3\mathrm{H}(p,\gamma)$ cross section used by Griffiths *et al.* and Schröder *et al.* to determine the ^{3}H areal density of their targets. The new data cover $2 \leq E_p \leq 15$ MeV, and

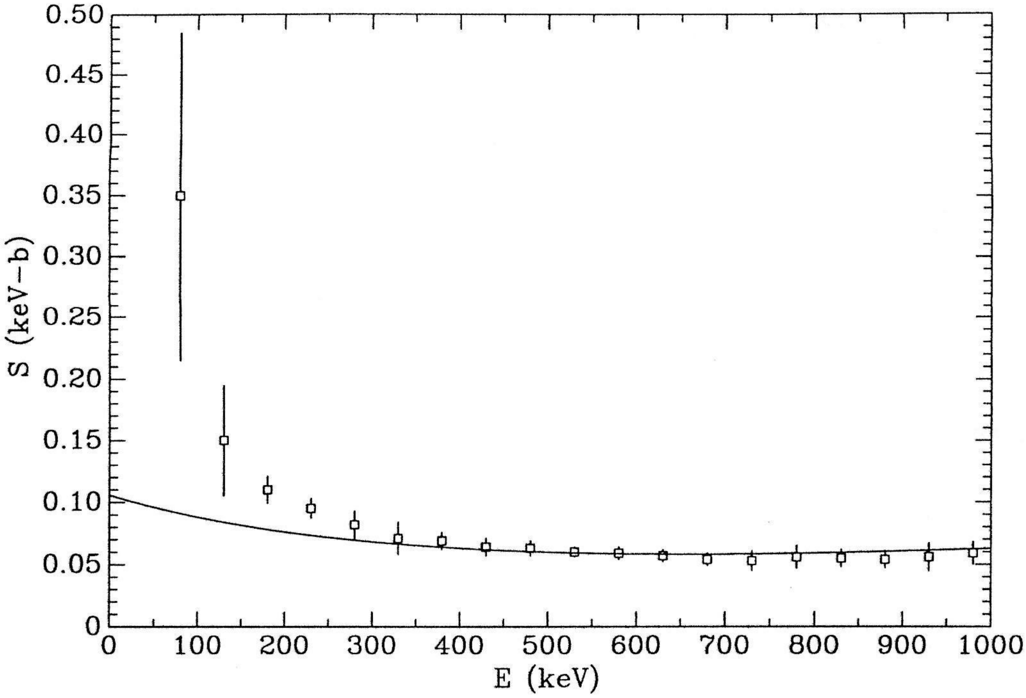

Figure 1.6: The Coulomb dissociation results of Utsunomiya *et al.* [Uts90]. The solid curve is Equation 1.16, normalized to $S(500 \text{ keV}) = 0.060$ keV-b. Note that the vertical scale has been expanded compared to Figure 1.5.

are $\approx$ 30% lower than the cross sections found by Perry and Bame (who quoted an uncertainty of 7%). The ramifications of this measurement for the absolute normalization of the Griffiths *et al.* and Schröder *et al.* S-factors are not clear, as the new measurement has not been independently confirmed, and it only covers higher energies than used in the (α,γ) experiments. A possible systematic error in the NaI scintillator efficiency used by Perry and Bame is discussed by Griffiths *et al.*

Coulomb Dissociation Measurements

The Coulomb dissociation approach for determining radiative capture cross sections for reactions of the type $a+b \rightarrow c+\gamma$ has recently received much attention. The basic idea is to study the inverse reaction, $c + \gamma \rightarrow a + b$, by bombarding a target with a beam of c, and using the Coulomb field of the target nuclei as the source of (virtual) photons. The relative energy in the $a + b$ center of mass must be reconstructed from the detected momenta of a and b. For example, the $^{3}\text{H}(\alpha,\gamma)^{7}\text{Li}$ cross section could perhaps be determined by measuring the $^{208}\text{Pb}(^{7}\text{Li},\alpha^{3}\text{H})^{208}\text{Pb}$ breakup cross section. The practical advantage of the Coulomb dissociation approach appears to be that the event rate is significantly higher than for radiative-capture experiments, under realistic experimental conditions. The realization of this advantage largely remains to be seen, as only a few experiments have been performed to date, and experimental techniques have not been optimized. The approach can also provide access to reactions for which radiative-capture experiments are very difficult, for example due to the presence of a short-lived isotope in the entrance channel. The Coulomb dissociation technique can necessarily only give information about radiative capture to the ground states of nuclei.

Several theoretical issues complicate the use of the Coulomb dissociation method. Coulomb breakup dominates over nuclear breakup only for high incident energies and very forward scattering angles. Bertulani and Hussein [Ber90] suggest that bombarding energies of $\approx$ 100 MeV/nucleon will optimize Coulomb-breakup contribution. The number of virtual photons seen by the projectile is multipole dependent, so the extraction of radiative capture cross sections requires an understanding of the reaction mechanism. For the case of ^{7}Li breakup, Typel [Typ93] has shown that $E2$ breakup significantly effects the absolute yield and angular distribution of the breakup fragments ($E2$ transitions are expected to contribute $< 1\%$ of the radiative-capture cross section). "Postacceleration" effects, due to the differential acceleration of the breakup products in the Coulomb field, may complicate the reconstruction of the relative energy.

Experimental challenges include the separation the breakup yield from the much more intense elastic-scattering yield, and the reconstruction of the relative energy with sufficient precision and resolution.

In 1990 Utsunomiya *et al.* [Uts90] published results for the dissociation of 42-MeV ^{7}Li ions incident on ^{27}Al, ^{58}Ni, and ^{120}Sn targets, and 63-MeV ^{7}Li ions incident on ^{144}Sm and ^{208}Pb targets. Absolute cross sections for $^{3}\text{H}(\alpha,\gamma)$ were not reported, apparently because of interference from nuclear breakup. However, the reduced transition probabilities extracted for different bombarding energies and targets were consistent with a nearly universal energy dependence. The authors presented simple theoretical arguments that the energy dependence of the nuclear breakup should be similar to the Coulomb breakup. On this basis, values of S were reported for $80 \leq E \leq 980$ keV, assuming $S(500 \text{ keV}) = 0.060$ keV-b for the absolute normalization. The results, shown in Figure 1.6, indicate an increasing S-factor with decreasing energy, similar to that found by Schröder *et al.* Theoretical uncertainties and the large low-energy error bars preclude any definite conclusions about the $^3\text{H}(\alpha,\gamma)$ cross section from being drawn.

Experiments on the breakup of 54-MeV ^7Li ions incident on ^{12}C and ^{197}Au targets were published in 1992 by Gazes *et al.* [Gaz92]. Large nuclear-breakup contributions were found in the case of ^{12}C, and large distortions in the energy spectra (attributed to "postacceleration" effects) were observed in the case of ^{197}Au. No attempt was made to extract information on the $^3\text{H}(\alpha,\gamma)$ cross section.

1.2.2 Theory

All theoretical calculations of the $^3\text{H}(\alpha,\gamma)^7\text{Li}$ cross section share several common features. The interaction Hamiltonian for γ-ray emission is given by

$$H_{\text{int}} = -\frac{1}{c}\vec{\jmath}\cdot\vec{A}, \tag{1.14}$$

where $\vec{\jmath}$ is the nuclear charged-current density, and $\vec{A}$ is the vector potential of the γ-ray field. The γ-emission interaction is sufficiently weak compared to nuclear and Coulomb forces that the capture cross section can be calculated using Fermi's golden rule: $\sigma \propto |\langle\Psi_f|H_{\text{int}}|\Psi_i\rangle|^2$, where $|\Psi_i\rangle$ is the initial (elastic scattering) wavefunction, and $|\Psi_f\rangle$ is the final (bound state) wavefunction. The calculations proceed by decomposing H_{int} into multipoles ($E1$, $M1$, $E2$,...) and $|\Psi_i\rangle$ into partial waves. The $^3\text{H}(\alpha,\gamma)^7\text{Li}$ cross section primarily results from the $E1$ capture of s-waves, with a substantial contribution at higher energies also coming from the $E1$ capture of d-waves. Due to its small binding energy, the ^{7}Li wavefunction has a relatively large tail (of primarily $^3\mathrm{H}+\alpha$ structure) at distances beyond the range of the nuclear force. At low energies the capture matrix element primarily depends upon this part of the bound-state wavefunction. All calculations involve some form of approximation, as the calculation of $|\Psi_i\rangle$ and $|\Psi_f\rangle$ is in general a seven-body problem, which as yet has not been solved for realistic nucleon-nucleon forces. We note that $^3\mathrm{H}-\alpha$ elastic-scattering phase shifts, which determine $|\Psi_i\rangle$ beyond the range of the nuclear force, have been measured [Spi67, Iva68] for higher energies, $E \geq 1550$ keV.

The first calculations were reported in 1961 by Christy and Duck [Chr61] and by Tombrello and Phillips [Tom61], and included the $E1$ capture of s-waves. An improved calculation was published in 1963 by Tombrello and Parker; the $E1$ capture of s- and d-waves to final p-states was included, and several computational improvements were made. The internal structures of the triton and α particles were ignored, and only the extra-nuclear contribution to the capture matrix element was calculated. In this region, the radial dependence of the final bound states is given by Whittaker functions. The s and d scattering waves were calculated using the phase shifts from a hard-sphere potential with a 2.8-fm radius. This choice of radius gave a good description of the mirror $^3\mathrm{He}-\alpha$ scattering reaction, and was shown later [Spi67, Iva68] to give a reasonable description of higher-energy $^3\mathrm{H}-\alpha$ scattering. The two bound-state reduced widths, which determine the normalization of the Whittaker functions, were left as free parameters. The calculation was able to simultaneously describe the values of S and R measured by Griffiths *et al.* as well as the values of S and R found for the mirror $^3\mathrm{He}(\alpha,\gamma)^7\mathrm{Be}$ reaction by Parker and Kavanagh [Par63], using the same values for the reduced widths. Unfortunately, the calculation for $^3\mathrm{H}(\alpha,\gamma)$ was presented as a σ versus E plot, making it impossible to ascertain the predicted low-energy behavior. The resulting angular dependences of γ_0 and γ_1 were also calculated. Due to the assumption of s- and d-wave capture only, the predicted dependences were of the form $1 + a_2P_2(\cos\theta_{c.m.})$, where P_2 is the $\ell = 2$ Legendre polynomial.

Using the formalism of Tombrello and Parker for s- and d-wave $E1$ capture, we further investigated the origin of the a_2 coefficient, assuming that both d-wave phase shifts are equal. The result is

$$a_2 = -\frac{\frac{1}{2}y - \sqrt{2y}\cos\Delta\phi}{1+y}, \tag{1.15}$$

where $y = \sigma_d/\sigma_s$ and $\Delta\phi = \alpha_2 + \delta_2 - \alpha_0 - \delta_0$ is the phase difference (Coulomb + nuclear) between the s and d waves. The presence of $\sqrt{y}$, due to interference between s and d waves, means that there can be significant anisotropy even if the d-wave contribution is very small compared to the s wave. By taking y from Mohr *et al.* [Moh93] and using hard-sphere nuclear phase shifts (2.8-fm radius), we were able to reproduce the a_2 coefficients calculated by Tombrello and Parker within 5%. Odd terms in the angular distribution are possible, due to interference with $M1$ or $E2$ capture from odd partial waves. Terms with $\ell \geq 4$ are expected to be negligible, as higher multipolarities are predicted to be negligibly small in all calculations.

The mirror reaction, ^{3}He$(\alpha,\gamma)^7$Be, is also very important in another branch of astrophysics, as the number of ^{7}Be and ^{8}B neutrinos produced by our sun is dependent upon its cross section (at $E \approx 20$ keV). Due to the persistence of the solar neutrino problem, as well as interest in the rates of ^{3}H$(\alpha,\gamma)^7$Li and ^{3}He$(\alpha,\gamma)^7$Be in the big bang, several theoretical calculations of both reactions have been published in the last ten years.

The first resonating-group method (RGM) calculation of radiative α capture to $A = 7$ nuclei was made by Liu, Kanada, and Tang [Liu81], who calculated $S(E)$ for ^{3}He$(\alpha,\gamma)^7$Be. Subsequent RGM calculations of $S(E)$ for ^{3}H(α,γ) have been reported by Kajino and Arima [Kaj84], Kajino [Kaj86], Mertelmeier and Hofmann [Mer86], and Altmeyer *et al.* [Alt88]. An RGM calculation of $S(0) = 0.154$ keV-b has been reported by Chopovsky [Cho89]. This technique allows the nucleonic substructure of the ^{3}H and α clusters to be approximately taken into account, and guarantees adherence to the Pauli principle between nucleons. The scattering- and bound-state

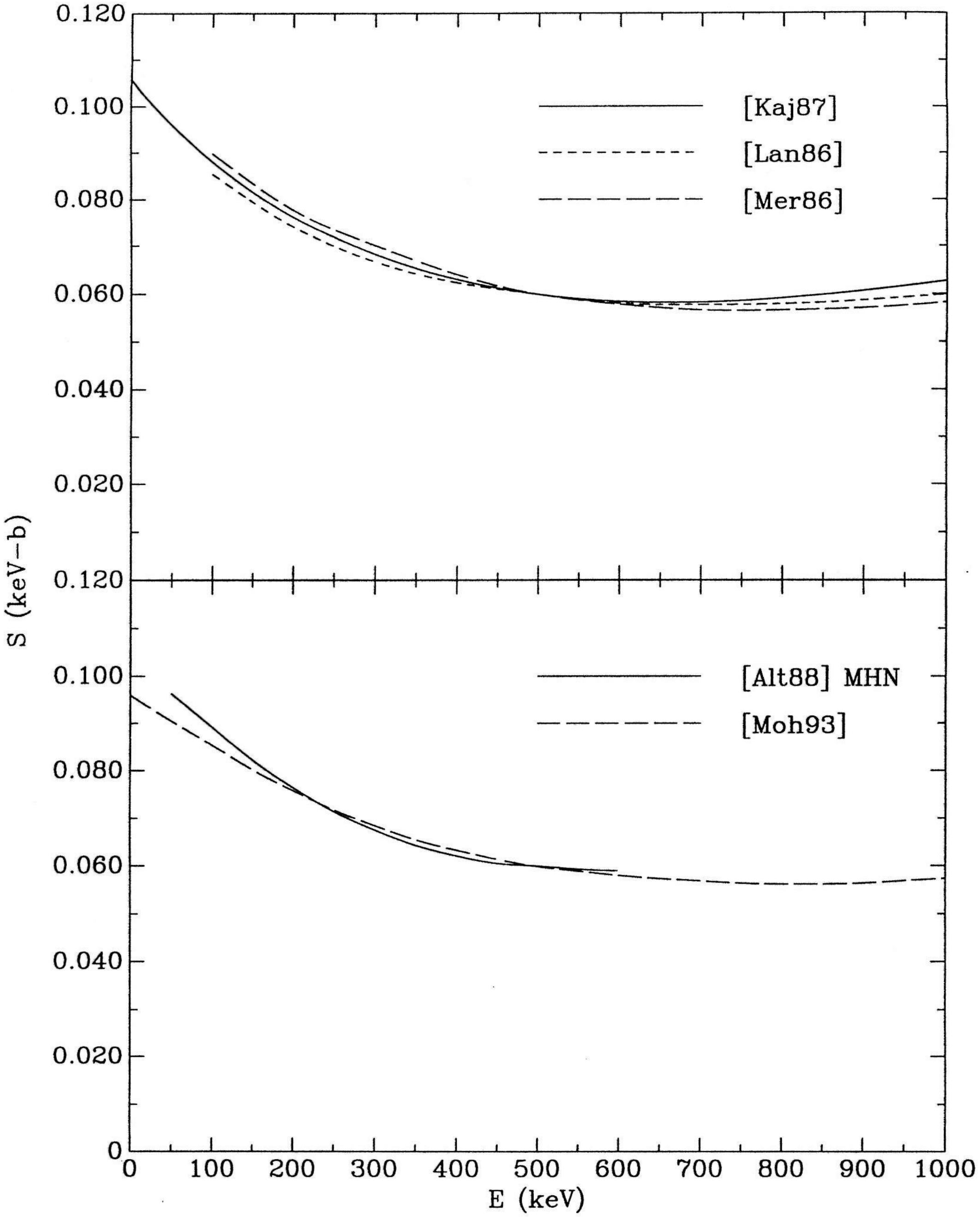

Figure 1.7: Theoretical calculations of $S(E)$ for ^{3}H(α,γ)^{7}Li by Kajino, Toki, and Austin [Kaj87], Langanke [Lan86], Mertelmeier and Hofmann [Mer86], Altmeyer *et al.* [Alt88], and Mohr *et al.* [Moh93]. We have used the Modified Hasegawa-Nagata (MHN) interaction calculation of Altmeyer *et al.* The curves have been normalized to $S(500\text{ keV}) = 0.060$ keV-b.

wavefunctions are calculated in a unified manner, and the full capture matrix element can be calculated. The predictive power of the method is however limited by the choice of the effective interaction. The calculated S-factor can vary by nearly a factor of two, depending on the choice of effective interaction [Kaj86, Alt88]. However, the calculated energy dependence of the S-factor is nearly the same for all calculations (see below). The choice of effective interaction can be constrained by requiring that the calculation reproduce the measured scattering phase shifts and ^{7}Li bound-state properties, perhaps reducing the uncertainty in the calculation. The various calculations differ in the model space and effective interaction(s) used.

Several other recent studies also warrant mention. Langanke [Lan86] has calculated $S(E)$ using a microscopic potential model. Kajino, Bertsch, and Kubo [Kaj88a] have estimated $S(0) = 0.097 \pm 0.038$ keV-b, using the measured electric-dipole polarizability of ^{7}Li. Kajino *et al.* [Kaj88b] have found a constraint on $S(0)$, $0.083 < S(0) < 0.15$ keV-b, using the experimental matter radius of ^{7}Li and the correlation found in RGM calculations between $S(0)$ and the matter radius. Kajino, Toki, and Austin [Kaj87] give an expression valid for $E \leq 1500$ keV,

$$S(E) = S(0)\exp(-2.056E)(1 + 2.2875E^2 - 1.1798E^3 + 2.5279E^4), \qquad (1.16)$$

with E in MeV, that reproduces within 3% the energy dependence found in RGM calculations [Kaj84, Kaj86]. Buck and Merchant [Buc88] calculated $S(0) = 0.09 \pm 0.03$ keV-b using a potential model. Another calculation of $S(E)$ using a potential model has been reported by Mohr *et al.* [Moh93].

All of the calculations predict an increasing $S(E)$ at low energies. Several of the calculations are shown in Figure 1.7. The curves have been normalized to $S(500 \text{ keV}) = 0.060$ keV-b. It is seen that the energy dependences of the calculations are consistent within $\approx 10\%$, due to the validity of the extra-nuclear approximation used in the early calculations. The uncertainty in absolute magnitude primarily arises from the normalization of the asymptotic ^{7}Li wavefunction. None of the calculations predicts as large an increase in the low-energy S-factor as found by Schröder *et al.* or Utsunomiya *et al.* It should be noted that calculations of the shape of $S(E)$ for the ^{3}He$(\alpha,\gamma)^7$Be reaction are in good agreement with experiment (see for example Kajino, Toki and Austin [Kaj87]).

Through 1985, the recommended thermonuclear reaction rate [Cau85] for ^{3}H$(\alpha,\gamma)^7$Li was calculated assuming a constant S equal to 0.064 keV-b as found by Griffiths *et al.* The most recent compilation [Cau88] uses $S(E)$ found by Langanke [Lan86], which agrees with the data of Griffiths *et al.*, and increases at low energies to $S(0) \approx 0.105$ keV-b. Several astrophysical calculations [Kaw88, Kra90, Smi93] have used different reaction rates based on the more recent experiments.

Low-Energy Logarithmic Derivative

Using assumptions similar to those of Tombrello and Parker [Tom63], Williams and Koonin [Wil81] calculated an expansion for the low-energy logarithmic derivative,

$$\frac{1}{S}\frac{dS}{dE} = a + bE. \tag{1.17}$$

Using a hard-sphere radius of 2.8 fm, the authors found $a = -2.034$ MeV^{-1} and $b = -3.709$ MeV^{-2}. Schröder *et al.* fit their low-energy data with this energy dependence, finding $S(0) = 0.162 \pm 0.024$ keV-b. However, Kajino [Kaj88c] has argued that the Williams-Koonin calculation contains a computational error; he finds $a = -1.15$ MeV^{-1} with what appears to be an identical calculation. The negative sign of b is inconsistent with the positive curvature found in all other calculations. Values of a from other calculations (-2.056 MeV^{-1} Equation 1.16 [Kaj87], -2.0 MeV^{-1} [Buc88], -1.02 MeV^{-1} [Moh93]) vary by a factor of two, even though the overall agreement of the energy dependences is within $\approx 10\%$ (Figure 1.7).

Branching Ratio

Calculations of the branching ratio show much less model dependence than does the absolute cross section. RGM calculations [Kaj86, Alt88] find nearly energy-independent branching ratios in the range 0.41 – 0.44. Kajino, Mathews, and Ikeda [Kaj89] estimated $R(0) = 0.47 \pm 0.07$ using a kinematical direct capture model and the measured $^3\mathrm{He}(\alpha,\gamma)^7\mathrm{Be}$ branching ratio. Mohr *et al.* [Moh93] also found R to be nearly independent of energy, with a value of 0.43. All of these calculations are significantly larger than the experimental value 0.32 ± 0.01 found by Schröder *et al.*, but are in reasonable agreement with the data of Griffiths *et al.* and Burzynski *et al.*

1.3 Experimental Overview

The goal of the present experiment was to measure the absolute $^3\mathrm{H}(\alpha,\gamma)^7\mathrm{Li}$ cross section, with particular emphasis on the energies relevant to the big bang. The measurements were extended to as low an energy as practical, and covered energies ranging over a factor of 20. Our experimental approach, using Ti–^{3}H targets, an α beam, and a Ge γ-ray detector, is similar to that used by Schröder *et al.* and Burzynski *et al.*

Our experiment does offer several technical improvements compared to the earlier work. The γ rays were detected using a high-purity-Ge detector with 85% relative efficiency, giving a substantial increase in detection efficiency. The determination of the total cross section from the measured γ-ray yield (which necessarily covers only a limited angular range) requires knowledge of the angular distribution. Angular distributions were measured at nine energies for this reason as well as for comparison with theoretical calculations. The systematic uncertainty in the absolute normalization was reduced by using the well known $^3\mathrm{H}(d,\alpha)$ reaction to determine the ^{3}H areal density. Several targets were bombarded to test the reproducibility of the absolute normalization. The data analysis is improved in many respects, particularly in the treatment of coincident γ-ray detection effects.

Preliminary measurements were made in 1990 using a 35% Ge detector and a commercial Ti–^{3}H target which had been extensively bombarded with ^{7}Li in an unrelated experiment. Due to problems from the implanted ^{7}Li and also target deterioration the results were not of high quality. Considerable difficulty was then experienced in obtaining suitable Ti–^{3}H targets, which led us to develop our own production technique as described in Chapter 2. The results reported here were taken in 1992 and 1993 using the 85% Ge detector and four targets made with our apparatus.

Chapter 2

Tritium Target Preparation

The preparation of metal hydrides for use as hydrogen-isotope targets for ion-accelerator experiments has a long history [Gra49, Con52, Roc52, Con52, Mas57, Sco59, Coo60, Smi67, Kob89]. The metals Ti, Zr, and Er have been used; Ti has been the most common in recent times. The targets are most often used for neutron production through the ^{3}H(d,n), ^{3}H(p,n), or ^{2}H(d,n) reactions. Typically, a (0.2–2)-mg/cm^2 metal layer is evaporated onto a solid substrate, which is then heated in the presence of the desired hydrogen-isotope gas. When the metal temperature reaches $\sim$ 400 °C, hydride formation occurs rapidly. Stoichiometries approaching H:Ti = 2.0:1 have been reported in bulk samples of Ti [Smi48].

As discussed in the Introduction, we chose to measure the ^{3}H$(\alpha,\gamma)^7$Li reaction using Ti–^{3}H targets, an α beam, and a high-purity-Ge detector to measure the emitted γ rays. Due to the small cross sections involved ($\approx$ 50 nb at $E_\alpha = 150$ keV), the ^{3}H areal density of the target should be high to maximize the γ-ray yield. On the other hand, the energy lost by the α beam in the target is proportional to the areal density. Due to energy loss, ^{3}H$(\alpha,\gamma)^7$Li reactions will occur at varying E_α, depending upon the depth of the interaction in the target. The reaction kinematics ($E_\gamma \approx \frac{3}{7}E_\alpha + Q$) imply that the α energy loss contributes to the width of the energy spectrum of the emitted capture γ rays. The ^{3}H areal density is thus limited by the choice of an acceptable γ-ray line width in the detection system. Furthermore, the cross section far below the coulomb barrier varies rapidly with energy, necessitating an accurate determination of the effective reaction energy, which is subject to less systematic error for small energy losses. In principle the best choice would be a windowless ^{3}H-gas target, but this option was deemed impractical in our laboratory due to radiation-safety considerations.

We determined that a Ti–^{3}H target of $\sim 20\,\mu\text{g/cm}^2$ would provide the best compromise of energy loss and γ-ray yield. Ti is preferable to the other materials because it has the smallest stopping power per ^{3}H atom (assuming comparable stoichiometry for all materials could be obtained). The ^{3}H contributes only 25% to the energy loss for Ti^{3}H$_2$ targets.

Attempts to obtain targets with the above characteristics from commercial sources were unsuccessful. The majority of companies or laboratories that historically produced ^{3}H targets had either temporarily or permanently stopped this service. The targets that we were able to purchase had poor stoichiometries ($^3\text{H:Ti} < 0.5$) and/or unsuitable Ti thicknesses. The 20-μg/cm^2 target desired was much thinner than the targets commonly used for other purposes. A survey of the previous literature indicated that a common problem affecting target preparation is poisoning of the Ti layer with contaminant gases before hydriding. It is reasonable to suppose that a very thin target would be more susceptible to these problems, particularly if the contamination is primarily near the surface. The technique most often described in the cited references is the evaporation of a Ti layer onto the substrate in one vacuum system followed by transfer of the target *in air* to another for hydriding. We believe that some of the difficulties commercial suppliers experienced in preparing a target to our specifications may be due to contamination of the Ti during the transfer step.

The systems and procedures that we developed to fulfill our needs are described in the following sections. In our process the Ti evaporation and hydride formation take place in the same apparatus, *without breaking vacuum.* The system has been extensively tested, first making Ti–^{2}H targets, and finally Ti–^{3}H targets. Methods for accurately determining the ^{2}H, ^{3}H, and Ti areal densities are also discussed. An accurate measurement of the ^{3}H areal density is crucial for obtaining absolute ^{3}H(α,γ) cross sections.

2.1 Description of Apparatus

The production of a Ti–H target consists of two operations: the evaporation of Ti onto a substrate, and the heating of the Ti and substrate in an atmosphere of hydrogen isotope to induce the formation of hydride. The boat used for Ti evaporation and the target substrate are each heated using a 3-turn induction coil centered either at the boat or target position. Radio-frequency power at 50–200 kHz is supplied to the coil by a 2.5-kW commercial supply (Lepel LSS-2.5). A drawing of the apparatus is shown in Figure 2.1.

The closed-ended quartz tube (42.1-mm o.d., 38.1-mm i.d.) hanging below the gas-handling manifold is sealed with a Viton O-ring. All other seals are metal gaskets or ferules. The high vacuum in the system is supplied by a 20-L/s ion pump. A 1.3-cm long cylindrical quartz tube (36.3-mm o.d., 30.0-mm i.d.) supports the boat from the bottom of the closed tube. The target substrate is supported above the boat a distance of 5.1 cm by a length of identical cylindrical tube. Several holes were ground through the walls of the inner quartz tubes in order to increase the pumping speed. With all valves closed, the interior volume is $\sim$ 300 mL.

Additional features of the system are shown schematically in Figure 2.2. Pressures between 10^{-3} and 10^{3} Torr are read by a Granville-Phillips Series 275 "Convectron" gauge, using supplied calibration curves for various gases. Non-radioactive gases are pumped away using a standard mechanical pump. The charcoal-filled trap, when chilled to LN_2 temperature, is used to pump away excess ^{3}H gas for eventual disposal. A 150-mL cylinder of high-purity He gas is attached for use as a coolant (described in more detail below). The locations of the vent and the hydrogen-isotope gas supply are also shown.

The boats used for Ti evaporation merit special comment. A top view of the 0.38-

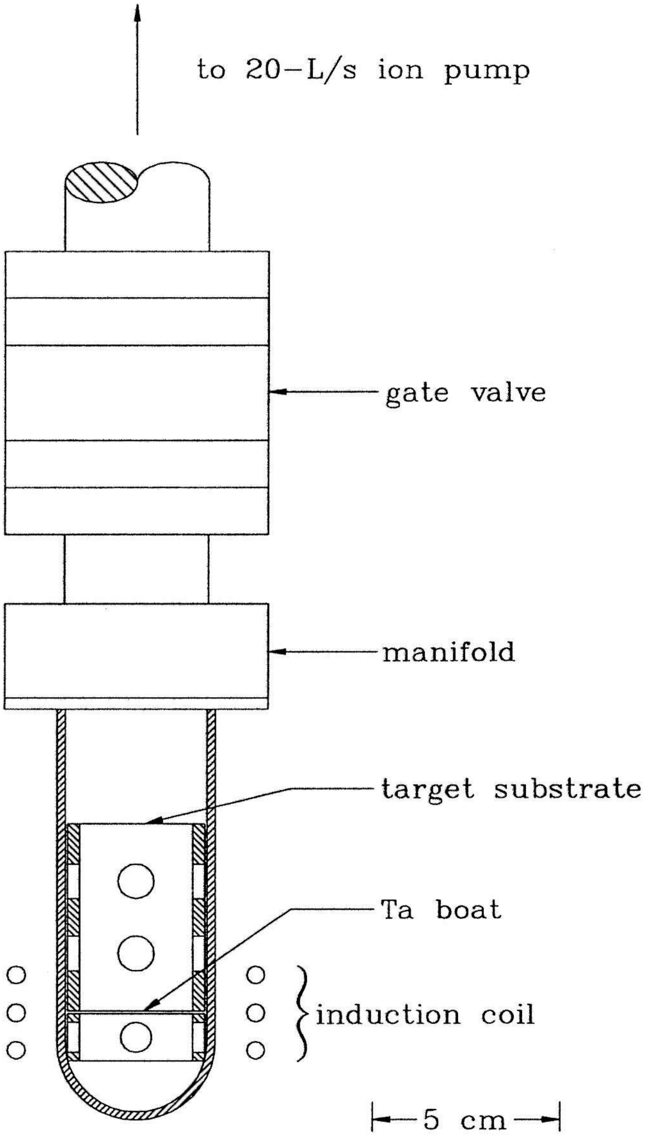

Figure 2.1: Side view of the target-production apparatus. The four ports connected to the gas-handling manifold are not shown (see Figure 2.2).

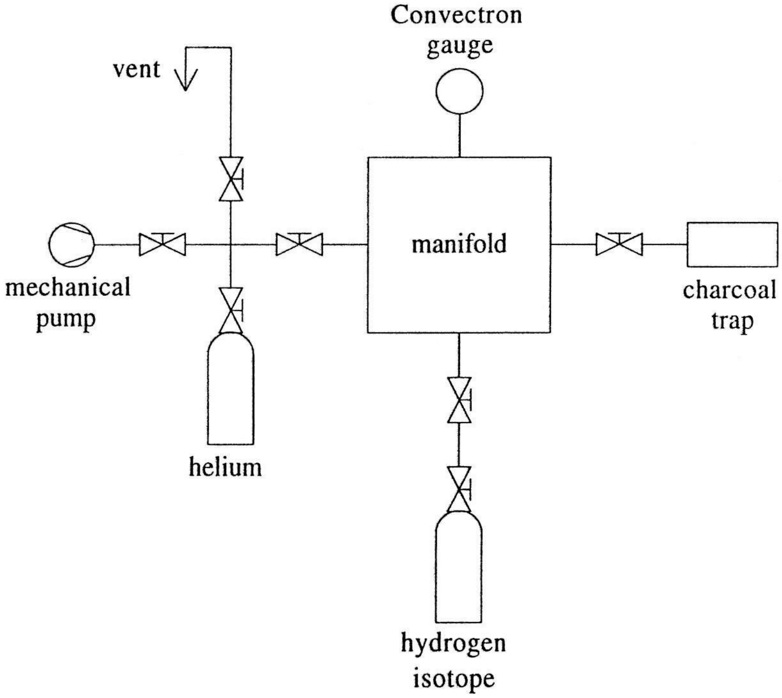

Figure 2.2: Schematic diagram (top view) of the apparatus. The ion pump and quartz tube are not shown (see Figure 2.1).

mm-thick Ta boats used is shown in Figure 2.3. The hemispherical dimple for the Ti source is positioned so that it is in the center of the quartz tube. The shape of the boat is designed to maximize the boat temperature at the source position for a given power output from the induction-heating power supply. New boats were thoroughly outgassed for several minutes in vacuum at temperatures in excess of those attained during Ti evaporation.

2.2 Target Production Procedure

The Ti was evaporated onto substrates of 31.7-mm-diameter Cu (0.81-mm thickness) or Ta (0.76-mm thickness). All of the targets used for the ^{3}H(α,γ) reaction were made using Cu substrates. The Cu substrates were cleaned with detergent, etched for 30 s in 3M HNO_3, and finally rinsed with distilled H_2O. Ta substrates were treated in the

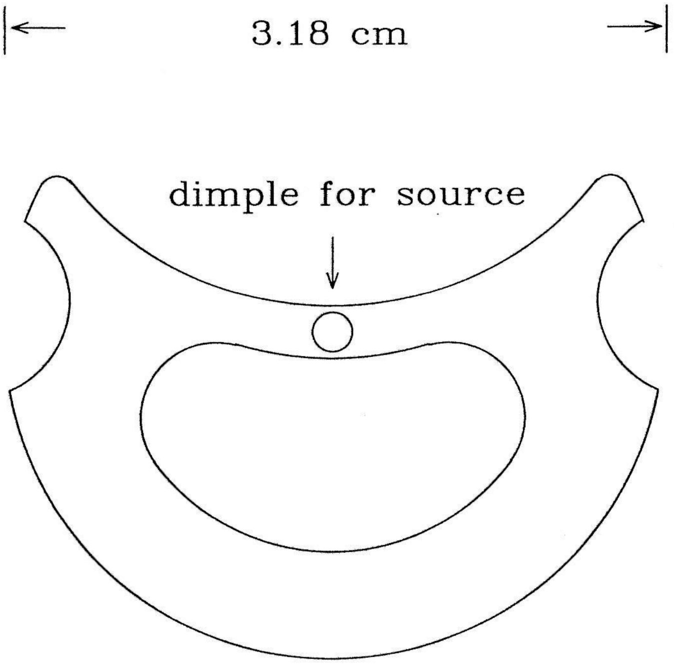

Figure 2.3: Top view of the Ta boats. The Ti evaporation source is placed in the hemispherical dimple at the center.

same manner, except the HNO_3 etch was replaced by a 15-s etch in 5M HNO_3 : 48% HF = 3:1 (by volume), followed by a 15-s etch in 8M HNO_3.

The Ti evaporation sources (typically $\sim$ 3 mg Ti) were cut from wire stock that had been previously outgassed in high vacuum by passing current through it, heating it to just below the melting point. The Ti source and substrate were then installed in the quartz tube assembly, and the system was pumped to high vacuum (base pressure $\approx 4 \times 10^{-8}$ Torr, as determined by ion-pump current). At this point the substrate was outgassed by heating it for five minutes (orange heat for Cu, yellow for Ta) with the induction coil. Next, the Ta boat and Ti source were outgassed by heating the boat for 20 minutes at a temperature somewhat below that required to melt Ti. The system was then allowed to pump and cool for several hours in order to achieve the best vacuum possible.

The Ti source was evaporated by slowly raising the power applied to the boat, until the source was observed to melt. The power was then left constant for two minutes in order to evaporate the Ti. This method proved effective in evaporating $\approx$ 70%

of the Ti (the remaining fraction appeared to amalgamate with the Ta). During evaporation, the pressure at the ion pump remained below 5×10^{-7} Torr. After roughly 10 such evaporations, the boats typically developed holes in the bottom and required replacement.

Following evaporation, the gate valve was closed and ≈ 1.0 Torr of high-purity He gas was admitted to the quartz tube. The presence of the gas increased the thermal conductivity inside the tube, greatly reducing the time required for the objects inside the tube to return to room temperature. After 20 minutes the He was pumped away, and the system was returned to high vacuum (gate valve open).

Next, the gate valve was closed, and 1.5 Torr of ^{2}H or ^{3}H gas was admitted (corresponding to ~ 1.5 Ci for ^{3}H). The substrate was then heated for three minutes. The temperature reached by the substrate is not known, but was reproducible in terms of the induction-heater control settings. It was found that if the Cu substrate was heated to a visible red temperature the Ti and Cu would amalgamate, which invariably led to a poor H:Ti ratio. We used a power level that, in vacuum, would heat a Cu substrate from room temperature to red heat in three minutes. The progress of hydride formation was monitored by recording the gas pressure versus time.

Upon admission of the hydrogen-isotope gas, some spontaneous absorption of the gas by the Ti occurred (i.e., without heating the substrate). The amount of spontaneous absorption that takes place is apparently very sensitive to the vacuum conditions during Ti evaporation. Absorption at room temperature was not anticipated, as the previous references [Gra49, Lil51, Roc52, Con52, Mas57, Coo60] stated that heating to ~ 400 °C was necessary for hydride formation. This effect is somewhat undesirable since it allows absorbtion by Ti which was evaporated onto surfaces other than the substrate, and because its extent is not reproducible. Attempts to control the effect by precooling the substrate and inner quartz pieces prior to the admission of hydrogen-isotope gas (by filling the quartz tube with 1.0-Torr He, immersing the tube in LN_2 for ~ 30 minutes, and then pumping out the He) were unsuccessful. On one occasion we tested the ^{2}H areal density of a target which was not heated. A ^{2}H:Ti ratio varying between 0.6 and 1.6 over the surface of the target was found. All of the other targets were heated in the hydrogen-isotope gas, improving the uniformity and reproducibility of the process.

Following the heating of the target, the system was allowed to cool until a constant pressure was reached ($\sim$ 15 minutes). The remaining gas was pumped away, using the LN_2-cooled charcoal trap in the case of ^{3}H gas, or the mechanical pump for ^{2}H gas. Then the residual pressure was pumped using the ion pump. The gate valve was then closed and the system was vented with air, at which point the target was transferred to the accelerator facility for testing.

Following each use of ^{3}H gas, the system was reassembled with another substrate, but without a new Ti source, and pumped to high vacuum. The boat was then heated for five minutes at yellow heat with the gate valve closed and the valve to the LN_2-cooled charcoal trap open in order to outgas as much of the residual ^{3}H radioactivity as possible and collect it in the trap.

The final step was to prepare the system for its next use by removing the Ti deposits from the quartz pieces with acid and distilled-H_2O rinses.

Five targets (numbered 1-5) were produced on Cu substrates. Targets 1 and 3–5 were used for the ^{3}H(α,γ) measurements (insufficient Ti was evaporated on target 2). An additional target on Ta backing was produced for some unrelated experiments.

All procedures involving ^{3}H gas are done in a fume hood in our isotope laboratory, with disposal of radioactive waste according to regulations in our license. The air in the personnel operating area is continuously tested with a tritium monitor during ^{3}H-handling procedures.

2.3 Target Characterization

The use of accelerator techniques to determine the hydrogen-isotope content of metals has been extensively reviewed [Kha89]. The ^{2}H, ^{3}H, and Ti areal densities were determined using the ^{2}H(^{3}He$,\alpha$), ^{3}H(d,α), and Ti(α,α) reactions, respectively. The

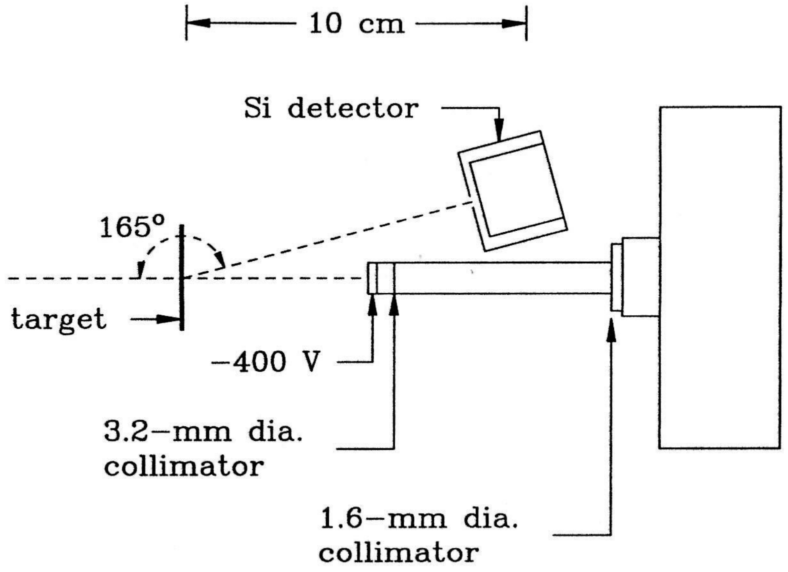

Figure 2.4: Scale drawing of the pertinent parts of the 0°-beamline scattering chamber.

proton, deuteron, D_3^+, $^3He^+$, and $^4He^+$ beams were supplied by the Caltech 3-MV Pelletron Tandem Accelerator. The beam is described in more detail in Section 3.2.

The experiments were performed using the scattering chamber on the Pelletron accelerator's 0° beamline. A scale drawing of the pertinent components is presented in Figure 2.4. The charged particles were detected at $\theta_{\mathrm{lab}} = 165°$ with a silicon surface-barrier detector collimated to have a solid angle of 1.194 ± 0.018 msr. The beam, collimated to a 1.6-mm diameter, was incident normal to the target. The target was biased at +300 V in order to ensure accurate beam-current integration by preventing secondary electron emission, and the collimator was followed by a −400 V suppression ring. A pulser peak was inserted above the spectrum to monitor dead-time corrections (typically less than 5%).

The beam-current integration and detector solid angle were checked by measuring the Cu(p,p) yield from a thick Cu substrate for $2000 \leq E_p \leq 2600$ keV, where the cross section is known to follow the Rutherford formula [Gol67], and where the proton-stopping power [Zie77] is known to 1%. The expected height of the plateau at its edge can be calculated from the differential cross section and stopping power as described by Sargood [Sar82]. The measured values were in excellent agreement with calculated values over the entire range; for example, the measured and calculated values at $E_p = 2200$ keV were $(9.22 \pm 0.17) \times 10^4$ and $(9.03 \pm 0.09) \times 10^4$ protons-keV$^{-1}\mu$C^{-1}sr^{-1}, respectively.

2.3.1 Ti Areal Density

The Ti areal density was determined by elastic α scattering for $1500 \leq E_\alpha \leq 2250$ keV, where the cross section is given by the Rutherford formula. A spectrum obtained at $E_\alpha = 2000$ keV from a Ti–^{3}H layer on a Cu substrate (target 1) is shown in Figure 2.5; also shown for comparison is the spectrum from a blank Cu substrate. An areal density of 2.96×10^{17} Ti atoms/cm^2 at the center of the target was found using the number of counts in the Ti(α, α) peak (the mean energy of the α particles was used in evaluating the Rutherford formula). Figure 2.5 shows a shift in the edge of the Cu(α, α) scattering plateau as a result of the Ti–^{3}H layer. Using 5.52×10^{17} ^{3}H atoms/cm^2 (determined as described below), the above Ti areal density, and assuming stopping-power additivity [Zie77], a shift of 46.2 keV was calculated, in good agreement with the observed 47.5 keV.

The uniformity of the Ti layers was excellent; the areal density was found to decrease slowly with distance from the center of the target (6% lower at 12 mm from center), consistent with the substrate – Ti source evaporation geometry. The Ti(α, α) spectra were also useful for profiling the Ti and Cu composition. In some early tests the Ti and Cu were amalgamated, an effect clearly visible in the spectra.

2.3.2 ^{2}H Areal Density

For Ti–^{2}H targets, the ^{2}H areal density was determined by detecting α particles from the ^{2}H(^{3}He$, \alpha$) reaction with $E[^3\text{He}] = 650$ keV. This energy corresponds to the peak of a broad maximum ($\Gamma_{\text{lab}} \approx 600$ keV), where the cross section is known to $\sim 3\%$ [Mol80, Dav80]. We have assumed $\frac{d\sigma}{d\Omega}(\theta_{\text{lab}} = 165^\circ) = 34.3$ mb/sr in the following

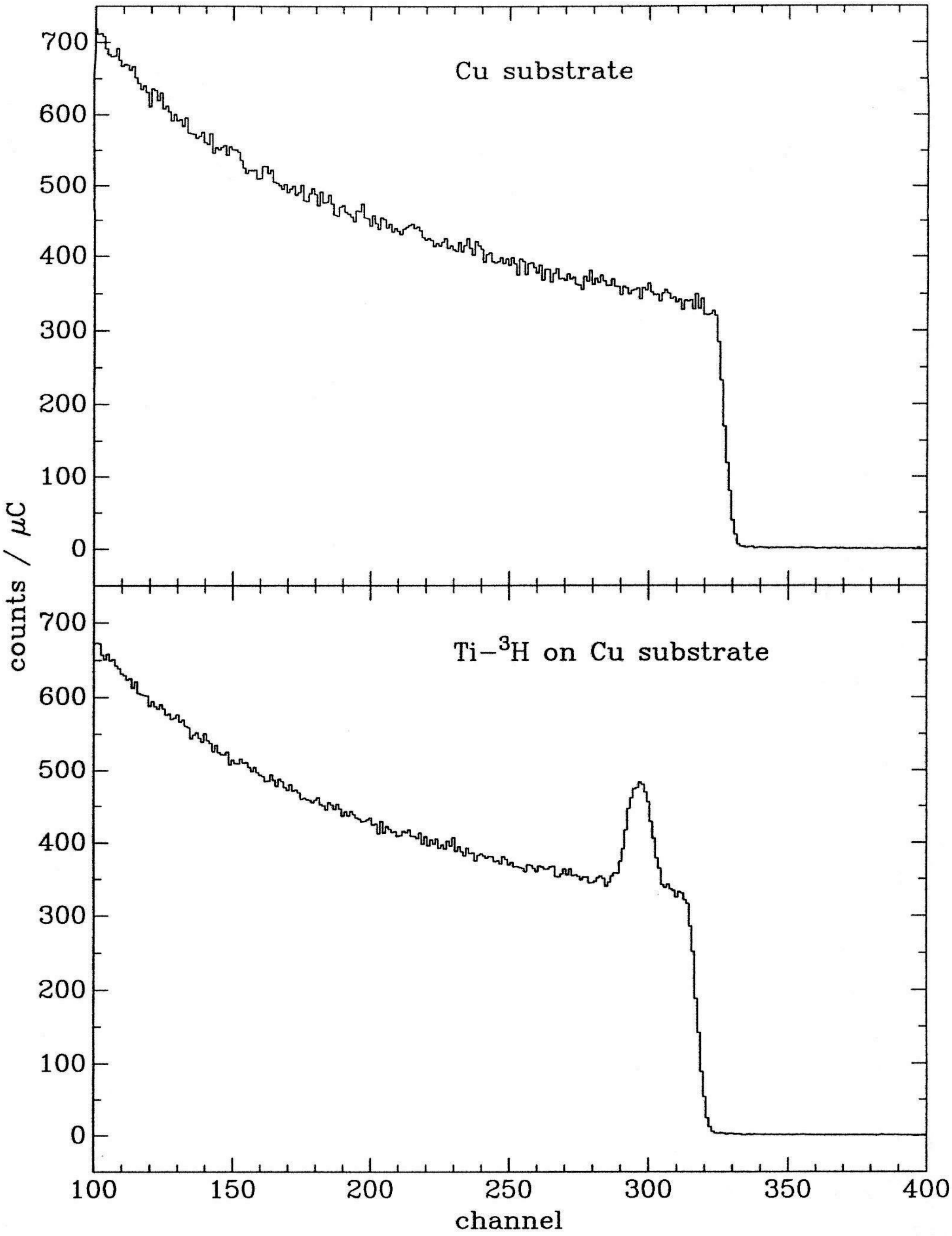

Figure 2.5: Spectra of scattered 2000-keV α particles observed at $\theta_{\text{lab}} = 165°$, from a blank Cu substrate (top panel) and target 1, a Ti–^{3}H layer on Cu substrate (bottom panel). The peak in the bottom panel at channel $\approx$ 295 is from the Ti layer. The leading edge of the Cu-scattering plateau in the lower panel is shifted by 10.0 channels due to the presence of the Ti–^{3}H layer.

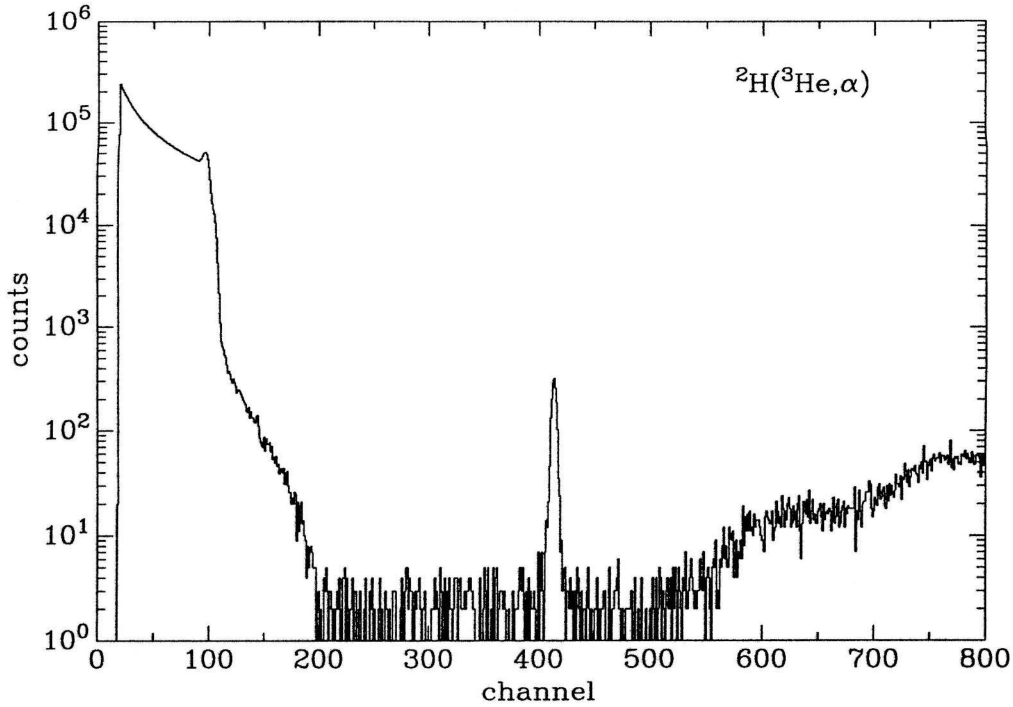

Figure 2.6: Si-detector spectrum resulting from the 650-keV-^{3}He bombardment of Ti–^{2}H on Cu substrate. The peak at channel ≈ 415 is due to α particles from the ^{2}H(^{3}He, α) reaction. The counts in channels $\geq$ 550 are due to high-energy protons from ^{2}H(^{3}He, p) that deposited a fraction of their energy in the detector.

analysis. The ^{2}H(^{3}He, α) spectrum obtained from Ti–^{2}H on a Cu substrate is shown in Figure 2.6; the ^{2}H and Ti areal densities were determined to be 5.05×10^{17} and 3.24×10^{17} atoms/cm^2, respectively, yielding a ^{2}H:Ti ratio of 1.56:1.

2.3.3 ^{3}H Areal Density

The ^{3}H areal densities of the Ti–^{3}H targets were determined using the ^{3}H(d, α) reaction. The total cross section and center-of-mass Legendre coefficients for this reaction were taken from the evaluation of Drosg and Schwerer [Dro87]; the uncertainty is estimated to be 1.5% for $E_d < 400$ keV, increasing to 4% for higher energies.

The majority of the Ti–^{3}H targets were tested over the range $250 \leq E_d \leq 700$ keV, with a deuteron beam produced using the accelerator's tandem mode (thus avoiding ^{2}H gas in the terminal ion source, which could lead to ^{2}H$_2^+$ contamination of the α^+

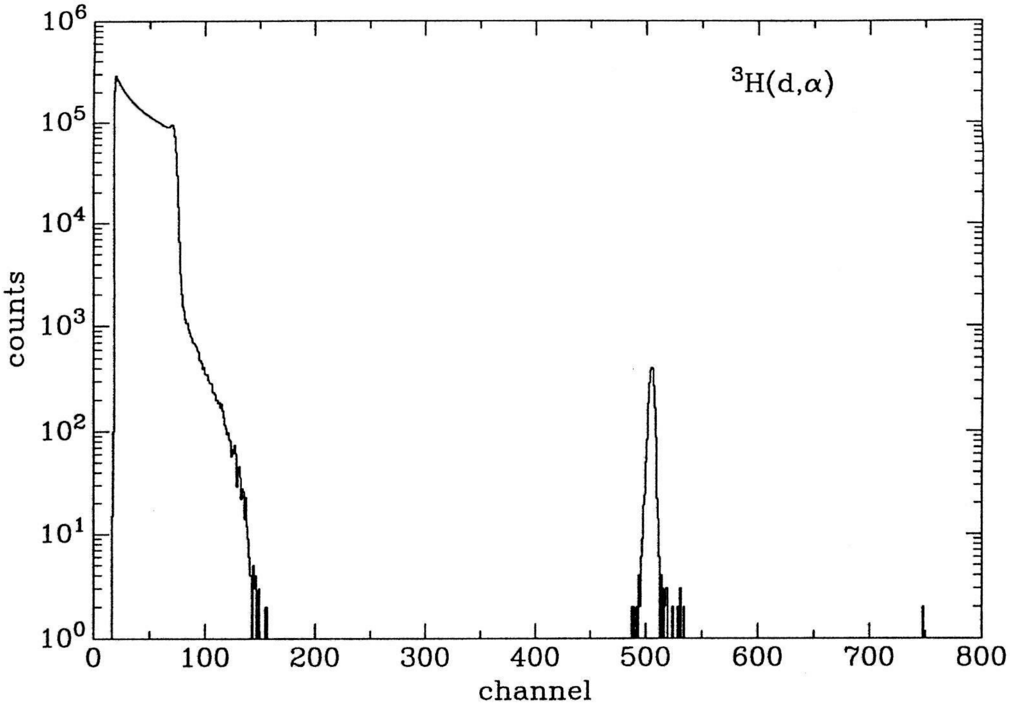

Figure 2.7: Si-detector spectrum resulting from bombarding Ti–^{3}H on Cu substrate (target 1) with a 400-keV deuteron beam. The peak at channel ≈ 505 is due to α particles from $^3\mathrm{H}(d,\alpha)$.

beam; see Appendix B). A sample spectrum obtained at $E_d = 400$ keV for target 1 is shown in Figure 2.7. The observed spectra were consistent with the ^{3}H being uniformly distributed in the Ti, with no ^{3}H in the target backing. In all cases the energy dependence of the α yield (including small corrections for energy loss) was consistent with the evaluated cross sections [Dro87]. From the average of runs at 7 energies between 250 and 700 keV, the ^{3}H areal density of target 1 was determined to be 5.52×10^{17} atoms/cm^2, yielding a ^{3}H:Ti ratio of 1.87:1. The $^3\mathrm{H}(d,\alpha)$ excitation functions from targets 1, 3–5 are shown in Figure 2.8, along with the fits to the energy dependence of Drosg and Schwerer [Dro87]. The ^{3}H:Ti ratio was found to be constant within 3% over the surface of the targets.

In order to test the evaluated cross section [Dro87], the $^3\mathrm{H}(d,\alpha)$ measurements were extended down to $E_d = 70$ keV to include the peak at $E_d \approx 110$ keV (where the cross section is best known). The required deuteron energies were obtained by using

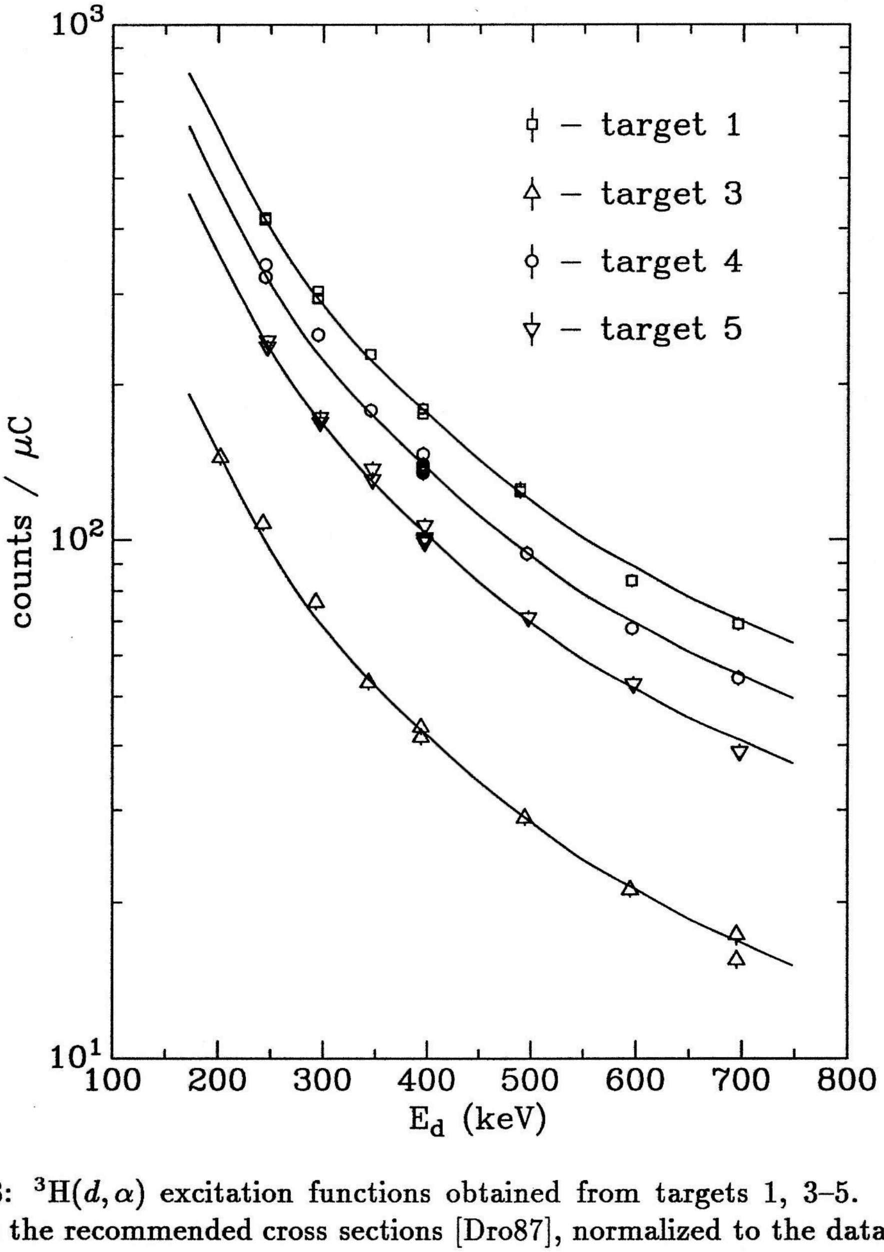

Figure 2.8: ^{3}H(d,α) excitation functions obtained from targets 1, 3–5. The solid curves are the recommended cross sections [Dro87], normalized to the data.

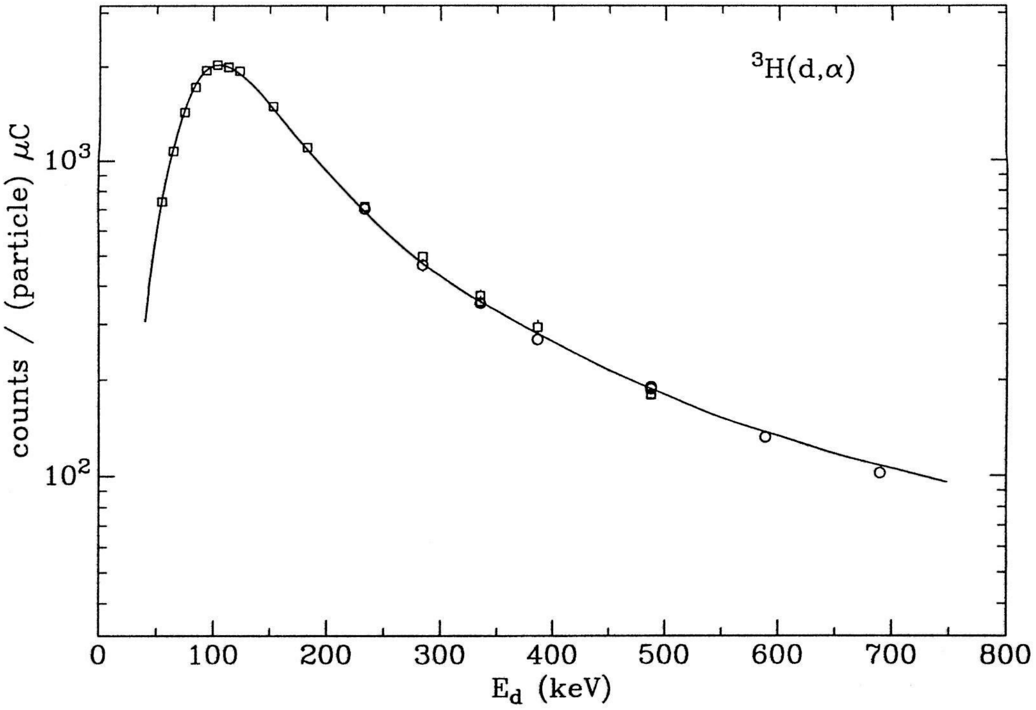

Figure 2.9: ^{3}H(d,α) excitation function obtained using deuteron (circles) and D_3^+ (squares) beams. The solid curve is the recommended cross section [Dro87], normalized to the data.

the molecular ion D_3^+ from the accelerator's terminal ion source. These measurements were performed after the ^{3}H(α,γ) experiments, since the D_2 gas was not installed in the ion source during the (α,γ) work due to concern about deuteron contamination of the α beam.

In this case, a target prepared on a Ta substrate was used. A 560-μg/cm^2 Ni foil was placed in front of the detector to reduce the count rate due to elastic scattering. The resulting excitation function (corrected for energy loss) is shown in Figure 2.9; the data agree with the shape given by [Dro87] (solid line) within 4%.

2.4 Results and Discussion

The technique described is capable of consistently making targets with hydrogen isotope to Ti ratios of $\geq 1.5{:}1$. The results for the four Cu-backed ^{3}H targets used for the ^{3}H(α,γ) measurements are shown in Table 2.1. During the (α,γ) measurements,

Target	Ti (10^{17}/cm^2)	^{3}H (10^{17}/cm^2)	N	χ^2
1	2.96	5.52(4)	13	13.1
3	4.67	1.32(2)	10	17.4
4	2.86	4.33(4)	14	17.5
5	1.90	3.23(3)	13	13.2

Table 2.1: The ^{3}H and Ti areal densities determined for the Cu-backed targets used for (α, γ) measurements. Also given are the number of data points N and the χ^2 (using only statistical errors) for the fits to the ^{3}H(d, α) cross section. The numbers given in parentheses with the ^{3}H areal densities are the statistical errors in the least significant digit, scaled by $\sqrt{\frac{\chi^2}{N-1}}$.

the targets were directly water cooled, and the α beam (5–30 μA) was rastered over ~ 1 cm^2. The targets proved very stable under bombardment; the observed deteriorations are given Chapter 3 (Table 3.1) and the corrections applied are described in Chapter 4. The deterioration is attributed to sputtering; blister formation at the Ti – Cu interface was not observed (a problem encountered with commercial targets).

One improvement in the apparatus would be the addition of an infrared temperature sensor to monitor the heating of the substrate. The technique currently used to reproducibly heat the substrate requires that the applied heat and gas-pressure history be reproduced, since the temperature reached by the substrate depends on pressure-dependent convection as well as the delivered radio-frequency power. Another improvement would be the addition of a mechanism to transfer the substrate to a separate chamber after Ti evaporation (still without breaking vacuum). This procedure would conserve the ^{3}H gas by preventing it from being absorbed by the Ti that was evaporated onto surfaces other than the substrate.

The nuclear-reaction-analysis techniques used were capable of determining absolute ^{2}H, ^{3}H, and Ti areal densities to $\sim 4\%$.

Chapter 3

Experimental Apparatus and Procedures

The preparation of the Ti–^{3}H targets proved to be the most difficult and time-consuming part of the experiment. The remaining aspects of the experiment, bombarding the targets with α^+ beam and detecting γ rays, were comparatively straightforward. However, a careful consideration of all experimental aspects is important for achieving the most accurate results.

The following sections describe the target chambers, beam, γ detection, and general procedures followed. Particular attention is paid to calibration of the high-purity Ge γ-ray detector. The availability of large-volume detectors has led to higher efficiencies than were previously possible, but has also increased the importance of coincident-summing corrections. A detailed description is given of the photofraction measurements, which are crucial for making coincident-summing corrections.

3.1 Target Chambers

Several factors were considered in the design of the target chambers. A knife-edge vacuum seal to the target was used in order to achieve the best possible (and hydrocarbon-free) vacuum. The backs of the Cu targets were cooled with flowing

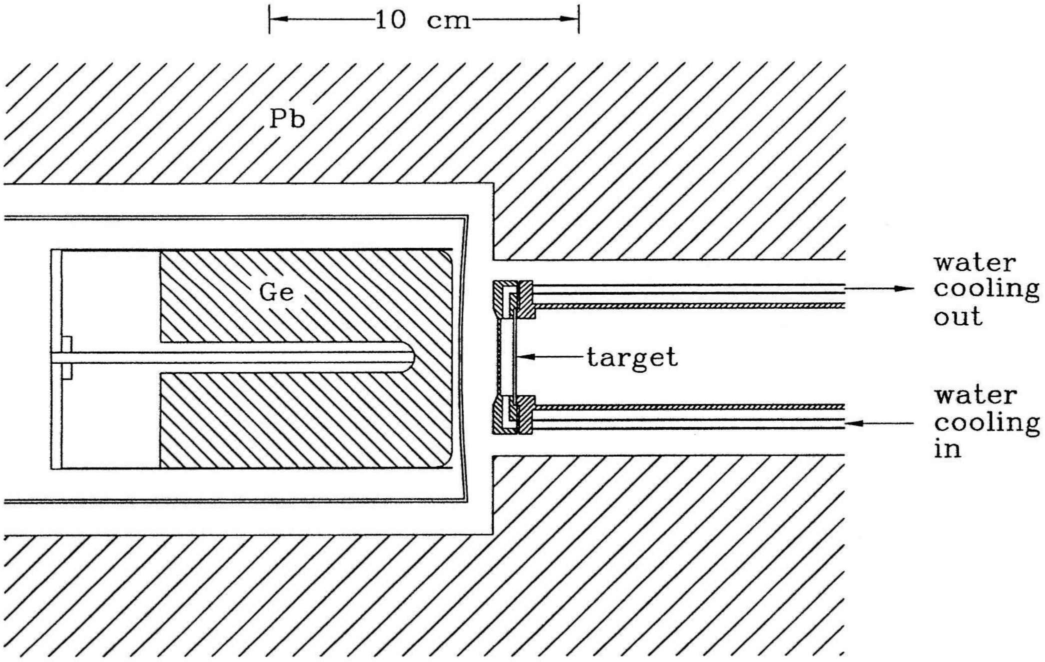

Figure 3.1: The details of geometry A, showing the perpendicular target chamber and the position of HPGe γ-ray detector.

chilled water to dissipate the beam power. The amount of material between the Ti–^{3}H layer and the γ-ray detector was made as small as practical in order to minimize γ-ray absorption. The target flange (with knife edge) and the water-cooling jacket were machined from stainless steel. The target flange was welded onto stainless-steel 3.81-cm o.d. vacuum tubing.

Two target chambers were used during the course of the experiments. The first chamber fixed the target perpendicular to the incident beam direction and was used for the experiments using targets 1, 3 and 5 which measured the γ-rays at zero degrees relative to the incident beam. This chamber is depicted in Figure 3.1. For the angular-distribution measurements using target 4, a chamber which fixed the target at an angle of 44.41° with respect to the beam direction was used. Hereafter, this chamber will be referred to as the "45-degree" target chamber. This chamber was oriented so that target substrate was rotated about the vertical diameter. The angular-distribution measurements were performed with the γ-ray detector in the horizontal plane.

For the measurements using the perpendicular target chamber with target 1, the beam was collimated by a 12.7-mm diameter Ta collimator 75 cm upstream from the target. For the measurements using this target chamber with targets 3 and 5 the same collimator was used at a distance of 62 cm upstream. For the measurements using the "45-degree" target chamber, a rectangular Ta collimator (4.0-mm horizontal × 15.9-mm vertical) was located 53 cm upstream from the target. For all measurements, a suppression ring held at -400 V was placed ≈ 12 cm downstream from the collimator. This voltage helped insure accurate beam-current integration by preventing secondary electrons from leaving the target chamber, and by preventing electrons from entering the chamber from upstream.

The target chambers were installed at the end of the South–30° beamline of the Pelletron accelerator, as shown in Figure 3.2. The beamline's cryopump maintained a base pressure of $\approx 4 \times 10^{-8}$, measured 5-cm upstream from the collimator. However, the pressure rose to $\approx 3 \times 10^{-7}$ torr when running α beams due to the presence of ^{4}He gas from the accelerator's ion source which the cryopump did not efficiently pump. The probability for charge-changing processes in the residual gas between the target-room optics and the target (which could lead to an error in beam-current integration) was calculated to be < 0.002, using tabulated [All58] charge-exchange cross sections for He^+ ions in He gas.

An inline 2.36-cm-i.d. hollow Cu tube held at LN_2 temperature was installed ≈ 20 cm upstream from the target in an attempt to reduce residual hydrocarbon vapors in the vicinity of the target. The presence of hydrocarbons in the residual gas will lead to an undesirable beam-induced carbon buildup on the target. The cold tube was used only with the experiments done with target 1 – with disappointing results: $\approx 5 \times 10^{17}$ atoms/cm^2 of carbon were observed on the surface of target 1 after the $^3\mathrm{H}(\alpha,\gamma)$ measurements. The carbon buildup observed on the targets is discussed in more detail below. After the experiments with target 1, the cold tube was removed, and the target chamber and collimator were thoroughly re-cleaned. No carbon buildup ($< 1.5 \times 10^{16}$ atoms/cm^2) was observed during the remaining experiments.

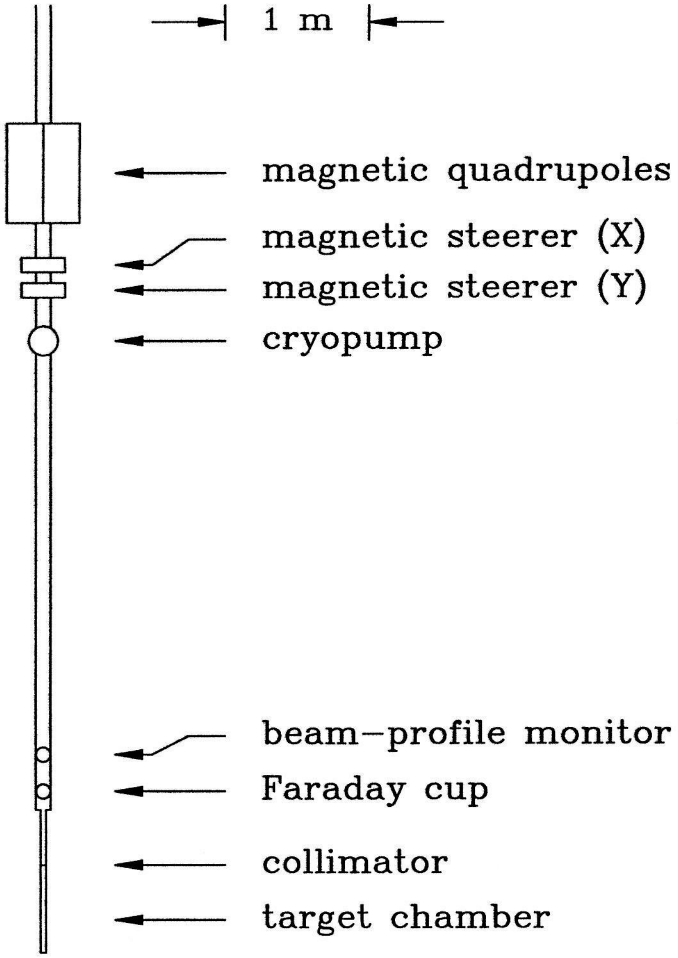

Figure 3.2: A scale diagram of the Pelletron accelerator's South–30° beamline, showing the location of the optics, vacuum system, beam-handling equipment, and target chamber.

3.2 Beam

The proton, deuteron, D_3^+, $^3He^+$, and $^4He^+$ beams were supplied by the Caltech 3-MV Pelletron Tandem Accelerator. The beam energy was defined by a 90° analyzer magnet and NMR magnetometer. The energy calibration ($\pm 0.1\%$) was established using the 483.91 ± 0.10-keV resonance [Ajz87] in $^{19}F(p,\alpha\gamma)$, the 991.86 ± 0.03-keV [End90] in $^{27}Al(p,\gamma)$, the 606.0 ± 0.5-keV resonance [Wan91] in $^{11}B(\alpha,n)$, and the 1530.03 ± 0.15-keV resonance [Maa78] in $^{24}Mg(\alpha,\gamma)$. This energy calibration was used for the experiments described in Chapter 2; the energy scale for the $^3H(\alpha,\gamma)$ measurements was deduced from energy of the capture γ-rays. The number of incident particles was determined by beam-current integration. The calibration of the integrator was tested with current sources over the range 20 nA – 30 μA, and found to be accurate within 0.5%. The effect of leakage current through the H_2O-cooling lines used during the $^3H(\alpha,\gamma)$ experiments was measured to be $< 0.5\%$.

The target chambers used for the $^3H(\alpha,\gamma)$ experiments were aligned by installing a quartz window in the target position (in place of the usual target and water-cooling jacket), and bombarding the quartz with a $\approx$ 20-nA α beam. The beam-induced fluorescence in the quartz indicated where the beam was striking the target. The target chamber and collimator were positioned so the beam, when positioned at the center of the collimator, would strike the center of the target. It was also verified that the beam was confined to the center of the target; it was found that the area of the target accessible to the beam was $\approx 50\%$ larger than the area of the collimator. The alignment was tested using α beams with energies between 200 and 1500 keV; no energy-dependent effect was noted.

The layout of the beamline components is shown in Figure 3.2. In order to bombard the target uniformly and reproducibly, the beam was rastered over the area of the collimator by the magnetic steerers. The beam was sharply focused at the collimator position (with the aid of a beam-profile monitor $\approx$ 1 m upstream from the collimator), and then amplitudes of the horizontal and vertical rasters were increased until $\approx 10\%$ of the beam struck the collimator. In addition, to help insure a reproducible trajectory, the beam was tuned so that it passed through the center of the target-room quadrupole magnets. This positioning was accomplished by tuning the beam so that the quadrupoles had no steering effect on the beam. These procedures were tested during the quartz alignment procedure, and found to yield good results. After removing the used targets, the area of the targets struck by the beam was observed to have a different appearance from the unstruck portions. For all targets, the beam spot was observed to be centered within 2 mm; for targets 1, 3, and 5 the beam spot consisted of a roughly square area of 10mm × 10mm; for target 4 (used with the "45-degree" chamber), the rectangular beam spot (on the target) was roughly 6 mm (horizontal) × 17 mm (vertical).

The energy of the incident α beam was varied between 140 and 2790 keV during the ^{3}H(α,γ) experiments. In order to achieve this range of energy, the pressure of the insulating SF_6 gas in the accelerator's pressure vessel was varied between 10 and 60 psi. In addition, a variable length of the accelerating tube could be shorted in order to increase the voltage gradient for a fixed terminal potential. This technique was essential for the obtaining the needed beam intensity and stability at low terminal potentials. For example, at $E_\alpha = 140$ keV and with 8/9 of the accelerating tube shorted, we averaged 19 μA on target for 11.5 hours. The beam intensities varied between 5 and 30 μA over the course of the experiment.

3.3 γ-Ray Detection

Gamma rays were detected using an 85% relative-efficiency high-purity Ge detector (ORTEC serial no. 31-TP40242A). The signals were processed by an ORTEC Model 972 spectroscopy amplifier and stored in a 4096-channel analyzer (Tracor-Northern TN-7200). The spectra were transferred to a computer for off-line analysis. The energy resolution of the detector was typically 2.1 keV at $E_\gamma = 1332$ keV.

3.3.1 Detector Geometries

The detector was used in three different setups. Using targets 1, 3, and 5 and the perpendicular target chamber, extensive (α, γ) measurements were performed with the detector at 0° in close geometry for maximum efficiency (source to crystal front face 2.1 cm). A 1.02-cm lucite spacer-ring mounted flush between target's water-cooling jacket and the detector housing's front face insured precise reproducibility of the detector – target distance. This setup (hereafter referred to as geometry A) is depicted in Figure 3.1.

In anticipation of large coincident-summing corrections and/or angular-distribution-attenuation effects, measurements were also performed at 0° on targets 1, 3, and 5 using the perpendicular target chamber with the detector much farther away, where these effects would be minimal (source to crystal front face 11.6 cm; hereafter referred to as geometry B). This change only required the moving of the detector.

For the angular-distribution measurements using target 4, the "45-degree" target chamber was used. The γ-ray detector was placed on a rotating table whose rotation axis was placed directly below the target position. A fairly large source – detector distance was used in order minimize attenuation of any anisotropy of the angular distribution (source to crystal front face 10.1 cm). The detector could be placed at five different angles: 0°, -45°, -90°, $+90^\circ$, and $+135^\circ$. This setup (geometry C) is depicted in Figure 3.3. It is estimated that the uncertainty in the angular positions is $\pm 2^\circ$. In this case the geometry was much easier to reproduce, as target or radioactive-source changes could be made without moving the detector.

3.3.2 Photopeak-Efficiency Measurements

The photopeak efficiency, ε, for a particular geometry is defined as the probability of a γ ray emitted by an isotropic source depositing its full energy in the Ge crystal. The photopeak efficiency was determined for the needed range of γ-ray energies in each

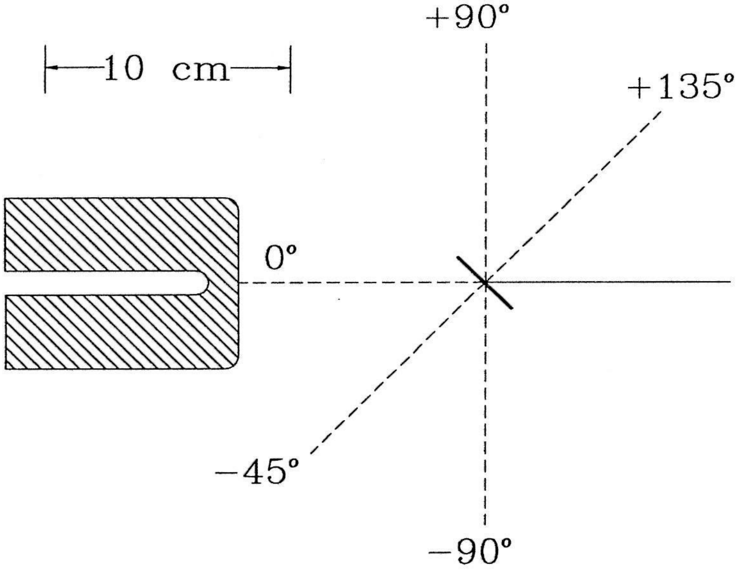

Figure 3.3: A scale diagram of geometry C, showing only the target and sensitive Ge.

geometry (including each angle for the angular-distribution setup) using the following sources: ^{152}Eu, ^{56}Co, and ^{24}Na. The commercially prepared ^{152}Eu source covers the range $122 \leq E_\gamma \leq 1408$ keV. The source was taped onto a blank Cu substrate which was sealed in the target position for the efficiency measurements.

The ^{56}Co source was produced via the ^{56}Fe$(p,n)^{56}$Co reaction by bombarding a 0.51-mm-thick Fe disk with 1 mC of 5950-keV protons using a different beamline. The source was installed in the target position with a 0.25-mm-thick Cu disk behind it (the γ-ray absorption of this combination is very close to that for 0.81-mm-thick Cu). The primary advantage of this source is that it extends the calibration to higher energies: it covers $847 \leq E_\gamma \leq 3548$ keV. The strength of this source was determined to be 2350 decays/sec by comparison with other sources.

The isotope ^{24}Na has a relatively short half-life (15 hours), and emits two γ-rays (1369 and 2754 keV) per decay in one-to-one coincidence (other decays take place $\approx 0.06\%$ of the time). Using the coincident-sum peak and the two photopeaks, the absolute strength of the source can be determined as described in Chapter 4. The ^{24}Na was produced using the ^{23}Na$(d,p)^{24}$Na reaction.

For the perpendicular target chamber, the ^{24}Na was produced in the "45-degree" chamber, using a different beamline, and then transferred to the perpendicular chamber for counting. A target consisting of unknown amount of Na_2WO_4 evaporated on a 0.81-mm-thick Cu disk was bombarded by 2000-keV deuterons, producing an initial activity of $\approx 2 \times 10^5$ decays/sec.

In the case of the "45-degree" target chamber used for the angular-distribution measurements, the ^{24}Na was produced in the target chamber. The γ rays from a source produced in this way should have the same spatial distribution as the γ-rays from the ^{3}H(α,γ) reaction, because the same collimator and beam-tuning procedures were used. The target was prepared by evaporating 1 mg/cm^2 Na_2WO_4 onto a 0.81-mm-thick Cu disk. Using the technique of Skelton and Kavanagh [Ske84], a 1-mg/cm^2 Au layer was then evaporated over the Na_2WO_4 in order to insure that all of the ^{24}Na produced would remain in the target. The source was produced by bombarding the target with 1.1 mC of 2200-keV deuterons, producing an initial activity of $\approx 1.3 \times 10^5$ decays/sec. One concern about using this technique was neutron damage to the Germanium crystal caused by neutrons from (d,n) reactions. According to the detector instruction manual, a cumulative neutron flux of $\geq 10^8$ n/cm^2 on the detector will cause degradation of resolution. During production, the γ-ray detector was rotated 180° in its dewar (to increase the distance from the target to detector), and the target and detector were heavily shielded with borated paraffin. Using a portable neutron monitor, it was estimated that the detector received $\approx 2 \times 10^4$ n/cm^2 during the ^{24}Na production. It was determined that $< 0.04\%$ of the ^{24}Na was lost from the target by measuring the background after removing the the target. The ^{24}Na-efficiency measurements were performed both before and after the ^{3}H(α,γ) angular-distribution measurements.

Care was taken during the γ-ray calibrations to use the same Pb-shielding arrangement as during the ^{3}H(α,γ) measurements, so that the total efficiency, which is needed for making coincident summing corrections, was the same. The analysis of the photopeak-efficiency calibration data is described in Chapter 4, and the results are plotted in Appendix E.

3.3.3 Photofraction Measurements

The photofraction, ϕ, is defined as the ratio of photopeak efficiency to total efficiency, η. The total efficiency for a particular geometry is defined as the probability of a γ-ray emitted by an isotropic source depositing any energy in the Ge crystal. The total efficiency includes events where γ-rays interact in the Ge crystal, but do not deposit their full energy, as well as events where radiation is scattered into the detector by material in the vicinity of the target and detector (possible "scattering" mechanisms include the Compton effect, pair production, 511-keV radiation from the annihilation of positrons, bremsstrahlung, and X-ray fluorescence). It is clear that the presence of the target chamber and Pb shielding increases the total efficiency relative to a bare detector.

In order to make (η-dependent) coincident-summing corrections to the ^{3}H(α,γ) and $\varepsilon(E_\gamma)$ measurements, the photofraction as a function of E_γ was measured using various sources. An ideal source would emit isotropic, monoenergetic γ rays, with no other radiation. In practice, such sources are rare, so use has been made of several "non-ideal" sources, with appropriate corrections. Due to the presence of noise in the detector electronics, a low-energy threshold (13-100 keV, depending on gain settings) was required in the detector spectrum. The extrapolation of the spectra to zero pulse height involved a correction of 3–9%. The spectra were corrected for background from the room as well as source impurities and non-coincident γ rays from the source. Most of the measurements were performed in geometry A, where coincident-summing effects were most important.

A ^{57}Co source ($E_\gamma = 122$ keV) was produced via ^{56}Fe$(d,n)^{57}$Co by bombarding a 0.51-mm-thick Fe disk with 30 mC of 4000 keV deuterons. The source was installed in the perpendicular target chamber using the 0.25-mm-thick Cu disk as described in Subsection 3.3.2 for the ^{56}Co source.

A source of ^{51}Cr ($E_\gamma = 320$ keV) was prepared using the ^{51}V$(p,n)^{51}$Cr reaction. A target consisting of 0.4 mg/cm^2 V evaporated onto a 0.81-mm-thick Cu disk was bombarded by 61 mC of 2180 keV protons.

A ^{198}Au source ($E_\gamma = 412$ keV) was produced by thermal-neutron activation of a 25-μm-thick, 1.1-cm diameter Au foil using a ^{252}Cf neutron source and H_2O moderator at an undergraduate physics laboratory on campus.

The ^{7}Li(p,p_1) reaction at $E_p = 1200$ keV was used as a source of 478-keV γ rays. The target was prepared by evaporating ≈ 5 μg/cm^2 Li on a 0.81-mm-thick Cu disk. Lithium-hydride was used as the evaporation source material; the evaporated film was a metallic grey color assumed to be metallic Li. Upon exposure to air the film became translucent, presumably reacting to form LiOH.

The ^{12}C$(p,\gamma)^{13}$N reaction at $E_p = 461$ keV was used to provide 2370 keV γ-rays. The γ rays were produced by a steady 1-μA bombardment of a target consisting of ≈ 2 μg/cm^2 C on a 0.81-mm-thick Cu disk. The spectra required correction for the unavoidable background arising from ^{13}N(β^+) decay. By acquiring timed spectra with the beam off and on target, and using the known half-life and ^{13}N production rate, the required correction was readily made.

The $\phi(E_\gamma)$ measurements were extended to $E_\gamma = 6130$ keV using the ^{19}F$(p,\alpha\gamma)$ reaction at $E_p = 340$ keV. A 1.5-μg/cm^2 LiF target on a 0.81-mm-thick Cu disk was used as the target; no effects from the ^{7}Li(p,γ) reaction were observed. The ^{19}F(p,α_π) reaction, which populates the pair-emitting first excited state of ^{16}O, is not resonant at this energy, and is expected to make a negligible contribution to the detected spectrum.

Additional measurements were made using the following commercially prepared sources: ^{137}Cs ($E_\gamma = 662$ keV), ^{54}Mn ($E_\gamma = 835$ keV), and ^{60}Co ($E_\gamma = 1172$ and 1332 keV). The 1172- and 1332-keV γ rays from ^{60}Co are emitted in one-to-one coincidence; because the energies are fairly close together, the data were analyzed using ϕ(1172 keV) / ϕ(1332 keV) fixed at at a value determined from other sources. Coincident-summing corrections were also made to the data as described in Chapter 4. The results from the ^{24}Na source (Subsection 3.3.2) were used to obtain ϕ(2754 keV) by using $\phi(E_\gamma)$ from other sources to estimate ϕ(1369 keV) and making coincident-summing corrections.

It should be noted that the commercial sources were prepared on 0.3- to 1.0-mm stainless-steel or plastic backings. The presence of the extra material could cause increased scattering into the detector, systematically lowering the measured ϕ. Monte Carlo simulations (Chapter 4) indicate that the effect of the source backing is $\leq 5\%$. No corrections were made for this effect. The results for geometry A are shown in Figure 3.4; the error bars reflect estimated systematic uncertainties. The solid curve is an empirical fit used in subsequent analysis. Also shown are the experimental results from geometry B; the solid curve was used in the analysis of data using geometries B and C.

3.3.4 γ-Ray Energy Calibration

At low energies, the ^{3}H(α,γ) cross section is strongly energy-dependent due to the coulomb barrier. An accurate determination of the mean reaction energy is thus very important. The mean reaction energy was determined from the centroid of the γ_0 peak and reaction kinematics (the details of the analysis are described in Chapter 4). An accurate determination of the detector's energy calibration is a crucial ingredient in this determination, particularly in the range $2500 \leq E_\gamma \leq 2700$ keV, corresponding to the lowest-energy ^{3}H(α,γ) measurements.

The energy calibration was primarily based upon the accurately known ^{24}Na lines at $E_\gamma = 1368.633(6)$ and 2754.030(14) keV [Gre79]. The calibrations were performed daily during the ^{3}H(α,γ) experiments by placing a ^{24}Na source as near the target position as practical. The calibrations were also performed before and after most low-energy ($E_{c.m.} \leq 150$ keV) measurements. Gain shifts were observed to be less than 0.2 keV in almost all cases (a change in calibration of ≈ 1 keV at 2754 keV was observed during run 096). The calibration was taken to be a linear fit to the centroids of the two ^{24}Na lines.

The duration of the low-energy runs was long enough to acquire sufficient statistics in the radio-thorium background line at 2614.533(13) keV [Gre79] to test the calibration. The measured energy was within 0.2 keV of the correct value in all cases.

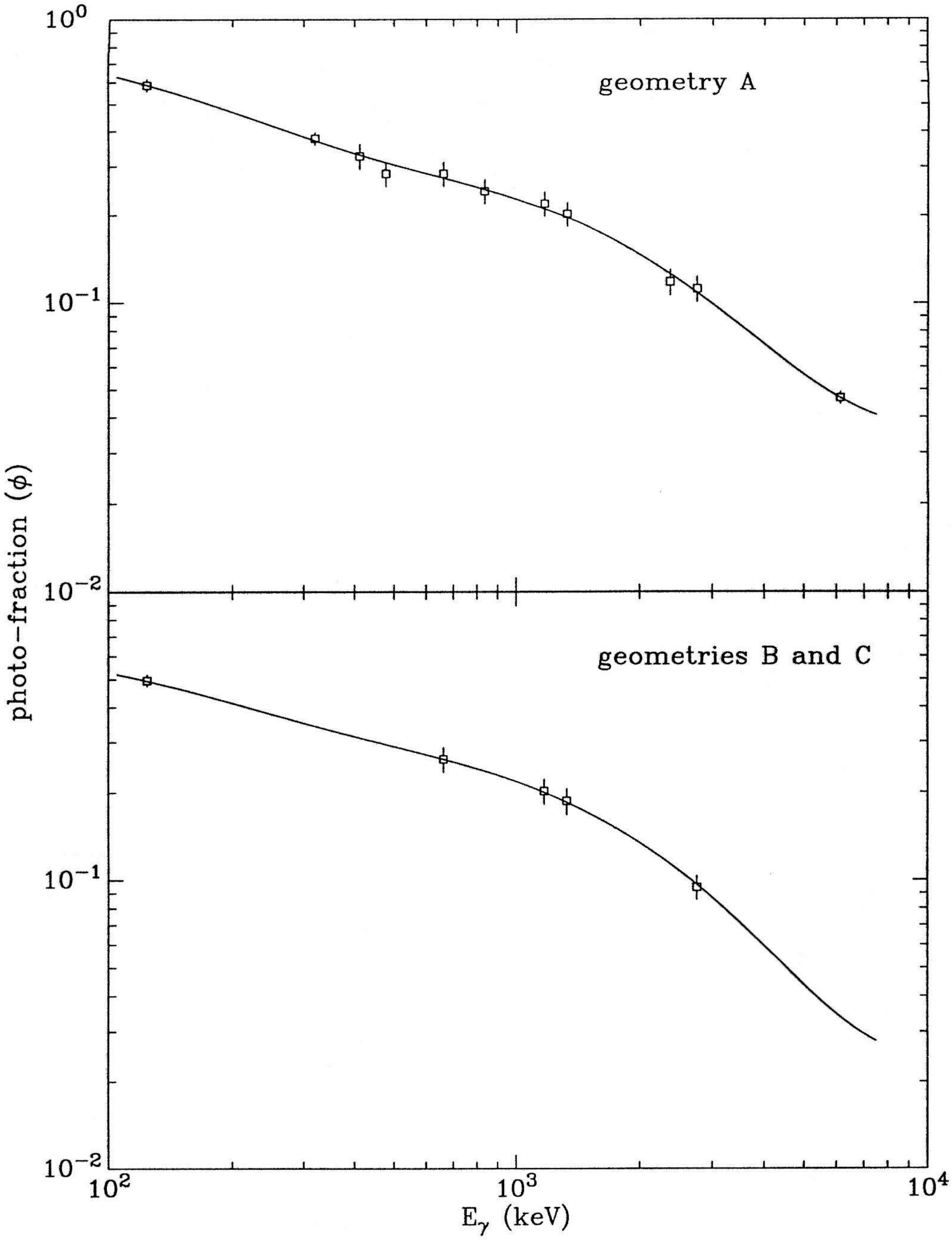

Figure 3.4: The photofraction for geometry A is shown in the upper panel. The squares are the experimental points, and solid line is the curve used in subsequent analysis. The squares on the lower panel are the experimental results for geometry B; the solid curve on the lower panel is used in the subsequent analysis for geometries B and C.

The energy calibration for run 096 (during which the gain shifted slightly) was fit using this line.

Tests using ^{56}Co and ^{152}Eu sources indicated that the straight-line fit from ^{24}Na described the calibration within 0.5 keV over the range $400 \leq E_\gamma \leq 3500$ keV. The energy calibration in the range $2500 \leq E_\gamma \leq 2700$ is assigned a 0.3-keV systematic uncertainty.

3.3.5 Detector Shielding

The natural γ-ray environment gives rise to background extending to $E_\gamma = 2614$ keV. At higher energies, the detector background is primarily due to cosmic-ray muons.

The most important regions of the ^{3}H(α,γ) spectrum are $E_\gamma \approx 478$ keV (γ_2 transition) and $2000 \leq E_\gamma \leq 2700$ keV (capture transitions for low incident energies). For $E_\alpha \lesssim 400$ keV, it was anticipated that beam-induced background would be negligible due to the large coulomb barrier for α-induced reactions on contaminants in the targets.

The detector was initially set up in geometry A with $\approx$ 10 cm Pb shielding in every direction (except the direction of the incident beam). In addition, a 65-cm × 58-cm × 2.5-cm-thick plastic scintillator paddle was centered over the detector, and used to reject cosmic-ray events. A background spectrum obtained with this setup is shown in Figure 3.5; also shown are the results for the detector with and without the Pb shielding. With 10-cm Pb in place, the cosmic-ray veto reduced the background by an additional factor 2 at $E_\gamma = 2550$ keV, but only 20% at $E_\gamma = 478$ keV. Also note that the Pb shielding has little effect on the background for $E_\gamma > 2614$ keV.

When the ^{3}H$(\alpha,\gamma)^7$Li experiments were performed with target 1, it was found that there was significant beam-induced background in the low-energy runs. For example, at $E_\alpha = 200$ keV the background at $E_\gamma = 2700$ keV was a factor of 13 higher with beam compared to without. It was determined that the background was due to neutrons from the ^{3}H$(^3$H$, 2n)\alpha$ reaction, where the ^{3}H projectiles resulted from ^{3}H$(\alpha, ^3$H$)$ elastic scattering. This effect is discussed in more detail in Appendix B.

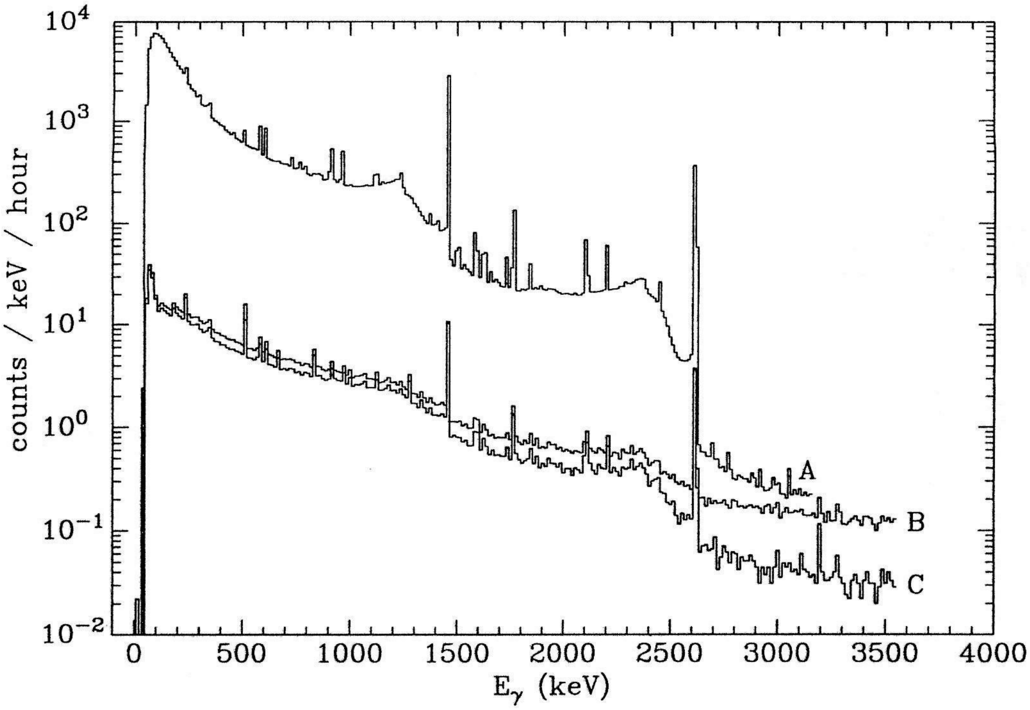

Figure 3.5: The γ-ray detector (beam-off) background. The highest curve (A) is the result for no detector shielding. The middle curve (B) is the result for $\approx$ 10-cm Pb shielding. The lowest curve (C) is for Pb shielding identical to curve B and cosmic-ray veto. The spectra have been re-binned to reduce statistical fluctuations.

This additional background made the effect of the cosmic-ray veto negligible, so it was discontinued for the remaining experiments. For the angular-distribution measurements, only 5 cm of Pb shielding was used, except for the E_α = 290-keV runs, where it was increased to 10 cm.

3.4 Procedure

After each target was made, its ^{3}H and Ti areal densities were determined as described in Chapter 2. The target was then installed in the target chamber for (α, γ) measurements. The incident beam energies were chosen so that the 2614-keV background line would not interfere with the capture γ rays. For each run, the incident charge, time, NMR magnetometer reading, and the γ-ray spectrum were saved; a summary of all runs is given in Appendix C. The most extensive measurements were performed

Target	Q (C)	^{3}H (before) (10^{17}/cm^{2})	^{3}H (after) (10^{17}/cm^{2})
1	1.573	5.52(4)	5.36(6)
3	1.036	1.32(2)	1.32(4)
4	5.905	4.33(4)	2.55(11)
5	0.690	3.23(3)	2.97(3)

Table 3.1: Summary of measured target deterioration. The column labeled Q gives the total α^{+} charge incident on each target. The "after" results have been corrected for ^{3}H(β^{-}) losses. The numbers in parentheses are the estimated relative uncertainties in the least significant figures.

using target 1. Targets 3 and 5 were primarily used to test the reproducibility of the absolute cross section and to make additional measurements at low energies. Many repeated measurements at $E_{\alpha} = 1000$ keV were performed to test for possible target deterioration over time. Measurements using targets 1, 3, and 5 were made in geometries A and B for each. The measurements using target 4 were made in geometry C.

The ^{3}H areal-density determinations using ^{3}H(d, α) were repeated after the (α, γ) measurements for targets 1, 3, and 5. The areal density of target 4 was observed to deteriorate by $\approx 40\%$ over the course of the experiment, as evidenced by the decrease in yield at $E_{\alpha} = 1000$ keV. The before-and-after results are shown in Table 3.1. The corrections for target deterioration are described in Chapter 4.

During the experiments with target 1, the capture γ rays for the repeated $E_{\alpha} =$ 1000-keV runs were at a slightly lower energy in the later runs compared to the earlier runs. It was suspected that this energy shift was due to a buildup of carbon on the target. This speculation was confirmed by measuring γ rays from the ^{12}C(p, γ) resonance at $E_{p} = 461$ keV.

The carbon layer was studied with an α beam by measuring neutrons from the ^{13}C(α, n) reaction. The measurements were performed using the "45 degree" target chamber and a polyethylene-moderated neutron detector [Wre94] at the 0° beamline. The beam collimation was carefully adjusted to reproduce the beamspot of the (α, γ)

measurements. The results from the vicinity of the $E_\alpha = 1053$-keV resonance are shown in Figure 3.6; also shown are the results from a pure ^{13}C foil [Bru92] taken under nearly identical conditions. The resonance profile indicates that either the carbon layer is not uniform, or that the carbon is mixed with the target material. We believe that the former explanation is most likely. The (p,γ) and (α,n) measurements consistently indicated the existence of a carbon layer of 5×10^{17} atoms/cm^2, averaged over the area of the beamspot.

The carbon buildup problem was corrected as described in Section 3.1. The ^{12}C(p,γ) measurements indicated that $< 1.5 \times 10^{16}$ atoms/cm^2 of carbon was deposited on the remainder of the targets.

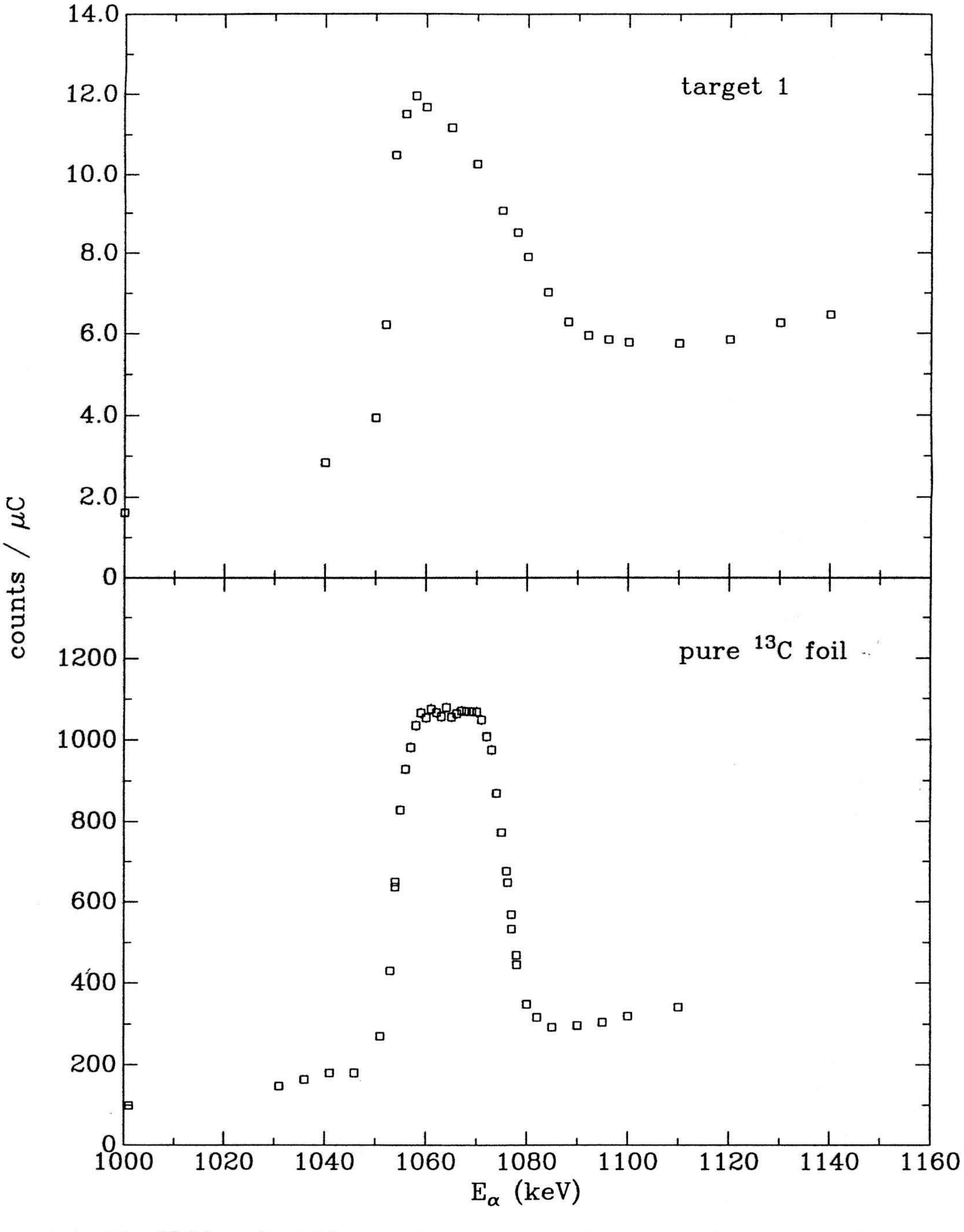

Figure 3.6: The $^{13}C(\alpha, n)$ yields are shown in the vicinity of the 1053-keV resonance. The upper panel is the result for target 1; the lower for a pure ^{13}C foil. Note that natural carbon is $\approx 1.1\%$ ^{13}C.

Chapter 4

Data Analysis

The data analysis consists of finding the absolute γ-ray yields, and then normalizing by the ^{3}H areal density and number of incident particles to obtain cross sections. The determination of the effective reaction energy from the observed energy of the γ_0 transition is also important. The reaction kinematics are discussed in Section 4.1. The γ-ray analysis is then described in Section 4.2. In Section 4.3 the small corrections for target deterioration due to beam damage and ^{3}H decay are discussed. Finally, the pieces are put together, and the cross sections are extracted in Section 4.4.

4.1 Kinematics

The energy of the capture γ rays as a function of the α-particle lab energy E_α and the lab angle θ_L is given by

$$E_\gamma(E_\alpha, \cos\theta_L) = \frac{Q(M_T + M_\alpha + M_7) + 2M_T E_\alpha}{2[M_T + M_\alpha + E_\alpha - \cos\theta_L \sqrt{E_\alpha(E_\alpha + 2M_\alpha)}]}, \tag{4.1}$$

where M_T, M_α, and M_7 are the rest masses (in energy units) of the ^{3}H, α, and ^{7}Li final state. The ^{7}Li nucleus may be left either in its ground or first excited state ($E_x = 477.61$ keV [Ajz88]). The masses and Q-value, $Q = M_T + M_\alpha - M_7$, are taken from a recent evaluation [Wap93]. The ground-state Q-value used (2467.9 ± 0.7 keV) is significant because it is used in the extraction of the effective reaction energy from the observed γ_0 energy. The error in Q leads to a ± 0.7-keV systematic uncertainty in the center-of-mass energy. This Q-value and its uncertainty are derived directly from the ^{7}Li mass excess ($\Delta = 14906.9 \pm 0.7$ keV), since the uncertainties in the ^{3}H and ^{4}He mass excesses are negligible in comparison.

The differential cross section in the center-of-mass system is given by

$$\frac{d\sigma_i}{d\Omega_{c.m.}} = \frac{\sigma_i}{4\pi} W^i_{c.m.}(\theta_{c.m.}), \tag{4.2}$$

where σ_i is the total cross section for producing γ_i. The normalized angular distribution, $W^i_{c.m.}$, is expanded in Legendre polynomials

$$W^i_{c.m.} = 1 + \sum_{\ell=1}^{\infty} a^i_\ell P_\ell(cos\theta_{c.m.}). \tag{4.3}$$

The decay of the $\frac{1}{2}^-$ first excited state is isotropic and uncorrelated with the feeding γ-ray; hence the a^2_ℓ should be identically zero. The lab and center-of-mass angles are related by

$$cos\theta_{c.m.} = \frac{\cos\theta_L - \beta}{1 - \beta\cos\theta_L} \tag{4.4}$$

and

$$\frac{d\Omega_{c.m.}}{d\Omega_L} = \frac{1-\beta^2}{(1-\beta\cos\theta_L)^2}, \tag{4.5}$$

where the relativistic parameter β is given by

$$\beta = \frac{\sqrt{E_\alpha(E_\alpha + 2M_\alpha)}}{M_T + M_\alpha + E_\alpha}. \tag{4.6}$$

The differential cross section in the lab system is

$$\frac{d\sigma_i}{d\Omega_L} = \frac{\sigma_i}{4\pi} W^i_L(\theta_L), \tag{4.7}$$

where the normalized angular distribution in the lab system is calculated from Equation 4.3 using Equations 4.4 and 4.5:

$$\begin{aligned} W_L^i &= 1 + 2\beta P_1(\cos\theta_L) + \sum_{\ell=1}^{\infty} a_\ell^i \Big\{ P_\ell(\cos\theta_L) + \frac{\beta}{2\ell+1}\Big[(\ell+1)(\ell+2)P_{\ell+1}(\cos\theta_L) \\ &\quad -\ell(\ell-1)P_{\ell-1}(\cos\theta_L)\Big]\Big\}, \end{aligned} \tag{4.8}$$

to first order in β. Note that $\beta \leq 0.022$ in this experiment, so this is an excellent approximation.

The lifetime of the first excited state of ^{7}Li ($\tau = 105 \pm 3$ fs [Ajz88]) is such that the ion velocity is significantly reduced (on average) before decaying. We use $\beta_{eff} = 0.75\beta$ for this transition, where 0.75 is the Doppler-shift attenuation factor found [Pau66] for this state with similar-velocity ^{7}Li ions stopping in Ni.

The center-of-mass kinetic energy E is related to E_α via

$$E_\alpha = \frac{2(M_T + M_\alpha)E + E^2}{2M_T}. \tag{4.9}$$

For use in subsequent error analysis, we note the following two approximate relations:

$$\frac{dE_\gamma}{d\cos\theta_L} \approx \beta(E + Q) \tag{4.10}$$

and

$$\frac{dE_\gamma}{dE} \approx 1 + \frac{\beta\cos\theta_L}{2}(3 + \frac{Q}{E}). \tag{4.11}$$

4.2 γ-Ray Detection

4.2.1 Analysis of Spectra

Examples of the γ-ray spectra obtained are shown in Figures 4.1 and 4.2 (at the lowest energy measured); Figures 4.3 and 4.4 (at an intermediate energy); and Figures 4.5 and 4.6 (at the highest energy). The γ-ray peaks were analyzed using a technique

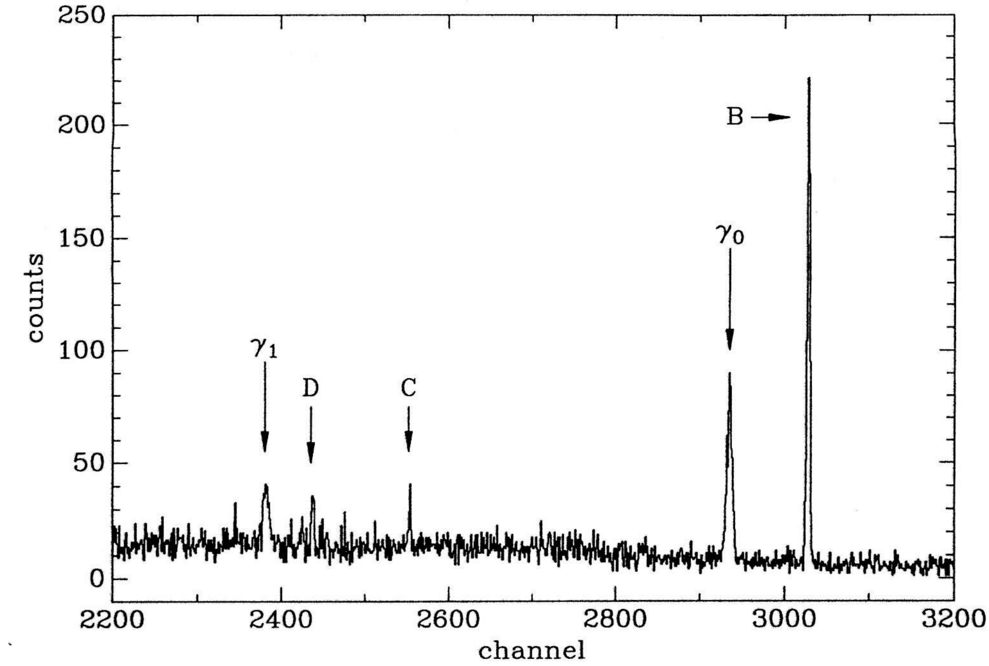

Figure 4.1: High-energy portion of run 096 spectrum obtained with target 5 and $E_\alpha = 140$ keV, showing the γ_0 and γ_1 transitions. The peak labeled B is a background line at 2614 keV from ^{208}Tl decay (^{232}Th decay product). Peak C is a background line at 2204 keV from ^{214}Bi decay (^{226}Ra decay product). Peak D is the first-escape peak associated with peak B.

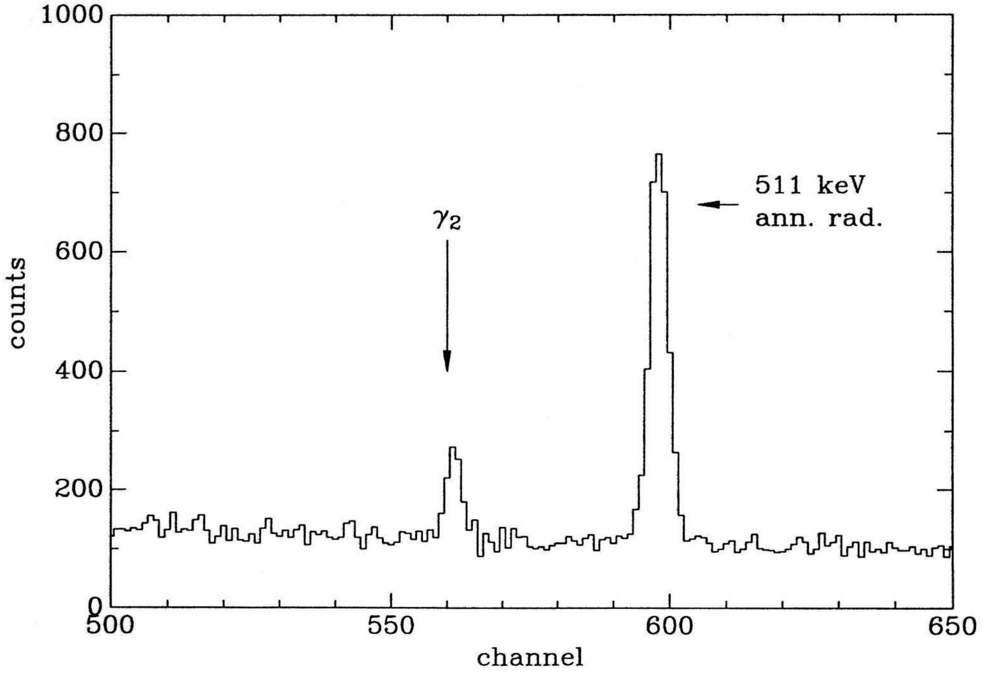

Figure 4.2: Low-energy portion of run 096 spectrum, showing the γ_2 transition and the 511-keV positron annihilation peak.

similar to that described in Appendix B of J. L. Osborne's thesis [Osb83]. The background under each peak was estimated by making a linear fit to user-defined background regions on both sides of the peak. The least-squares fitting was performed iteratively. The error ΔN in the number of counts in a channel N was $\Delta N = 1/\sqrt{N}$ for the first pass, and for subsequent passes the errors were generated from the fit, $\Delta N = 1/\sqrt{N_{fit}}$. This was done to avoid improper weighting when there are only zero or a few counts in each channel. Then the number of counts in the peak and the peak centroid (with statistical errors) were extracted using a user-defined peak region. The centroid was converted to a mean γ-ray energy using the calibration described in Subsection 3.3.4.

In almost all cases, the ^{3}H(α,γ) peaks were free from background lines, and the background was only a slowly varying continuum, which was fit as described above. In a few cases, the γ_1 peak included a contribution from a room-background line. These cases were easily handled by subtracting from the peak area the contribution measured during beam-off background measurements. In the angular distribution measurements with $E_\alpha \geq 1500$ keV and detector angles $-45°$, $-90°$, $+90°$, or $+135°$, the capture γ-ray peaks were Doppler-broadened such that the first-escape peak from γ_0 interfered with the γ_1 peak (see, for example, Figure 4.5). These cases were treated by extracting the combined number of counts in the γ_0 first-escape and γ_1 peaks, and then subtracting the γ_0 first-escape contribution calculated from the number of counts in the γ_0 peak and the ratio of first-escape to photopeak. This ratio was determined for geometry C using the ^{56}Co source and the 0° ^{3}H(α,γ) data (where the Doppler-broadening was much smaller).

The only beam-induced background lines identified in the spectra were traced to the ^{10}B$(\alpha,p\gamma)$ and Ti(α,α') reactions, both of which were observed for $E_\alpha \geq$ 1500 keV. There was no case in which these lines interfered with ^{3}H(α,γ) peaks.

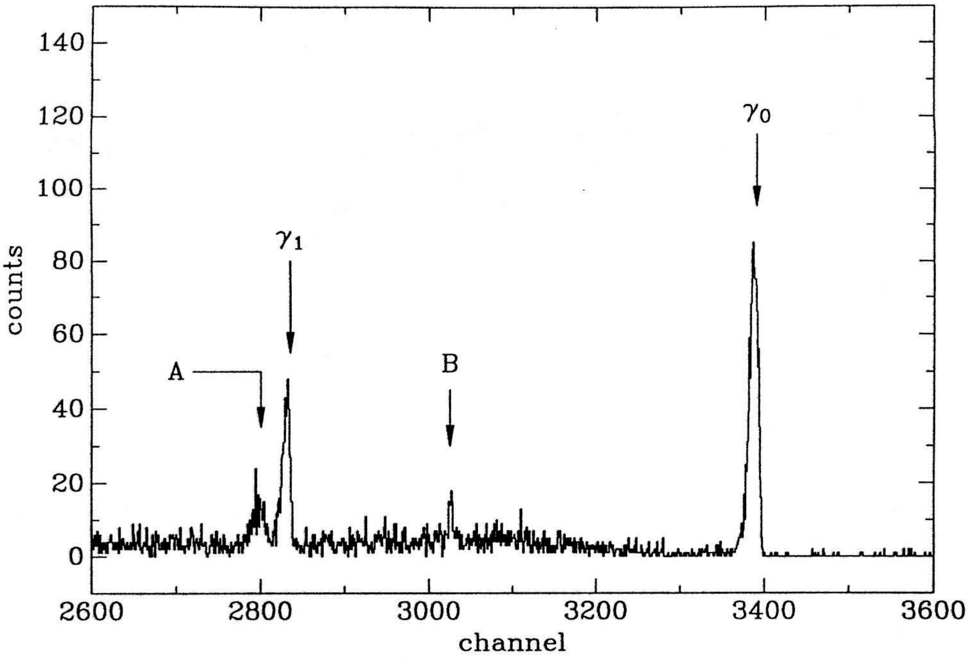

Figure 4.3: High-energy portion of run 095 spectrum obtained with target 5 and E_α = 1000 keV, showing the γ_0 and γ_1 transitions. The peak labeled A is the γ_0 first-escape peak; peak B is a background line at 2614 keV from ^{208}Tl decay (^{232}Th decay product). The energy calibration is the same as for run 096 (Figures 4.1 and 4.2).

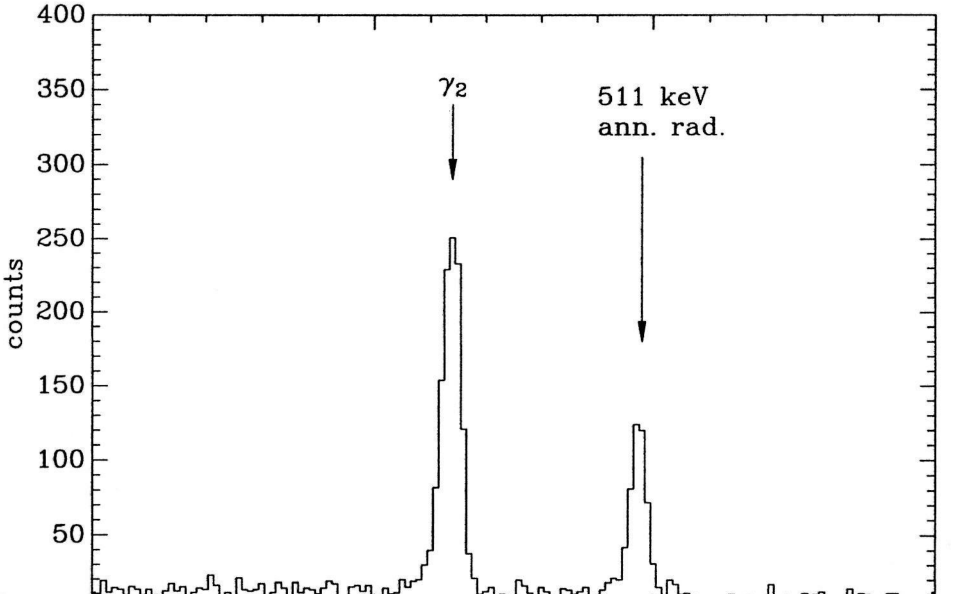

Figure 4.4: Low-energy portion of run 095 spectrum, showing the γ_2 transition and the 511-keV positron annihilation peak.

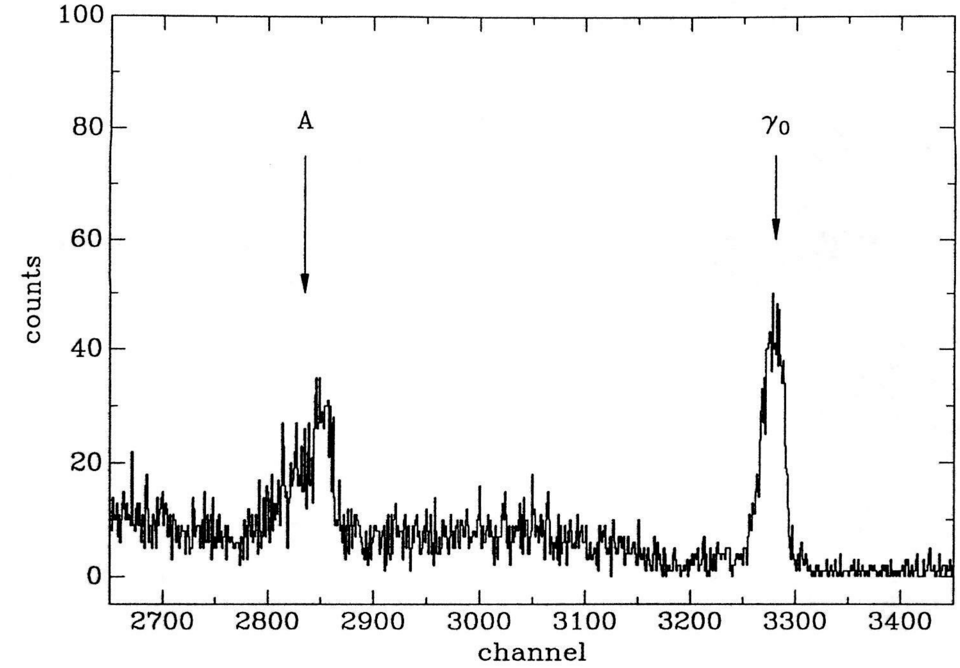

Figure 4.5: High-energy portion of run 137 spectrum obtained with target 4 and $E_\alpha = 2790$ keV, with the detector in the $-90°$ position. The γ_0 transition is cleanly resolved, but the γ_1 transition and the first-escape peak from the γ_0 transition overlap (peak A). The energy calibration is different from runs 095 and 096 (Figures 4.1–4.4).

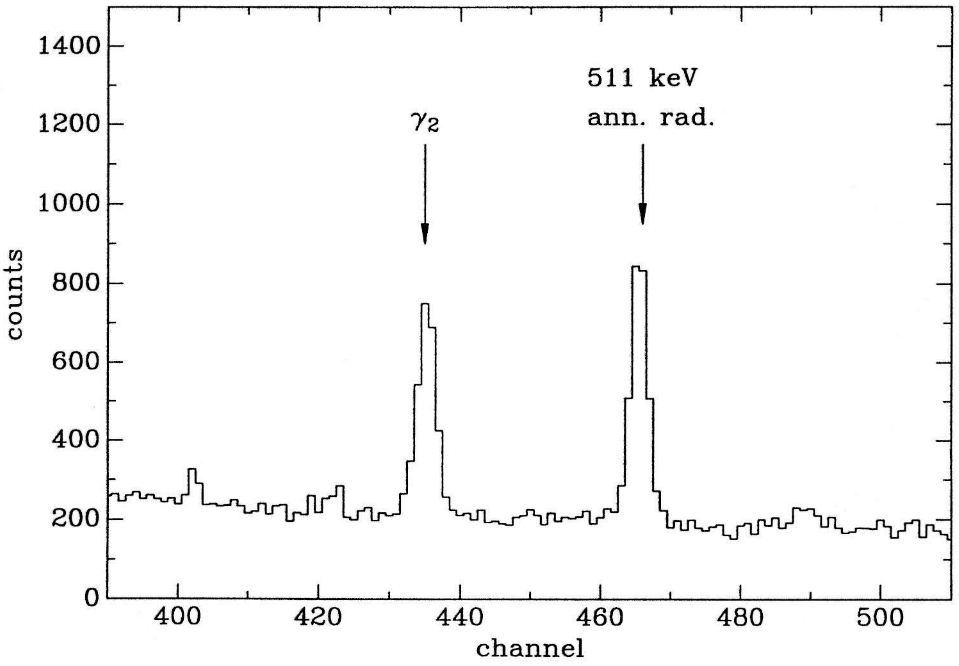

Figure 4.6: Low-energy portion of run 137 spectrum, showing the γ_2 transition and the 511-keV positron annihilation peak.

4.2.2 Monte Carlo Simulations

Monte Carlo simulations of the γ-ray detector response were used to supplement the information found using radioactive sources. In particular, one can determine the distribution of γ-ray emission angles for detected γ rays using the simulation. This information is important for making finite detector-size corrections to the angular distributions, and also for extracting the effective reaction energy from the observed energy of the γ_0 transition. This information is not readily attainable experimentally from radioactive sources. The simulations were performed using the *Electron Gamma Shower* (EGS4) code developed at Stanford [Nel85].

The details of the target chamber, detector, and Pb shielding (as shown for example in Figure 3.1) were included in the simulation. All simulations were performed using an isotropic, mono-energetic source, uniformly distributed over the experimental beamspot (Section 3.2). The simulations reproduced the measured photopeak efficiency ε and photofraction ϕ within 15% over the range $120 \leq E_\gamma \leq 3500$ keV for each geometry. Over the range $2000 \leq E_\gamma \leq 3500$ keV, the agreement was within about 5%.

For each γ ray interacting with the detector, the energy deposited in the detector and the γ-ray emission angle θ_γ were saved. The $0°$ direction is defined by a line from the center of the target, through the center of the detector. The results for 2750-keV γ rays and geometry A is shown in Figure 4.7. Note that a photopeak event's first and subsequent interactions must all take place within the active Ge, and hence are confined to $\cos\theta_\gamma \geq 0.5$ by the beamspot – detector geometry. From the distribution of all detected events it is clear that scattering "in" to the detector is significant.

Using the simulated distributions of γ-ray emission angles, the angular-distribution attenuation factors [Ros53] are easily calculated:

$$Q_\ell = \frac{1}{N}\sum_{i=1}^{N} P_\ell(\cos\theta_{\gamma i}), \tag{4.12}$$

where N is the number of detected events, $\cos\theta_{\gamma i}$ is $\cos\theta_\gamma$ of the i^{th} detected event,

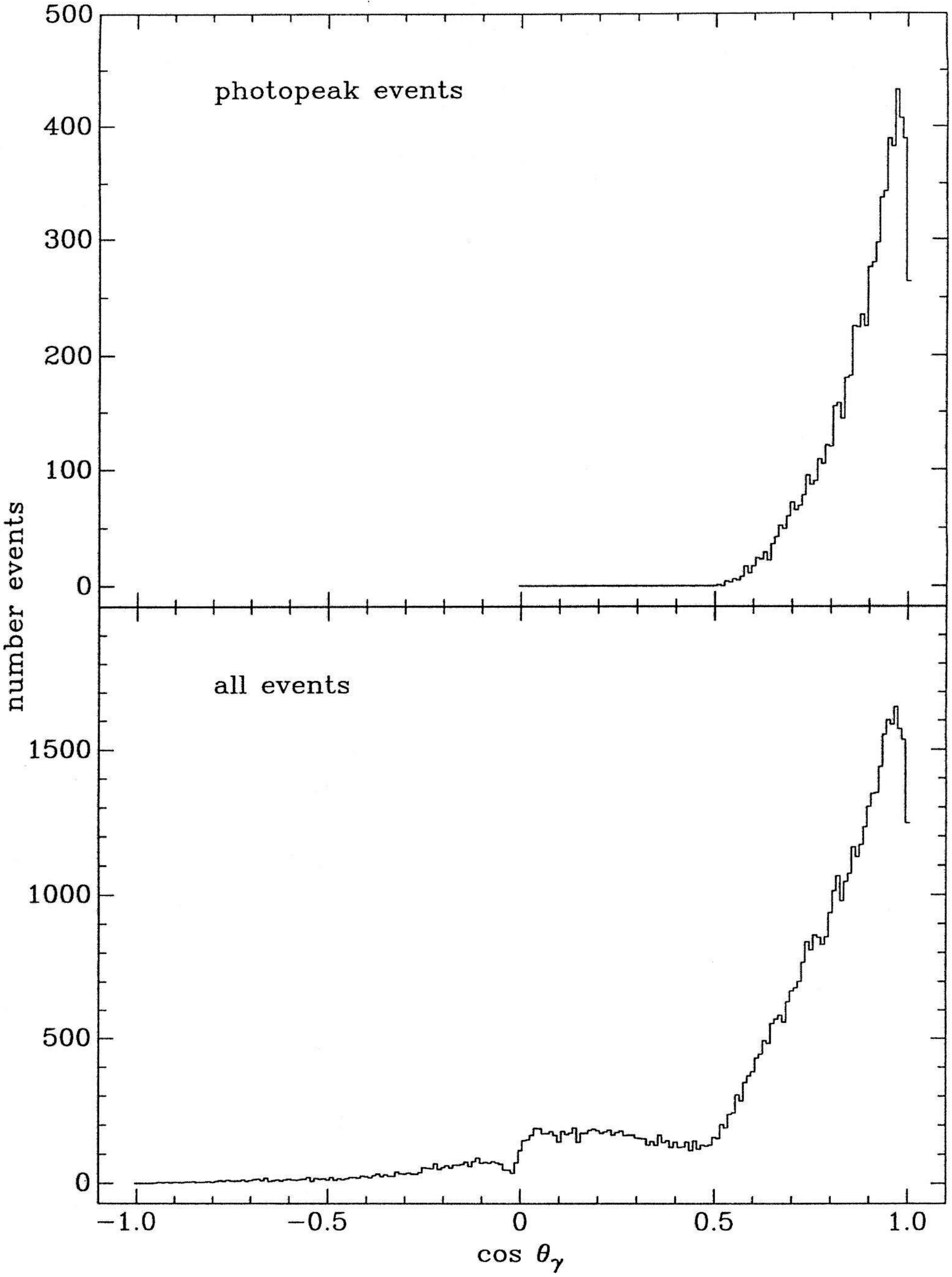

Figure 4.7: The distribution of γ-ray emission angles for detected γ-rays, calculated with EGS4 for a 2750-keV source and geometry A. The upper panel shows the results for full-energy (i.e., photopeak) events, and the lower the results for all events depositing energy in the detector.

and P_ℓ is the Legendre polynomial of order ℓ. We will distinguish between photopeak attenuation factors, Q_ℓ^ϵ, which are calculated from events which deposit the full γ-ray energy, and total attenuation factors, Q_ℓ^η, which are calculated from all detected events. The factors Q_ℓ^ϵ and Q_ℓ^η for $1 \leq \ell \leq 4$, $100 \leq E_\gamma \leq 6000$ keV, and geometries A, B, and C are plotted in Appendix D. The calculations for geometry C were performed using an idealized geometry where the target was normal to the beampipe, as the axially-symmetric geometry was much easier to input to EGS4. The factors calculated for the 0° detector position were assumed to hold for the other positions of geometry C as well.

4.2.3 Detector Efficiency

^{24}Na Source

The ^{24}Na source emits two γ rays (1368 and 2754 keV) per decay in one-to-one coincidence. The cascade consists of a $4^+ \rightarrow 2^+ \rightarrow 0^+$ sequence, where both decays are $E2$ transitions. The γ-ray angular correlation for this sequence is readily found [Fer65] to be

$$W(\theta) = 1 + \frac{5}{49}P_2(\cos\theta) + \frac{4}{441}P_4(\cos\theta). \tag{4.13}$$

The photopeak efficiency at the two γ-ray energies can be found using the number of counts in each photopeak and in the coincident-sum peak. A constraint on the total efficiency can also be found using the total counting rate in the spectrum. The results were analyzed using the relations

$$\begin{aligned}
N_1 &= S\varepsilon_1\{1 - \eta_2[1 + \frac{5}{49}Q_2^\epsilon(1)Q_2^\eta(2) + \frac{4}{441}Q_4^\epsilon(1)Q_4^\eta(2)]\} && (4.14)\\
N_2 &= S\varepsilon_2\{1 - \eta_1[1 + \frac{5}{49}Q_2^\epsilon(2)Q_2^\eta(1) + \frac{4}{441}Q_4^\epsilon(2)Q_4^\eta(1)]\} && (4.15)\\
N_{12} &= S\varepsilon_1\varepsilon_2[1 + \frac{5}{49}Q_2^\epsilon(1)Q_2^\epsilon(2) + \frac{4}{441}Q_4^\epsilon(1)Q_4^\epsilon(2)] && (4.16)\\
N_{tot} &= S\{\eta_1 + \eta_2 - \eta_1\eta_2[1 + \frac{5}{49}Q_2^\eta(1)Q_2^\eta(2) + \frac{4}{441}Q_4^\eta(1)Q_4^\eta(2)]\}, && (4.17)
\end{aligned}$$

where N_1 and N_2 are the number of counts in 1368- and 2754-keV photopeaks, N_{12} is the number counts in the coincident-sum peak, and N_{tot} is the total number of counts in the spectrum (corrected for the experimental effects of dead time, pileup, background, and extrapolation to zero pulse height). The quantity S is the number of source decays in the counting interval, ε_i and η_i are the photopeak and total efficiencies for energy i, and $Q_\ell^\varepsilon(i)$ and $Q_\ell^\eta(i)$ are the attenuation coefficients for energy i, from Subsection 4.2.2. These equations include all coincident summing effects.

Equations 4.14–4.17 were iteratively solved for ε_1, ε_2, S, and η_2, using $\eta_i = 0$ for the first pass. Then η_1 was calculated from ε_1 and ϕ_1 (ϕ_1 is assumed known from other sources); η_2 was found using Equation 4.17. This process was continued until it converged to the solution; the convergence is quite rapid, because η_i is small compared to unity: $\eta_i \sim 0.15$ for geometry A, and is an order of magnitude smaller for geometries B and C. For geometry C, the photofraction was assumed to be known at both energies, so ε_1, ε_2 and S were calculated without using Equation 4.17. The values of S obtained from different measurements of the same source were checked for consistency with the known [End90] 14.958 ± 0.004-h half-life. All of the comparisons were consistent within 1%. The measurements included comparisons of geometries A and B or different angles of geometry C. The before-and-after measurements in geometry C agreed within $\approx$ 1%. The combined error due to statistics and inaccuracies in the photofractions and attenuation coefficients is estimated to be 2%.

The γ rays from the ^{60}Co source used for the photofraction measurements have the identical spin sequence and multipolarities as ^{24}Na. The ^{60}Co data (taken in geometry A only) can thus be analyzed using Equations 4.14–4.17. Using other sources, it was estimated that $\phi(1173\text{ keV}) / \phi(1332\text{ keV}) = 1.09$. The photofractions for ^{60}Co were extracted using this constraint.

^{56}Co Source

The absolute strength of the ^{56}Co source was determined by comparison with the ^{152}Eu source described below, in geometries A and B. The relative γ-ray intensities

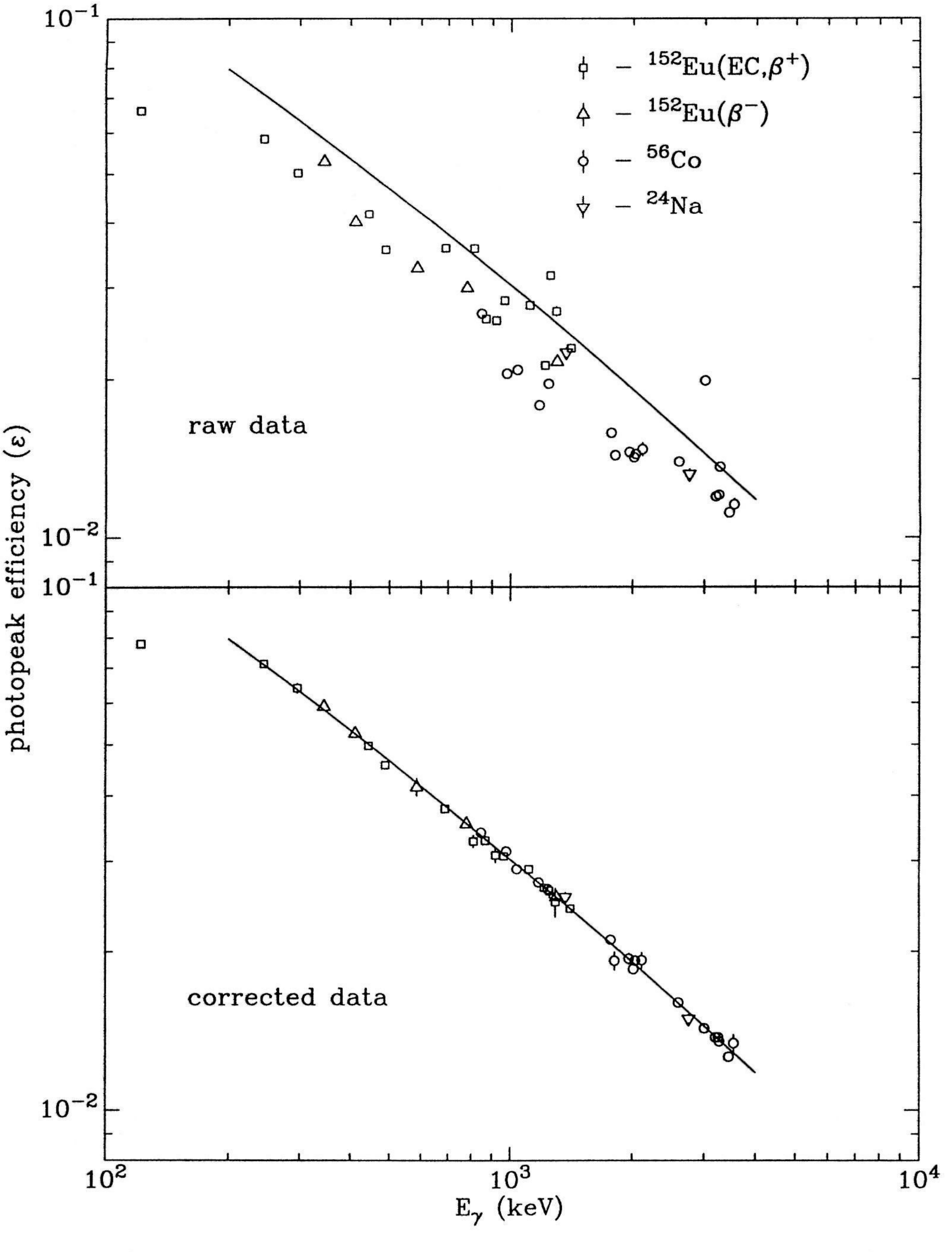

Figure 4.8: The photopeak efficiency for geometry A. The upper panel shows the results without correction for coincident summing, while the lower shows the results including summing corrections. The solid curve on both panels is an empirical fit to the corrected data with $300 \leq E_\gamma \leq 4000$ keV, used in subsequent analysis.

were taken from Yoshizawa *et al.* [Yos80], for $E_\gamma < 2750$ keV. The relative intensities for higher energies were taken from Appendix 4 of *Table of Isotopes* [Led78]. The relative intensities of the stronger lines are known to better than 1%. The remaining details of the decay scheme (β-decay feeding factors, internal-conversion coefficients) needed for making coincidence-summing corrections were taken from *Nuclear Data Sheets* [Jun87].

^{152}Eu Source

The absolute strength of the ^{152}Eu source was previously determined to 1.5% by comparison with NBS source #4275. The relative γ-ray intensities (known to better than 1% for stronger lines) were taken from Trzaska [Trz90] where available; the remaining intensities were taken from Iwata *et al.* [Iwa84]. This source decays by (β^+, EC) to ^{152}Sm and also β^- to ^{152}Gd. The β-decay feeding factors and internal-conversion coefficients were taken from *Nuclear Data Sheets* [Pek89].

^{56}Co and ^{152}Eu Coincident-Summing Corrections

The results from these sources were corrected using the technique of T. M. Semkow *et al.* [Sem90]. Using decay-scheme information, the full coincidence correction from all possible γ-ray combinations is calculated. The effects of "summing out" (loss of photopeak counts due to coincidently detected radiation) and "summing in" (increase in photopeak counts of a crossover γ ray due to coincident photopeak detection of the cascade γ rays) are included. The effects of annihilation radiation from coincident β^+-particles are also included. The angular correlation between γ rays is neglected in this calculation. This assumption is justified on the grounds that in a close geometry, when the coincidence correction is large, the angular correlation is much reduced due to the attenuation coefficients. In a distant geometry, the coincidence correction is small, so an error in the correction due to angular correlation is less significant. The effects of coincident X-rays (from internal conversion or electron capture) and β-particles are not included, and are estimated to be negligible.

The decay-scheme input and the calculations are done in matrix form. The β-decay feeding factor, γ-ray branching factors, and internal-conversion coefficients were supplied for each level. When necessary, the factors were adjusted slightly to reproduce the aforementioned relative γ-ray intensities (which are more accurately known). The ^{152}Eu (EC, β^+) branch was analyzed separately from the β^- branch, since γ rays from one branch are never in true coincidence with γ-rays from the other. The experimental input to the calculation consisted of the number of source decays in the counting interval, the number of counts in a selected set of photopeaks, the $\phi(E_\gamma)$ function, and an estimate for $\varepsilon(E_\gamma)$. The photopeaks selected were those with sufficient statistics and also free from interfering lines. For example, the 1360.2-keV line from ^{56}Co was not used because of interference from the 846.8 + 511-keV coincident-sum peak. The estimate of $\varepsilon(E_\gamma)$ was used in calculating the effects of lines which were not supplied; the estimate was iteratively improved as data from more sources became available. The calculation of the photopeak efficiency for each member of the set is then iterated self-consistently, using $\phi(E_\gamma)$ to estimate η at each step.

The results for geometry A are show in Figure 4.8. The uncorrected efficiency is simply the number of counts in the photopeak, divided by the number of γ rays of that energy emitted. The uncorrected efficiencies show considerable scatter, and are usually lower than the true efficiency. The solid curve is an empirical fit to the corrected data that is used in subsequent data analysis. The corrections for geometries B and C were much smaller ($\approx 3\%$), due to greater source distances.

The corrected efficiencies for each geometry are presented in Appendix E. The solid curves are empirical fits for $300 \leq E_\gamma \leq 4000$ keV. The detection efficiency is assigned a 3% systematic error.

4.3 Target Deterioration

The ^{3}H areal density was observed to deteriorate under α bombardment (see Table 3.1 for before-and-after results). Corrections were made assuming that the ^{3}H areal density after cumulative charge Q (measured in μC) is $(nt)_T F_L(Q)$, where $(nt)_T$ is the initial areal density and

$$F_L(Q) = 1 - \int_0^Q \frac{dQ'\, F_s}{[E_\alpha(Q')]^{0.74}(nt)_{\mathrm{Ti}}}. \tag{4.18}$$

The quantity F_s is a constant, E_α is the incident α energy in keV, and $(nt)_{\mathrm{Ti}}$ is the initial Ti areal density in $10^{17}/\mathrm{cm}^2$. The sputtering rate is expected [Win76] to be proportional to the nuclear stopping power. The nuclear stopping power for α's in Ti [Zie77] is approximately $\propto E_\alpha^{-0.74}$ (over our range of energy), so this dependence is included in Equation 4.18. The constant F_s is 4.0×10^{-6} for targets 1, 3, and 5 (perpendicular target chamber) and 1.8×10^{-5} for target 4 ("45-degree" chamber). These values were found to reproduce the deteriorations observed after the (α, γ) measurements. The error in the correction was assumed to be 40% of the correction, i.e., $\Delta F_L(Q) = 0.4[1 - F_L(Q)]$. From the positions of the centroids and the widths of the γ_0 peaks obtained from target 4, it was determined that the Ti was lost from the target in the same proportion as the ^{3}H.

The ^{3}H areal density was also corrected for radioactive decay using

$$F_d(D) = exp(-\frac{D \log 2}{t_{1/2}}), \tag{4.19}$$

where D is the number of days since the (d, α) areal-density determination, and $t_{1/2}$ is the half-life in days. This correction was never more than 1%.

4.4 Extraction of Cross Sections

The effective reaction energy $\bar{E}$ is found from the observed γ_0 centroid $\bar{E}_{\gamma 0}$ by inverting Equation 4.1 to find E_α, and then calculating $\bar{E}$ from E_α using Equation 4.9. In Equation 4.1, we use $E_\gamma = \bar{E}_{\gamma 0}$ and $\cos\theta_L = Q_1^\epsilon(\bar{E}_{\gamma 0})\cos\theta_D$, where Q_1^ϵ is the photopeak attenuation factor (Subsection 4.2.2) and θ_D is the angle of the center of the detector with respect to the incident beam. In principle, finite detector-size effects should be calculated by expanding Equation 4.1 in terms $\propto P_\ell(\cos\theta_L)$, and then replacing $P_\ell(\cos\theta_L)$ by $Q^\varepsilon_\ell(\bar{E}_{\gamma 0})P_\ell(\cos\theta_D)$. However, our approximation is sufficient since the $\ell > 1$ terms are very small. This analysis also assumes that the radiation is isotropic; the effects of including anisotropy in the $\bar{E}$ extraction were investigated, and found to be negligible for our case. At $E = 50$ keV, the estimated 2% uncertainty in Q^ε_1 contributes ±0.2-keV uncertainty to $\bar{E}$.

The effect of finite detector size on the observed γ_0 energy was tested using the $E_\alpha = 1600$ keV runs on target 5 (numbers 098, 099, and 100), where the detector was in geometry A, geometry B, and geometry A, respectively. The runs were performed in succession, using the the same beam tune for each run. Thus the energy distribution of the γ rays should be identical for the three runs. The centroid was observed to shift by $E_{\gamma 0}(\mathrm{B}) - E_{\gamma 0}(\mathrm{A}) = 5.3(4)$ keV, where the error includes statistics and an estimate of the systematic uncertainty. For $E_\gamma = 3200$ keV, the calculated attenuation factors are $Q^\varepsilon_1(\mathrm{A}) = 0.880$ and $Q^\varepsilon_1(\mathrm{B}) = 0.987$. Using $E_\alpha = 1600$ keV and $\cos\theta_L = Q^\varepsilon_1$ in Equation 4.1, we calculate $E_{\gamma 0}(\mathrm{B}) - E_{\gamma 0}(\mathrm{A}) = 5.8$ keV, in reasonable agreement with the measured value.

The observed angular distributions $\overline{W}^i_L(\delta)$, which include the effects of finite detector size, are given by Equation 4.8, where $P_\ell(\cos\theta_L)$ is replaced by $Q^\delta_\ell(\bar{E}_{\gamma i})P_\ell(\cos\theta_D)$, and $\delta = \varepsilon$ or η determines whether photopeak or total attenuation factors are to be used. We define ε_i to be the photopeak efficiency evaluated at the observed centroid of γ_i (the energy for γ_1 is calculated from γ_0 and reaction kinematics). The total efficiencies η_i are calculated from ε_i and $\phi(E_{\gamma i})$. The effective efficiencies $\tilde{\varepsilon}_i$, which include coincident-summing corrections, are defined by

$$\tilde{\varepsilon}_0 = \varepsilon_0 + 0.44\varepsilon_1\varepsilon_2\frac{\overline{W}^1_L(\varepsilon)\overline{W}^1_L(\varepsilon)}{\overline{W}^0_L(\varepsilon)}, \tag{4.20}$$

$$\tilde{\varepsilon}_1 = \varepsilon_1[1 - \eta_2\overline{W}^2_L(\eta)], \tag{4.21}$$

and

$$\tilde{\varepsilon}_2 = \varepsilon_2[1 - \eta_1\overline{W}^1_L(\eta)]. \tag{4.22}$$

RUN	E_α (keV)	f
063	400	0.998
070	200	0.979
074	500	0.998
075	300	0.992
077	150	0.944
079	250	0.984
089	500	0.998
092	280	0.991
096	140	0.992
145	290	0.993
146	290	0.994
147	290	0.995
148	290	0.996
149	290	0.996

Table 4.1: The correction factors f. All of the runs with $|1-f| \geq 0.001$ are shown. The run numbers, incident energy, and correction factors are given.

The term added to ε_0 includes the effect of coincident photopeak detection of γ_1 and γ_2; the factor 0.44 is branching ratio, σ_1/σ_0 (Chapter 5). The terms subtracted from ε_1 and ε_2 correct for the lost counts due to the coincident detection of the other cascade member.

The number of counts in γ-ray peak i per incident α, Y_i, is related to the experimental cross section at $\bar{E}$, $\sigma_i(\bar{E})$, by

$$Y_i = f\ (nt)_T\ F_L(\overline{Q})\ F_d\ \sigma_i(\bar{E})\ \tilde{\varepsilon}_i\ \overline{W}^i_L(\varepsilon), \tag{4.23}$$

where f is a deconvolution factor defined below, and $\overline{Q}$ is the cumulative charge up to the half-way point in the run (as determined by charge).

If the cross section is known and the target consists of a homogeneous Ti–^{3}H layer, the expected γ_0 yield Y_0^c can be calculated:

$$Y_0^c = (nt)_T \; F_L(\overline{Q}) \; F_d \; \overline{W}_L^i(\varepsilon) \frac{\int_{E_\alpha - \Delta E_\alpha}^{E_\alpha} \sigma_0(E'_\alpha) \; \tilde{\varepsilon}_0[E_{\gamma 0}(E'_\alpha)] \; [\frac{dE_\alpha}{dX}(E'_\alpha)]^{-1} \; dE'_\alpha}{\int_{E_\alpha - \Delta E_\alpha}^{E_\alpha} [\frac{dE_\alpha}{dX}(E'_\alpha)]^{-1} \; dE'_\alpha}, \tag{4.24}$$

where $\frac{dE_\alpha}{dX}$ is the effective stopping power for α's in Ti–^{3}H and ΔE_α is the energy lost in the target. The quantity $E_{\gamma 0}(E'_\alpha)$ is calculated using Equation 4.1 with $\cos\theta_L$ replaced by $Q_1^\varepsilon \cos\theta_D$. The energy of the γ_0 centroid can also be calculated:

$$\bar{E}_{\gamma 0}^c = \frac{\int_{E_\alpha - \Delta E_\alpha}^{E_\alpha} E_{\gamma 0}(E'_\alpha) \; \sigma_0(E'_\alpha) \; \tilde{\varepsilon}_0[E_{\gamma 0}(E'_\alpha)] \; [\frac{dE_\alpha}{dX}(E'_\alpha)]^{-1} \; dE'_\alpha}{\int_{E_\alpha - \Delta E_\alpha}^{E_\alpha} \sigma_0(E'_\alpha) \; \tilde{\varepsilon}_0[E_{\gamma 0}(E'_\alpha)] \; [\frac{dE_\alpha}{dX}(E'_\alpha)]^{-1} \; dE'_\alpha}. \tag{4.25}$$

The calculated γ-ray centroid $\bar{E}_{\gamma 0}^c$ can be converted to an effective reaction energy $\bar{E}^c$ as described in the beginning of this Section. In order for the calculated yield to be consistent with Equation 4.23, the correction factor f must be given by:

$$f = \frac{\int_{E_\alpha - \Delta E_\alpha}^{E_\alpha} \sigma_0(E'_\alpha) \; \tilde{\varepsilon}_0[E_{\gamma 0}(E'_\alpha)] \; [\frac{dE_\alpha}{dX}(E'_\alpha)]^{-1} \; dE'_\alpha}{\sigma(\bar{E}^c) \; \tilde{\varepsilon}_0(\bar{E}_{\gamma 0}^c) \int_{E_\alpha - \Delta E_\alpha}^{E_\alpha} [\frac{dE_\alpha}{dX}(E'_\alpha)]^{-1} \; dE'_\alpha}. \tag{4.26}$$

The energy dependence of σ_0 in Equations 4.25 and 4.26 is assumed to be given by Equation 1.9, with the energy dependence of $S(E)$ from Equation 1.16. The attenuation factors used implicitly in Equations 4.25 and 4.26 are evaluated at the experimental γ_0 centroid $\bar{E}_{\gamma 0}$ in view of the negligible energy dependence of $Q_\ell^\varepsilon(E_\gamma)$. The calculation of f was further simplified by using ε_0 in place of $\tilde{\varepsilon}_0$ in Equations 4.25 and 4.26. This analysis of the correction factor ignores straggling of the beam and the energy dependences of the angular distribution and branching ratio.

The factor f arises because the use of $\bar{E}$ (determined from $\bar{E}_{\gamma 0}$) does not completely deconvolute the effects of the distribution of reaction energies. It is primarily the strong energy dependence of the cross section that makes the correction necessary. The magnitude of f can be estimated in a simple model: (1) ignore the energy dependences of $\tilde{\varepsilon}$ and $\frac{dE_\alpha}{dX}$ in Equations 4.25 and 4.26, (2) expand $\sigma(E_\alpha)$ to first order, i.e., $\sigma(E_\alpha) = \sigma(E_0) + \frac{d\sigma}{dE_\alpha}|_{E_0}(E_\alpha - E_0)$, and (3) simplify Equation 4.1 to be $E_\gamma(E_\alpha) = \frac{M_T}{M_T + M_\alpha} E_\alpha + Q$. The quantity E_0 is defined to be $E_\alpha - \Delta E_\alpha/2$. The factor

f is then analytically calculable using Equations 4.25 and 4.26:

$$f = \frac{1}{1 + \frac{\Delta E_\alpha^2}{12}\left(\frac{1}{\sigma(E_0)}\frac{d\sigma}{dE_\alpha}\Big|_{E_0}\right)^2}. \tag{4.27}$$

It is clear that the factor f will be significantly different from unity when the target is sufficiently thick and/or $\frac{d\sigma}{dE_\alpha}$ is sufficiently large.

For targets 3, 4, and 5, f was calculated using Equations 4.25 and 4.26, with E_α calculated from the NMR-magnetometer calibration. For target 1, the calculation was modified to take into account the energy loss and energy spread due to the nonuniform carbon layer that was deposited. The carbon-layer thickness was adjusted for each run; the values used were found by interpolating between values inferred from the $\bar{E}_{\gamma 0}$ shifts in the repeated $E_\alpha = 1000$-keV runs. The correction factor is only appreciable for the lowest-energy runs, as it arises primarily from the strong energy dependence of the cross section. All of the runs with $|1 - f| > 0.001$ are shown in Table 4.1. The uncertainty in f is taken to be 40%, i.e., $\Delta f = 0.4|1 - f|$.

4.4.1 Angular Distributions

The factors $\overline{W}^i_L(\delta)$ used for summing corrections in Equations 4.20, 4.21, and 4.22 were calculated by taking a_2^0 and a_2^1 from Tombrello and Parker [Tom63], setting $a_1^0 = 0.0$, $a_3^0 = 0.05$, $a_1^1 = 0.08$, $a_3^1 = -0.05$, and setting $a^i_{\ell>3}$ to zero. These choices will be justified by the results presented in Chapter 5. For each γ-ray line, $\sigma_i(\bar{E})\overline{W}^i_L(\varepsilon)$ was extracted using Equation 4.23. This quantity was then converted to $S_i(\bar{E})\overline{W}^i_L(\varepsilon)$ using Equation 1.9. For each nominal energy where angular distributions were taken, the effective reaction energies determined at each angle were then averaged together to give E, the nominal center-of-mass energy.

For each energy the quantities $S_i(E)\overline{W}^i_L(\varepsilon)$ were fit using Equation 4.8, with $P_\ell(\cos\theta_L)$ replaced by $Q_\ell^\varepsilon P_\ell(\cos\theta_D)$. The parameters S_i, a_1^i, a_2^i, and a_3^i were varied; $a^i_{\ell>3}$ were set to zero. The fit was fully determined, since data were available at four independent angles. For each fit the needed Q_ℓ^ε were calculated once at the average

Source of Error	Error (%)	
^{3}H areal density		
^{3}H(d, α) cross section	3	
detector solid angle	1.5	
current integration	2	
statistics	0.8	
uniformity	1	
	4.1	4.1
γ-ray detection efficiency		3
current integration		1
angular-distribution correction		3
total		6

Table 4.2: Systematic errors in the absolute cross section.

γ-ray energy. The neglect of $\ell > 3$ terms in the angular distribution is justified on the grounds that the terms are very small due higher multipolarity and/or initial angular momentum required. The γ_0 and γ_1 angular distributions are plotted in Appendix F (Figures F.1–F.9). The errors in the a_ℓ^i are dominated by statistics; the systematic error due to uncertainties in the detection efficiencies, detector angles, and attenuation coefficients is estimated to be ± 0.03.

The repeated $E_\alpha = 1000$-keV measurements (runs 139 and 150) were used for monitoring target deterioration, but were not analyzed further. The majority of the deterioration of target 4 took place during the $E_\alpha = 290$-keV measurements (runs 145-149). Due to the large uncertainty from target deterioration, these runs were analyzed by normalizing the γ_0 and γ_1 yields to the γ_2 yield. The γ_2 angular distribution was assumed to be isotropic in center of mass. Absolute cross sections were not extracted for these runs.

4.4.2 0° Data

As above, the factors $\overline{W}_L^i(\delta)$ used in Equations 4.20-4.23 were calculated by taking a_2^0 and a_2^1 from Tombrello and Parker [Tom63], setting $a_1^0 = 0.0$, $a_3^0 = 0.05$, $a_1^1 = 0.08$,

$a_3^1 = -0.05$, and setting $a_{\ell>3}^i$ to zero. These choices will be justified by the results presented in Chapter 5. The cross sections $\sigma_i(E)$ were then extracted using Equation 4.24, and converted to $S_i(E)$ using Equation 1.9.

4.4.3 All Data

Since S_1 must equal S_2, the weighted average of S_1 and S_2 (using statistical errors) was taken to form S_{12}. Then S_0 and S_{12} were added together to give S, the total S-factor. The error explicitly included with S results from errors due to statistics, ΔF_L, Δf, and uncertainty in the center-of-mass energy (from the Q-value, γ-ray energy calibration, statistical error in centroid, and attenuation coefficients), combined in quadrature. Additional systematic uncertainties are listed in Table 4.2.

The branching ratio R is calculated by dividing the weighted average of γ_1 and γ_2 by γ_0: $R = S_{12}/S_0$. The error explicitly included with R is statistical; the systematic error in R is estimated to be 4%.

Chapter 5

Results

5.1 Total S-factor

The total S-factors obtained with the different targets and in different geometries are shown in Figure 5.1 and tabulated in Tables F.1 and F.2 of Appendix F. The data taken under different experimental conditions are seen to be in excellent agreement. It is also seen that the energy dependence of the data is well described by Equation 1.16. We adopt this energy dependence as a means of comparing and combining the different data sets. The results for fits to Equation 1.16 are shown in Table 5.1. The data sets were combined by first slightly renormalizing each set so that the fitted $S(0) = 0.1067$ keV-b, and then taking the weighted average of S and E for data points whose energies were within $\lesssim$ 10 keV. The weighted averages for σ_1/σ_2 and R (presented below) were also formed using statistical errors and the same energy binning used for S. The systematic uncertainty in S due to the Q-value was not included in making the weighted average, but was included after doing so. The final results for σ and S are shown in Figures 5.2 and 5.3; the numerical values for S are listed in Table F.4 of Appendix F. The error bars do not include an additional systematic error of 6% (Table 4.2); of the total systematic error, the energy-dependent contributions due to γ-ray efficiency and angular-distribution corrections are estimated to be $\lesssim 4\%$.

Data Set	N	$S(0)$ (keV-b)	χ^2
target 1, geo A	19	0.1060(6)	23.0
target 1, geo B	2	0.1067(18)	0.008
target 3, geo A	8	0.1074(9)	7.96
target 3, geo B	2	0.1049(21)	2.44
target 4, geo C	9	0.1053(8)	5.33
target 5, geo A	8	0.1109(12)	4.17
target 5, geo B	1	0.1116(33)	0.0
all data	49	0.1067(4)	64.3

Table 5.1: The resulting $S(0)$ values found from fits of Equation 1.16 to data taken under different experimental conditions. Also given are the number of data points N and the χ^2 for each fit. The numbers in parentheses are the statistical errors in the least significant digits.

5.2 Branching Ratio

As a test of internal consistency, the ratio $Z = \sigma_1/\sigma_2$ is shown in Figure 5.4; $Z = 1$ is required since the cascade through the first excited state is one-to-one. The results are seen to be consistent with $Z = 1$, although the dispersion is greater than the statistical errors: $\chi^2 = \sum_i [(Z_i - 1)/\Delta Z_i]^2 = 31$ for 17 data points. An additional error of 4% (in quadrature) is required to make $\chi^2 = 17$; this error is within the estimated systematic error in detection efficiency and angular-distribution corrections. It should be noted that the statistical error in γ_1 is about twice that of γ_2, so the weighted average used in calculating R strongly favors γ_2 compared to γ_1.

The results for the branching ratio R are shown in Figure 5.5, and are consistent with a constant; a fit of the 17 data points to a constant using statistical errors yields $R = 0.453(2)$, with $\chi^2 = 40.1$. A fit to a linear dependence yields an improved fit: $R(0) = 0.437(5)$, $dR/dE = 3.4(9) \times 10^{-5}$ keV^{-1}, with $\chi^2 = 27.1$, but this energy dependence is within the estimated 4% systematic error. The results for R are tabulated in Table F.4 of Appendix F.

Coefficient	Function	Result	χ^2	Adopted
a_1^0	constant	0.007(10)	8.9	0.0
a_2^0	[Tom63]	–	9.3	[Tom63]
a_3^0	constant	0.05(2)	8.2	0.05
a_1^1	constant	0.08(2)	13.2	0.08
a_2^1	[Tom63]	–	13.6	[Tom63]
a_3^1	constant	–0.05(5)	12.9	–0.05

Table 5.2: Fits of the γ_0 and γ_1 Legendre coefficients (9 data points for each coefficient) to either a constant or the Tombrello-Parker [Tom63] calculation. In the case of the Tombrello-Parker calculation, there are no variable parameters. The parameterization used in the analysis of the zero-degree data is listed in the column under Adopted. The numbers in parentheses are the statistical errors in the least significant digits.

5.3 Angular Distributions

The measured Legendre coefficients for the γ_0 and γ_1 transitions are shown in Figures 5.6 and 5.7, and are tabulated in Table F.3 of Appendix F. The results for γ_1 are similar to γ_0, except that the errors are significantly larger due to poorer statistics. The results for a_2^i are seen to be in reasonable agreement with the calculation of Tombrello and Parker [Tom63]. Comparisons of the a_2^i coefficients to the Tombrello-Parker calculation as well as fits to a constant for a_1^i and a_3^i are described in Table 5.2. The Tombrello-Parker calculation and the values obtained from fits to a constant for the odd terms have been adopted for the analysis of the zero-degree data. The constant fits were chosen for simplicity; the Legendre coefficients are expected to be slowly varying functions of energy, but the limited statistics mask any energy dependence. The values adopted have little impact on the final results: setting $a_1^i = a_3^i = 0$ changes the extracted values of S and R by $\approx 1 - 2\%$.

The measured coefficients for γ_2 are shown in Figure 5.8, and are consistent with the required isotropic distribution. The systematic error in the a_ℓ^i coefficients is estimated to be ± 0.03. The fits to the γ_0 and γ_1 angular distributions and the Legendre coefficients extracted are given in Appendix F.

5.4 Comparison with Previous Experiments

5.4.1 Total S-factor

The present results for S are compared to the previous direct measurements in Figure 5.9. Our results are seen to be consistent with all previous data for $E \gtrsim 200$ keV, if systematic errors are taken into consideration. However, for $E \lesssim 150$ keV, the present data are $\approx 40\%$ lower than the data of Schröder *et al.* [Sch87] (the only previous experiment in this range). For $E \gtrsim 250$ keV, our results for S are consistent with the Coulomb-breakup results of Utsunomiya *et al.* [Uts90] (Figure 1.6), but are considerably lower at lower energies. The agreement with the Coulomb-breakup data at higher energies is not surprising since their results are normalized to $S(500 \text{ keV}) = 0.060$ keV-b. The 6% systematic error in the present experiment is considerably smaller than the $14-25\%$ systematic error in the previous experiments.

5.4.2 Branching Ratio

The present results for R are compared to previous data in Figure 5.9. The results are consistent with the data of Griffiths *et al.* [Gri61] and Burzynski *et al.* [Bur87], but are about 40% higher than those of Schröder *et al.* The statistical and systematic errors are considerably reduced compared to the previous experiments.

5.4.3 Angular Distributions

The only previous data on the angular distributions come from the limited measurements of Griffiths *et al.* They found that the angular distributions of γ_0 and γ_1 were identical within 5%; the present data (Figures 5.6 and 5.7) and the calculation of a_2^i by Tombrello and Parker are consistent with this result. The present data are in agreement with the measured γ_0 angular distributions of Griffiths *et al.*, as shown in Table 5.3.

Intensity Ratio	Griffiths *et al.* [Gri61]		Present Experiment		Calculation
	E (keV)	Result	E (keV)	Result	
0°/90°	241	1.05(6)	245	1.17(5)	1.18
0°/90°	567	1.28(4)	560	1.33(5)	1.36
45°/90°	567	1.06(6)	560	1.10(4)	1.14
135°/90°	567	1.02(6)	560	1.12(4)	1.16

Table 5.3: The previous γ_0 angular-distribution measurements of Griffiths *et al.* are compared to present measurements taken at nearly identical energies. The ratios calculated with the angular distributions used for the analysis of the 0° data are also given ($a_\ell^0 = 0$, except a_2^0 is taken from the Tombrello-Parker calculation [Tom63], and $a_3^0 = 0.05$). All of the results are in the center-of-mass system, except for the 241-keV result of Griffiths *et al.*, where it is not clear if corrections for finite detector size and center-of-mass motion have been made. The numbers in parentheses for both experiments are the statistical errors in the least significant digit.

5.5 Comparison with Theoretical Calculations

5.5.1 Total S-factor

The present data are compared to several theoretical energy dependences in Figure 5.10 and Table 5.4. The S-factor rises at low energies, consistent with the theoretical calculations. The data are consistent with all of the energy dependences, except perhaps that of Mertelmeier and Hofmann [Mer86]. The absolute magnitude of the S-factor is consistent with the rather large range allowed by theoretical calculations described in Subsection 1.2.2.

5.5.2 Branching Ratio

The branching ratios found in the present experiment are consistent with all calculations [Kaj86, Alt88, Kaj89, Moh93], which predict R in the range $0.41 - 0.47$. The strong theoretical objections [Alt88, Kaj89] to the branching ratio found by Schröder *et al.* have proven to be well founded.

Data Range	Reference	$S(0)$ (keV-b)	$S(500\text{ keV})$ (keV-b)	N	χ^2
all data	[Kaj87]	0.1067(4)	0.0604(2)	17	18.2
$100 < E < 1000$ keV	[Lan86]	–	0.0613(2)	12	12.4
$E > 100$ keV	[Mer86]	–	0.0603(2)	14	82.9
$50 < E < 600$ keV	[Alt88] MHN	–	0.0609(3)	13	20.3
$E < 1000$ keV	[Moh93]	0.9744(4)	0.0608(2)	15	47.4

Table 5.4: Fits of our data to various theoretical calculations of $S(E)$. We have used the Modified Hasegawa-Nagata (MHN) interaction calculation from Altmeyer *et al.* [Alt88]. Some of the calculations do not cover the full range of the data, so the range of data and number of points N are given. The normalization at $E = 500$ keV, χ^2, and when possible $S(0)$ are also given; the numbers in parentheses are the statistical uncertainties in the least significant digits. The fits are plotted in Figure 5.10.

5.5.3 Angular Distributions

As discussed in Section 5.3, the measured a_2^i coefficients are consistent with the calculations of Tombrello and Parker. There are no theoretical calculations of the a_1^i and a_3^i coefficients, but the results are consistent with the expectation that a_1^i and a_3^i would be less significant than a_2^i, due to relative weakness of the interfering $M1$ or $E2$ amplitudes. In the case of the mirror $^3\text{He}(\alpha,\gamma)^7\text{Be}$ reaction, Tombrello and Parker calculated $|a_1^i|$ and $|a_3^i|$ to be less than 0.1.

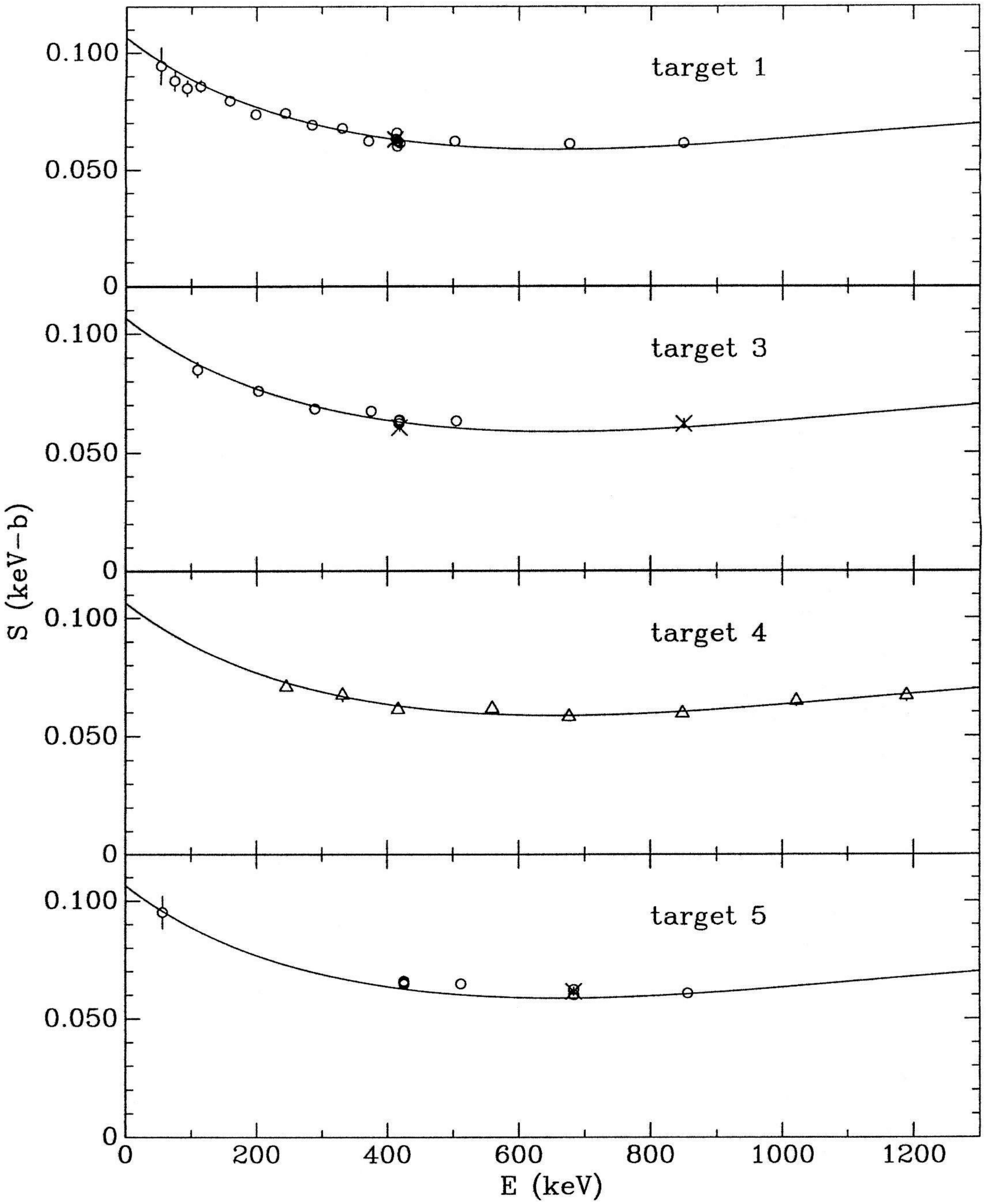

Figure 5.1: Total S-factors obtained from targets 1, 3-5. The circles, crosses and triangles correspond to data taken in geometries A, B, and C, respectively. The solid curves are Equation 1.16, normalized to $S(0) = 0.1067$ keV-b.

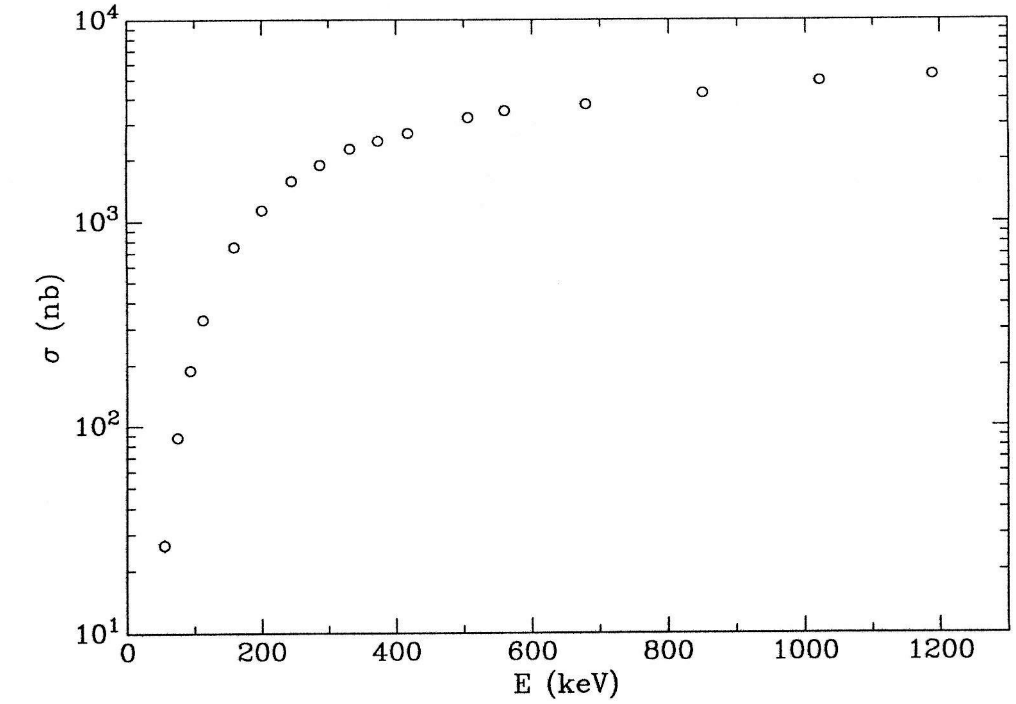

Figure 5.2: The final result for σ, found by combining data sets shown in Figure 5.1.

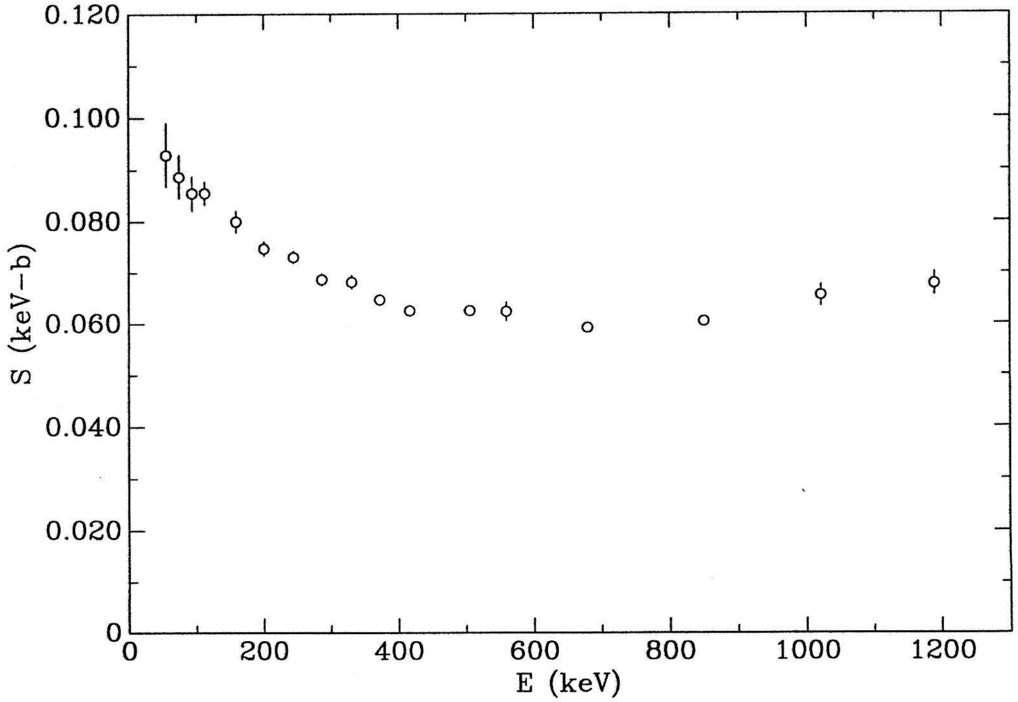

Figure 5.3: The final result for S, found by combining data sets shown in Figure 5.1. The error bars do not include the additional systematic error of 6%.

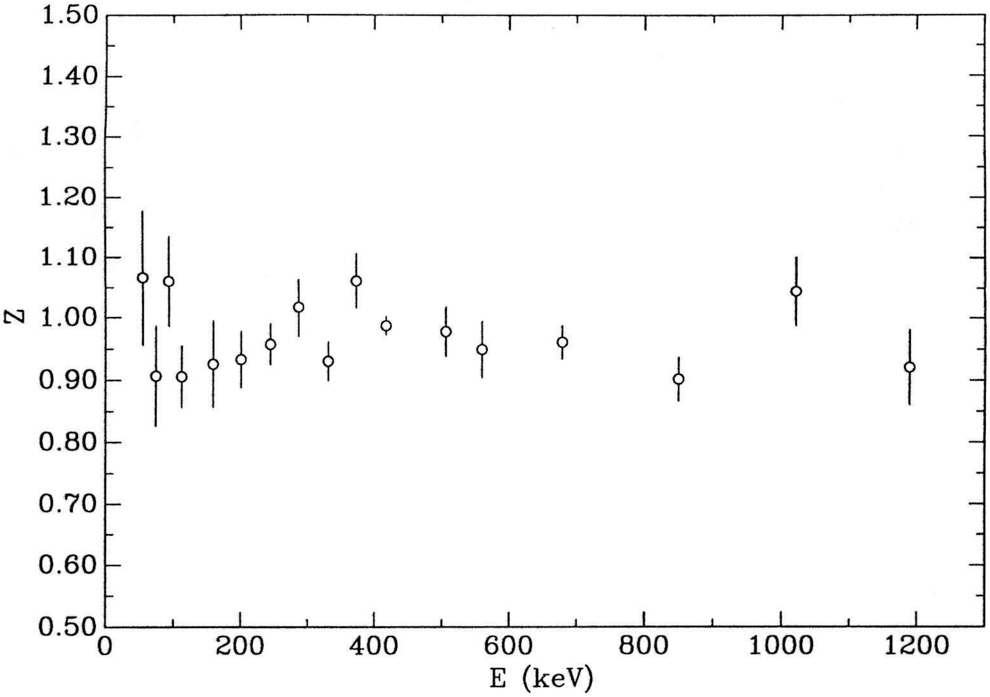

Figure 5.4: The ratio $Z = \sigma_1/\sigma_2$; the error bars include only statistical uncertainties. Note the suppressed zero.

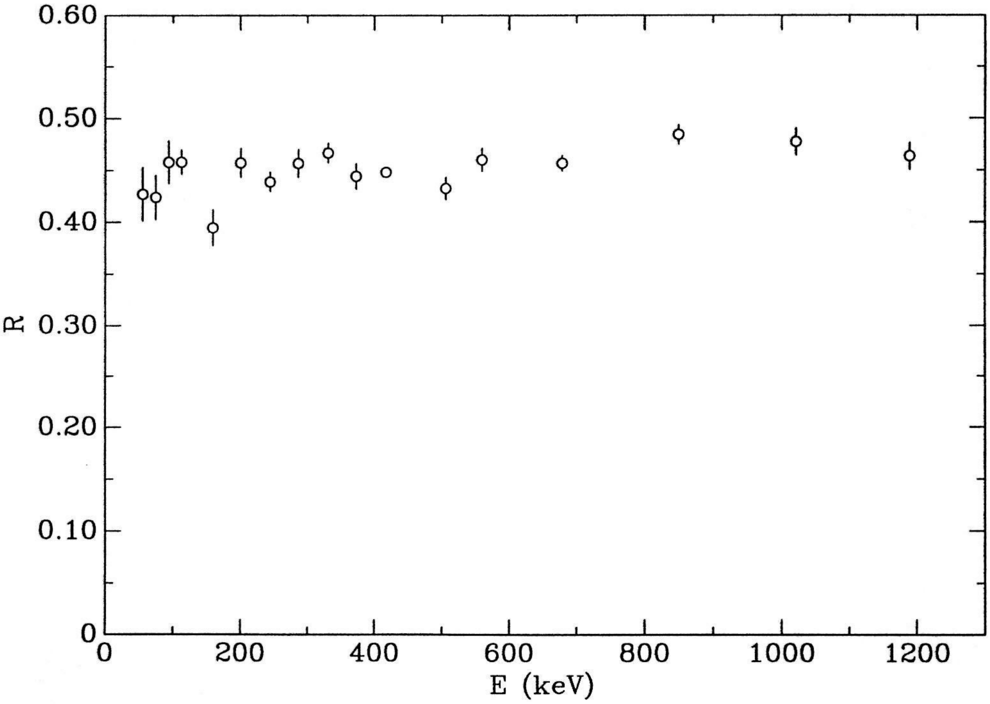

Figure 5.5: The branching ratio R. The error bars are statistical; the systematic error is estimated to be 4%.

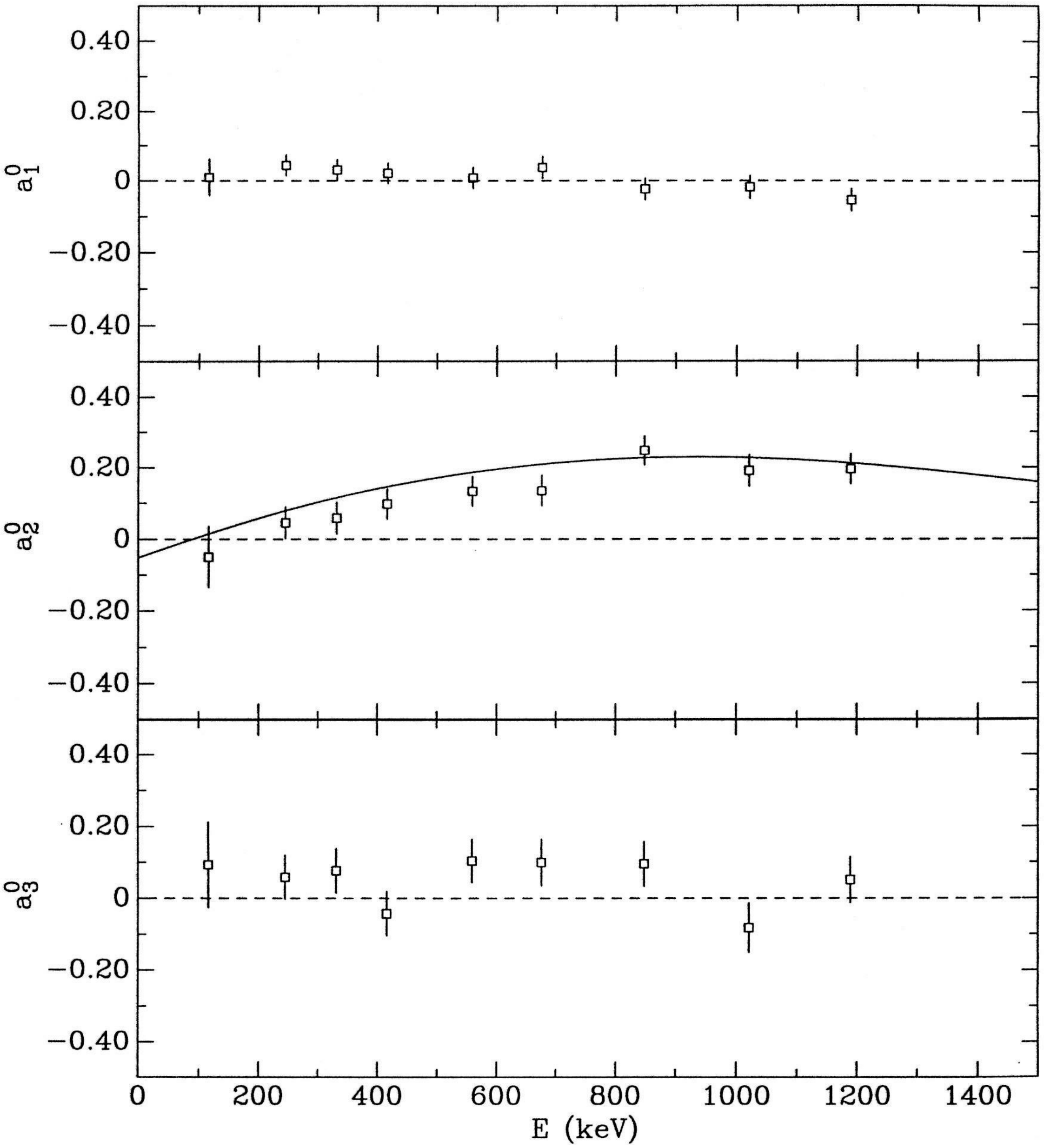

Figure 5.6: γ_0 angular-distribution coefficients. The errors are statistical; the systematic uncertainty in a_ℓ^0 is estimated to be ±0.03. The solid curve is the calculation of Tombrello and Parker [Tom63] for a_2^0.

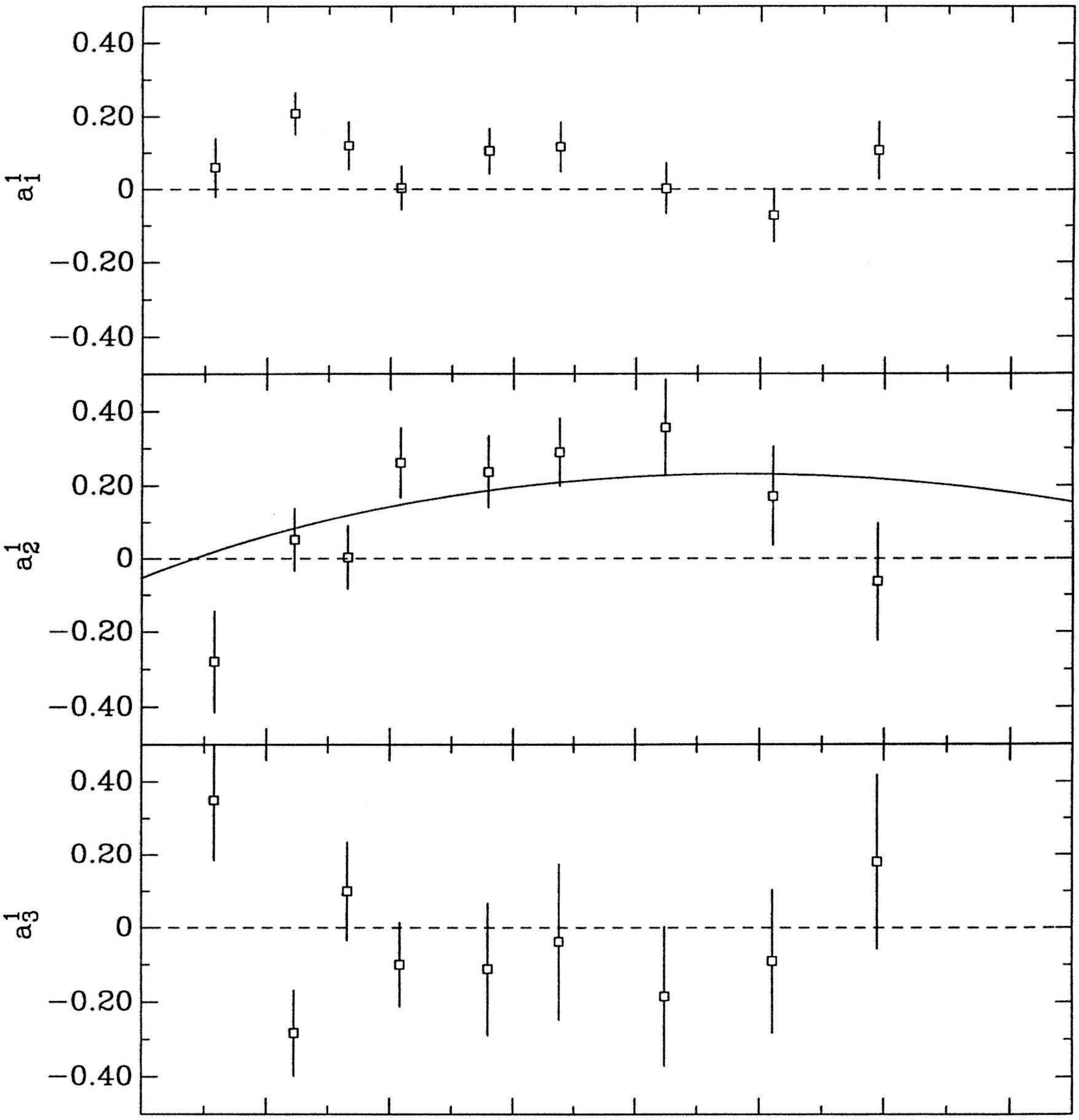

Figure 5.7: γ_1 angular-distribution coefficients. The errors are statistical; the systematic uncertainty in a_ℓ^1 is estimated to be ±0.03. The solid curve is the calculation of Tombrello and Parker [Tom63] for a_2^1.

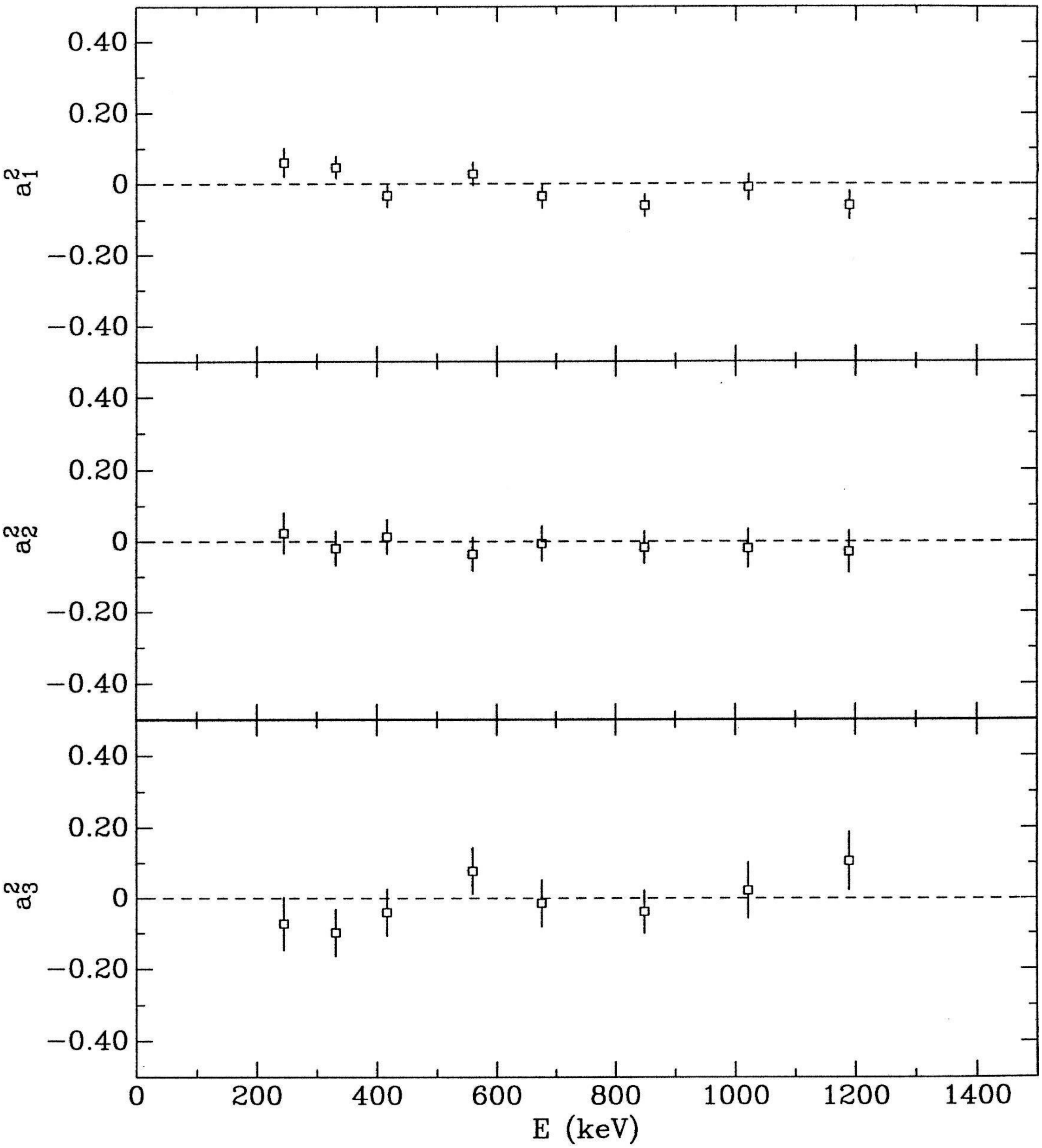

Figure 5.8: γ_2 angular-distribution coefficients. The errors are statistical; the systematic uncertainty in a^2_ℓ is estimated to be ±0.03.

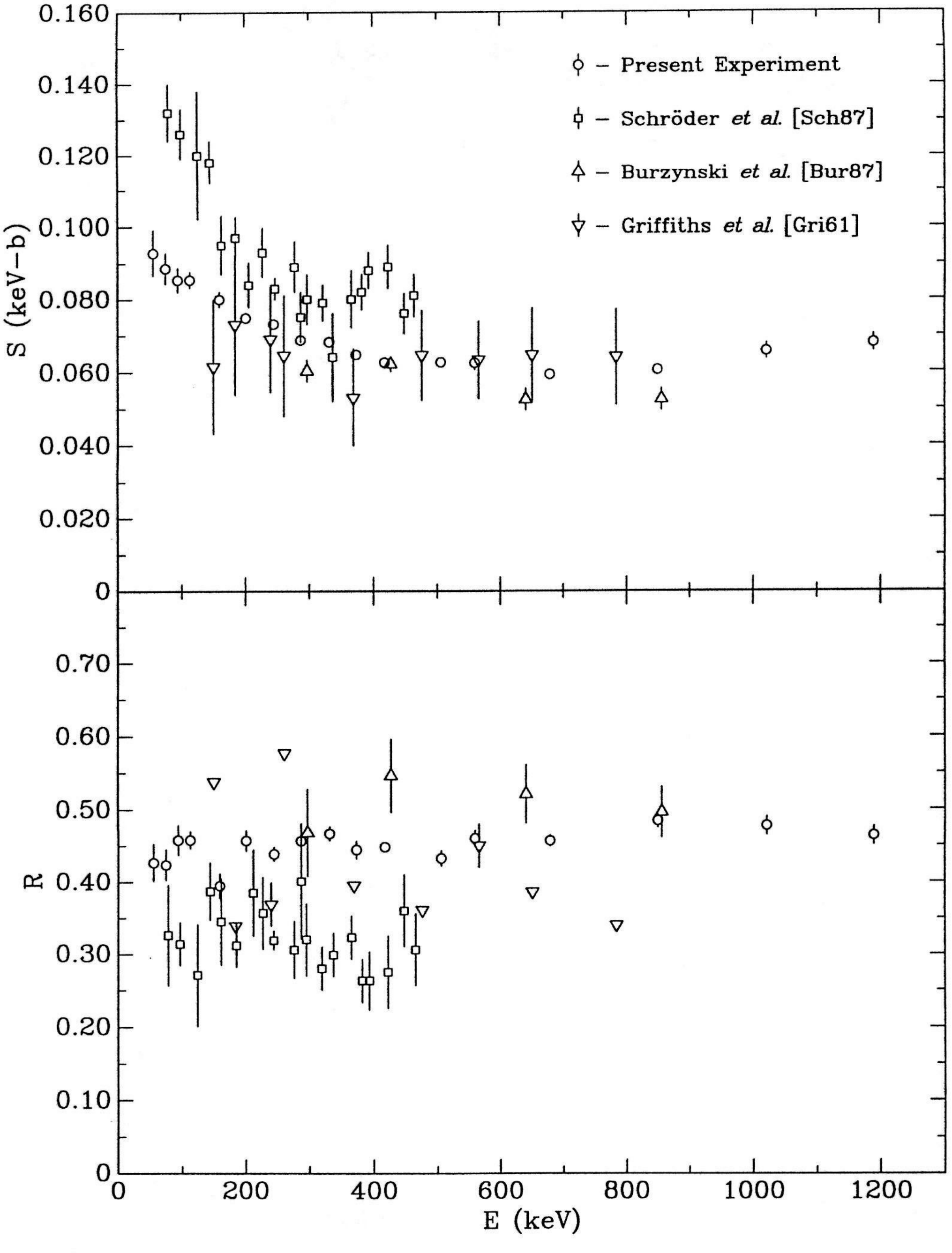

Figure 5.9: The present results for S and R, compared to previous direct measurements.

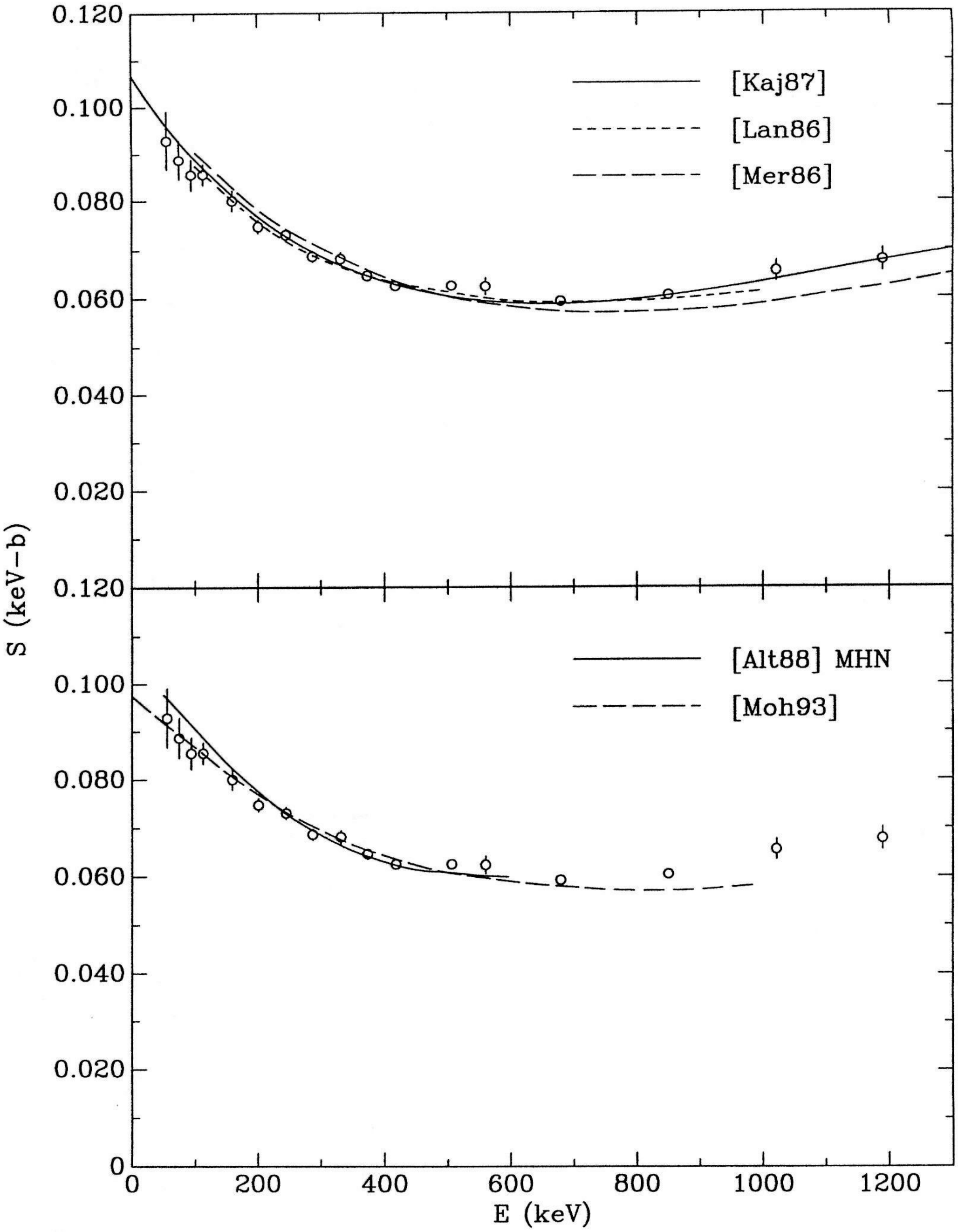

Figure 5.10: Fits to theoretical calculations of $S(E)$. The details of the fits are shown in Table 5.4.

Chapter 6

Conclusions

6.1 Nuclear Physics

We have measured the $^3\mathrm{H}(\alpha,\gamma)^7\mathrm{Li}$ cross section for $50 \leq E \leq 1200$ keV, with a systematic uncertainty estimated to be 6%. Nine angular distributions were measured between 115 and 1200 keV. The present results disagree at low energies ($E \lesssim 200$ keV) with two previous experiments [Sch87, Uts90], which show a larger increase in the low-energy S-factor than predicted by theoretical calculations of the energy dependence. Our measurements of the branching ratio (we find $R \approx 0.45$) are in reasonable agreement with Griffiths *et al.* [Gri61] and Burzynski *et al.* [Bur87], but not with Schröder *et al.* [Sch87] (who found $R \approx 0.32$). The systematic error in the present experiment is reduced by a factor of 2–4 compared to the previous measurements, leading to a much better determination of the absolute normalization of the cross section. As discussed in Section 5.5, the energy dependence of the cross section, the magnitude of the branching ratio, and the angular distributions are in reasonable agreement with the available calculations.

The serious disagreement between our results and those of Schröder *et al.* for the low-energy behavior of the S-factor and also the absolute magnitude of the branching ratio prompted an investigation into possible explanations for the discrepancies.

The discrepancy in energy dependence at low energies is probably due in part to the neglect of the effects of finite detector size on the calculation of the effective reaction energy from the observed mean γ_0 energy. Schröder *et al.* apparently assumed $\cos\theta_L = 1$ in their analysis of their 0° data (see Section 4.4 for the analysis used in the present experiment). For their geometry (104-cm^3 detector, front face $\approx$ 1.0 cm from target), we estimate $Q_1^\varepsilon = 0.83$. Using this estimate for $\cos\theta_L$ in Equation 4.1, the extracted value of $\bar{E}$ is increased by 2.2 keV, for $E = 79$ keV (the lowest energy measured by Schröder *et al.*). This change in energy will reduce the extracted value of S by about 10%. For $E = 200$ keV, the extracted values of $\bar{E}$ would be increased by 3.9 keV, but this reduces the value of S by only about 4%, due to the decreased slope of the cross section (see Equation 1.13). The inclusion of this effect would clearly improve the agreement of the Schröder *et al.* data with the present experiment. This example shows the importance of understanding the energy scale at low energies, where the cross section is highly energy-dependent.

The discrepancy in the branching ratio probably results in part from the neglect of coincident-summing corrections by Schröder *et al.* For their geometry, these effects would decrease the apparent γ_1 and γ_2 fluxes by $\approx$ 15%, and increase the γ_0 flux by $\approx$ 3% (see Section 4.4 for the analysis used in the present experiment). These corrections would increase branching ratio by $\approx$ 18%, to $R \approx 0.38$, still lower than our result, but in the right direction. The neglect of coincident-summing effects will also affect the determination of the detection efficiency using calibration sources which emit γ rays in coincidence. There exists some indication [Rol91] that there is an error in the relative γ-ray efficiency used by Schröder *et al.*

Major improvements on our experiment seem unlikely, at least within the confines our experimental approach and available detector technology. Continued increases in the efficiency of Ge γ-ray detectors is to be expected. Improvements in the low-energy data using the present techniques would be especially difficult, as the uncertainties from target deterioration and energy-scale determination are at least as important as statistical considerations. A windowless ^{3}H-gas target could be helpful here, but radiation safety would be a serious challenge. A better determination of the ^{7}Li mass excess would eliminate part of the systematic error in determining the effective reaction energy, and would somewhat reduce the errors in our low-energy $S(E)$ data. The angular distributions could be measured more accurately using a fixed array of Ge detectors, thereby greatly increasing the rate at which data is obtainable, and eliminating systematic errors in the normalization of the ^{3}H areal density and number of incident particles for each angle.

While the data are in reasonable agreement with the theoretical calculations of the energy dependence [Kaj86, Lan86, Mer86, Alt88, Moh93], it would be useful if the existing $\sim$ 10% discrepancies (see Figure 5.10) between the calculations could be resolved. However, it may be that this uncertainty represents the best that can be achieved with current theoretical techniques. An improved understanding of the energy dependence would reduce the uncertainty in the cross section at low energies, where the data have larger uncertainties, or are unavailable. However, it is important to note that the present experiment covers nearly all of the energy range needed for standard big-bang nucleosynthesis, so astrophysical conclusions do not depend very much on the extrapolation of data. It would also be interesting to perform another ^{7}Li Coulomb-breakup experiment, under improved kinematical conditions, in order to test the accuracy of radiative-capture cross sections determined in this approach.

6.2 Astrophysics

For the calculation of the thermonuclear reaction rate, we assumed $S(E)$ to be given for $E \leq 1200$ keV by Equation 1.16 normalized to our data, and for higher energies by a linear extrapolation:

$$S(E) = \begin{cases} \text{Equation 1.16, with } S(0) = 0.1067 \text{ keV-b} & E \leq 1200 \text{ keV} \\ 0.0337 + 2.85 \times 10^{-5} E \text{ (keV-b)} & E > 1200 \text{ keV} \end{cases}, \qquad (6.1)$$

where E is in keV. Using this parameterization, the reaction rate $N_A\langle\sigma v\rangle$ was then calculated by numerically integrating Equation 1.8. The results are shown in Figure

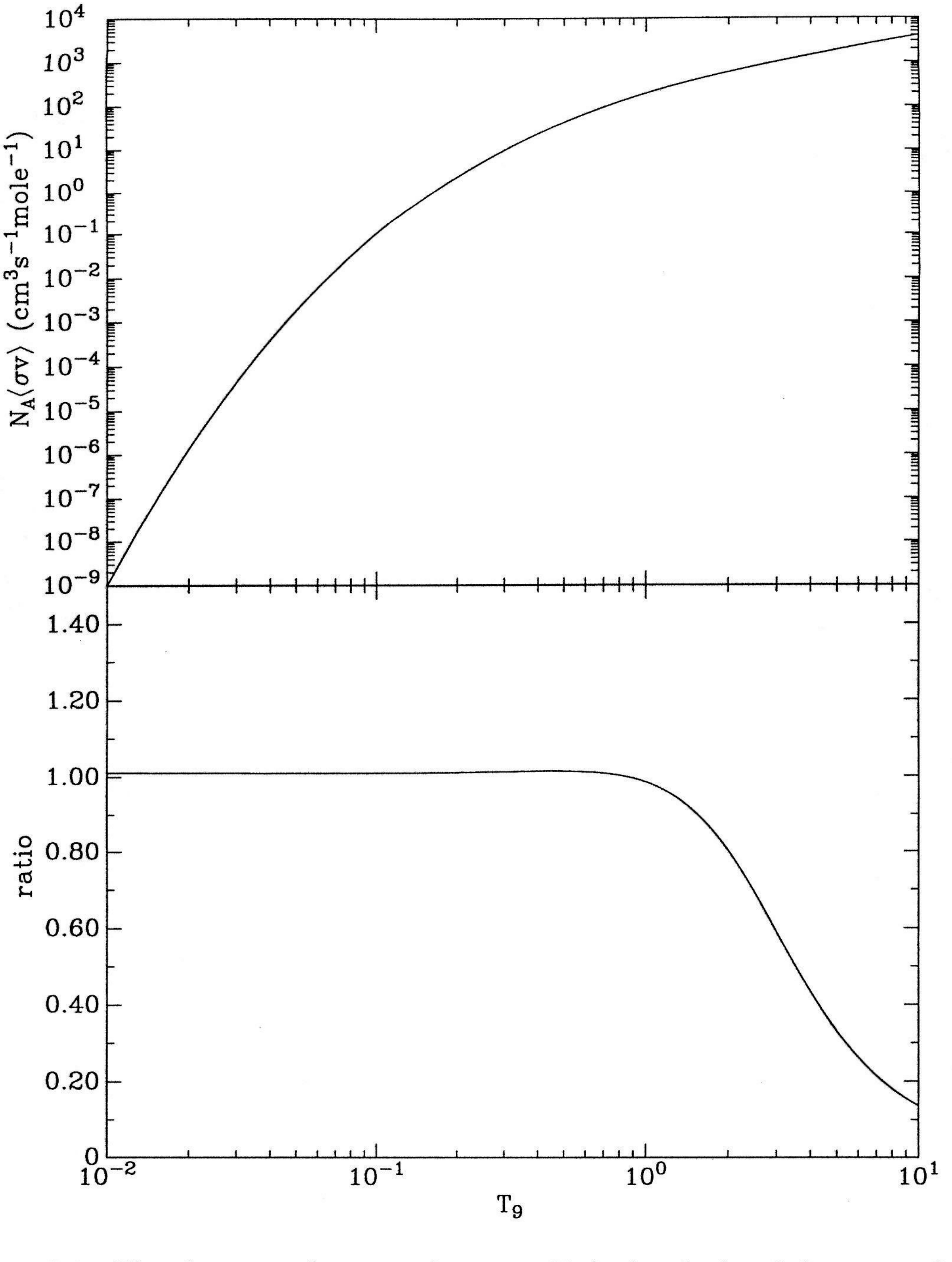

Figure 6.1: The thermonuclear reaction rate $N_A\langle\sigma v\rangle$ calculated from our data is shown as a function of temperature in GK in the upper panel. The ratio of the present reaction rate to that given by Caughlan and Fowler [Cau88] is shown in the lower panel.

6.1. Energies between 50 and 1200 keV (i.e., the range covered by this experiment) contribute at least 50% of the integral in Equation 1.8 for $0.09 \leq T_9 \leq 6$. Also shown in Figure 6.1 is the ratio of the present reaction rate to that given by Caughlan and Fowler [Cau88]. It is seen that the present reaction rate is excellent agreement with the Caughlan-Fowler rate for $T_9 \leq 1$, but is considerably lower for higher temperatures. The excellent agreement at low temperatures is due to Caughlan and Fowler's fortuitous use of Langanke's calculation of $S(E)$ [Lan86], which is in excellent agreement with the present experiment. Our numerically integrated reaction rate is given within $\approx 1\%$ for $T_9 \leq 10$ by the following expression:

$$\begin{aligned} N_A\langle\sigma v\rangle &= 8.79 \times 10^5 T_9^{-2/3} \exp(-\frac{8.080}{T_9^{1/3}}) \\ &\times(1 + 0.0516 T_9^{1/3} - 0.711 T_9^{2/3} + 0.367 T_9 - 0.00581 T_9^2). \end{aligned} \tag{6.2}$$

The S-factor and reaction rate are now determined much more accurately than previously. For $E \leq 1200$ keV, the S-factor is well described by Equation 1.16, with $S(0) = 0.1067$ keV-b. A reasonable estimate for the fractional 1-σ uncertainty in the S-factor is

$$\frac{\Delta S}{S} = 0.06 + 0.06 \exp(-0.005E), \tag{6.3}$$

where E is in keV, the constant term is the estimated systematic error in the present experiment, and the increased error at low energies reflects the increased uncertainty in the low-energy data and also the uncertainty in theoretical extrapolation. The resulting temperature-dependent fractional uncertainty in the reaction rate is approximately given by

$$\frac{\Delta\langle\sigma v\rangle}{\langle\sigma v\rangle} = 0.06 + 0.06 \exp(-1.16 T_9^{2/3}). \tag{6.4}$$

This uncertainty is much smaller than previous estimates; see for example Smith, Kawano, and Malaney [Smi93], who estimated the 1-σ uncertainty to be 29% for $T_9 \to 0$. The uncertainties in Equations 6.3 and 6.4 are only valid for $E \leq 1200$ keV and $T_9 \lesssim 6$, respectively, due to the lack of knowledge of the cross section at higher energies. However, as discussed in the Introduction and Appendix A, big-bang ^{7}Li production is only sensitive to the reaction rate for $0.1 \lesssim T_9 \lesssim 0.6$. Our new reaction rate does not differ significantly from the Caughlan-Fowler compilation in the temperature range needed for standard big-bang nucleosynthesis, so the calculated ^{7}Li abundances described in the Introduction will not change significantly. The error in the ^{3}H$(\alpha,\gamma)^7$Li reaction rate is now comparable to other nuclear-physics uncertainties, reducing a major source of uncertainty in the comparison of big-bang calculations with the observed light-element abundances.

Appendix A

Sensitivity of Standard Big Bang Calculation to the ^{3}H(α,γ)^{7}Li Rate

An analysis of the sensitivity of the standard big bang calculation to the ^{3}H(α,γ)^{7}Li rate is presented in this Appendix. We are particularly interested in finding the temperature range of $N_A\langle\sigma v\rangle$ to which the final calculated ^{7}Li yield is sensitive. The existing literature is not clear on this point: Schröder *et al.* [Sch87] and Utsunomiya *et al.* [Uts90] state that an effective energy of $E_0 \approx 10$ keV (corresponding to $T_9 \approx 0.009$) is most important for ^{3}H(α,γ)^{7}Li in the big bang, while Walker *et al.* [Wal91] use $T_9 = 0.9$ as "a temperature characteristic of nucleosynthesis" for comparison of reaction rates from different sources. It is clearly important to have some idea of what temperatures are important, in order to focus nuclear-physics research on the important energy range.

A.1 Nucleosynthesis

In this section we review some of the fundamentals used in nucleosynthesis calculations. The rate of change of species k, due to the reaction $i + j \rightarrow k + l$, is given by

$$\dot{n}_k = n_i n_j \langle\sigma v\rangle_{ij\rightarrow kl}, \tag{A.1}$$

where n_i is the number density of species i, the dot represents differentiation with respect to time, and $\langle\sigma v\rangle_{ij\to kl}$ is the temperature-dependent reaction rate. It is convenient to factor out the effects of expansion from n_i by defining the number fractions $Y_i = n_i/n_B$, where n_B is the baryon number density; then Equation A.1 becomes

$$\dot{Y}_k = Y_i Y_j [ij \to kl], \tag{A.2}$$

where the rate factor $[ij \to kl]$ is defined by

$$[ij \to kl] = n_B \langle\sigma v\rangle_{ij\to kl}. \tag{A.3}$$

In general the time evolution of a particular species is governed by a sum of terms of the type A.2, including all reactions which produce or destroy the species. These equations, along with the evolution of other quantities such as temperature and n_B, form a complicated network which is normally solved by numerically integrating the equations forward in time (see for example Kawano [Kaw92]).

A.2 Temperature Sensitivity

We investigated the temperature sensitivity of big-bang calculations to the $^3\mathrm{H}(\alpha,\gamma)^7\mathrm{Li}$ rate numerically, i.e., by systematically varying the rate used in the Kawano code. Specifically, the existing reaction rate [Cau88] was multiplied by a temperature-dependent factor

$$f(T,T_0) = \begin{cases} 1 & T \le T_0 - \frac{\Delta}{2} \\ 1 + \epsilon\left[\frac{1}{2} + \frac{3}{2}\frac{T-T_0}{\Delta} - 2\left(\frac{T-T_0}{\Delta}\right)^3\right] & T_0 - \frac{\Delta}{2} < T < T_0 + \frac{\Delta}{2}, \\ 1 + \epsilon & T \ge T_0 + \frac{\Delta}{2} \end{cases} \tag{A.4}$$

where the parameter T_0 is the "perturbing temperature", $\Delta = 0.1T_0$, and $\epsilon = 0.1$. This function is essentially $1 + \epsilon\Theta(T - T_0)$, where $\Theta(x)$ is the step function, except that the step is smoothed out over a width Δ, as shown for $T_0 = 0.5$ GK in Figure

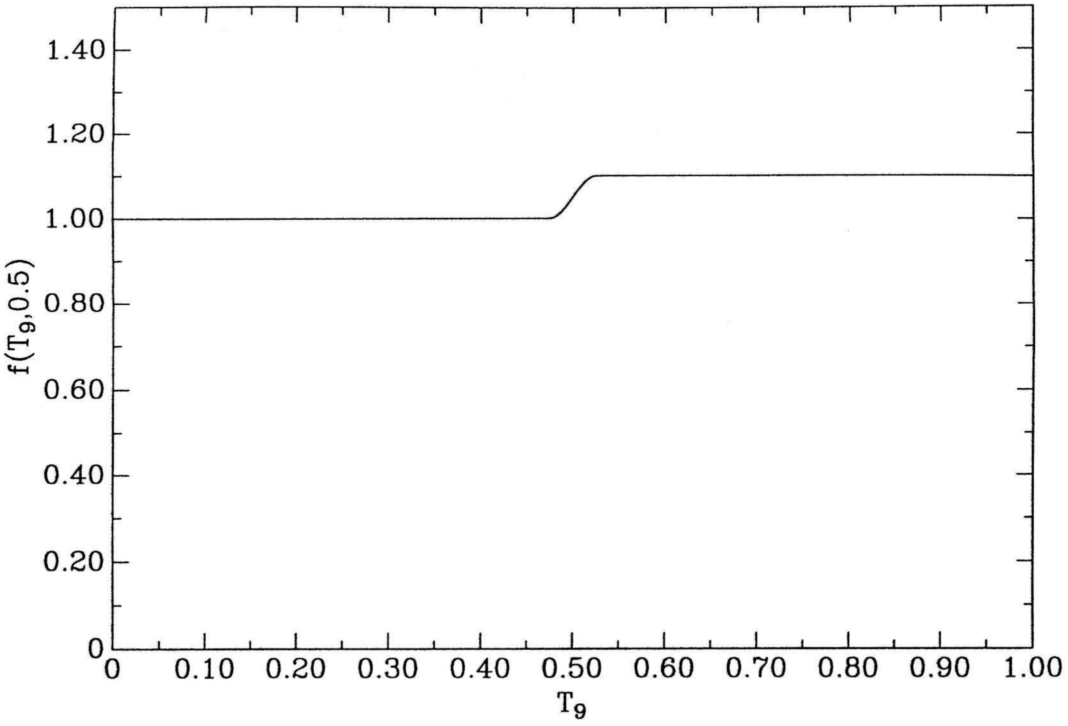

Figure A.1: The perturbing function f (Equation A.4) as a function of temperature in GK, for $T_0 = 0.5$ GK.

A.1. The time step used in the nucleosynthesis calculation was adjusted so that the change in temperature for each step was small compared to Δ.

The ^{7}Li fraction Y_7 (not including ^{7}Be) was calculated as a function of T_0. The resulting fractional change $\delta(T_{90})$ was then calculated using

$$\delta(T_0) = \frac{Y_7(T_0) - Y_7(\infty)}{Y_7(\infty)}. \tag{A.5}$$

Note that the $T_0 \to \infty$ limit corresponds to making no change in the reaction rate, while $T_0 \to 0$ corresponds to multiplying $\langle \sigma v \rangle$ by a constant $1 + \epsilon$. The results for $\eta_{10} = 1.0$, 3.0, and 10.0 are shown in Figure A.2. For $1 \leq \eta_{10} \leq 10$, it is seen that the calculated abundance is sensitive to the position of the step for $0.1 \lesssim T_0 \lesssim 0.6$ GK. Changes in $\langle \sigma v \rangle$ outside of this range do not change the final ^{7}Li abundance. The range of sensitive temperature is also seen to shift to lower temperatures with increasing η. We find that the opposite change in the reaction rate, $\epsilon = -0.1$, has

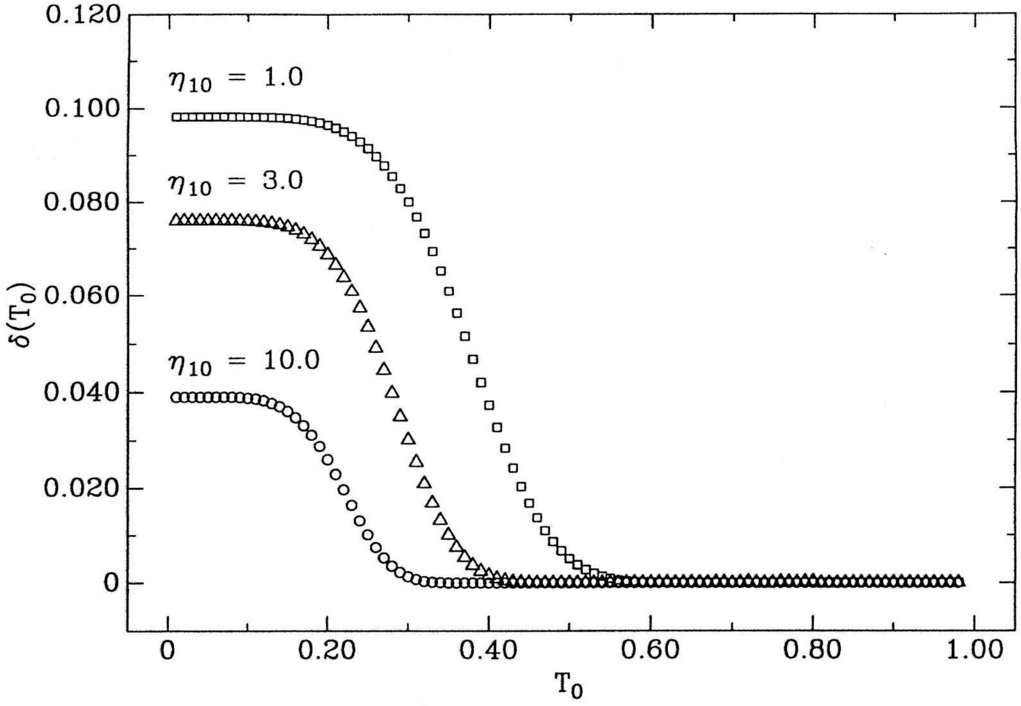

Figure A.2: The fractional change in the calculated ^{7}Li abundance as a function of the perturbing temperature T_0 in GK (see text for details).

the effect of changing the sign of δ.

To summarize, we find that the calculated ^{7}Li abundance is sensitive to the ^{3}H$(\alpha,\gamma)^7$Li reaction rate for $0.1 \lesssim T_9 \lesssim 0.6$. It is not expected that alternative functional forms for variations of the rate would lead to significantly different conclusions. These conclusions could change if any of the assumed reaction rates are seriously in error and are only valid for the standard big bang.

A.3 Freeze-Out Calculation

An alternative approach to calculating big-bang abundances has been given by Esmailzadeh, Starkman, and Dimopoulos [Esm91]. The technique is approximate, but can be done analytically, so the relevant physics is made clear. The authors have succeeded in calculating the big-bang abundances within a factor of three of the exact numerical solution for a wide range of baryon densities.

We will outline their idea, using ^{7}Li as an example, assuming that ^{7}Li is only produced by ^{3}H$(\alpha,\gamma)^7$Li, and destroyed by ^{7}Li(p,α). The evolution of the ^{7}Li fraction Y_7 is then given by

$$\dot{Y}_7 = Y_T Y_\alpha [T\alpha \rightarrow 7\gamma] - Y_p Y_7 [7p \rightarrow \alpha\alpha], \tag{A.6}$$

where Y_T, Y_α, and Y_p are the ^{3}H, ^{4}He, and ^{1}H fractions.[1] Provided that the destruction rate $Y_p[7p \rightarrow \alpha\alpha]$ (i.e., the ^{7}Li reciprocal lifetime) is much greater than the expansion rate of the universe $H(t)$, the ^{7}Li fraction will be given by

$$Y_7 = \frac{Y_T Y_\alpha [T\alpha \rightarrow 7\gamma]}{Y_p [7p \rightarrow \alpha\alpha]}. \tag{A.7}$$

By comparison with Equation A.6 it is clear that this solution corresponds to the case $\dot{Y}_7 \approx 0$, where the production and destruction nearly cancel. The regime where this solution is valid has been dubbed quasi-static equilibrium (QSE). As the universe expands and cools, the reaction rates slow down, and eventually Equation A.7 will no longer be valid. Esmailzadeh, Starkman, and Dimopoulos claim that a reasonable approximation to the final abundance can be found by evaluating Equation A.7 at the "freeze-out" time (or temperature), defined as the time when the expansion rate and the destruction rate are equal, i.e., when

$$H(t) = Y_p [7p \rightarrow \alpha\alpha]. \tag{A.8}$$

Assuming three massless neutrinos, the expansion rate after $e^+ - e^-$ annihilation is given in terms of temperature by

$$H(T_9) = 0.00281 T_9^2 \quad \mathrm{sec}^{-1}. \tag{A.9}$$

---

[1] Y_p here is different from the Y_p used for the primordial ^{4}He mass fraction in Section 1.1.

Using Equation 1.3, the baryon number density is

$$n_B = 2.029 \times 10^{18} T_9^3 \eta_{10} \quad \mathrm{cm}^{-3}. \tag{A.10}$$

Assuming $Y_p = 0.75$, the freeze-out temperature T_{9f} for ^{7}Li is found by solving

$$0.00281 T_{9f}^2 = 0.75 \times 2.029 \times 10^{18} T_{9f}^3 \eta_{10} \langle \sigma v \rangle_{7p \to \alpha\alpha}, \tag{A.11}$$

where $\langle \sigma v \rangle$ is in cm^{3}sec^{-1}. For $\eta_{10} = 1.0$, 3.0, and 10.0, we find T_{9f} to be 0.45, 0.34, and 0.27, respectively. The η dependence comes from the fact that reaction rates are faster (and freeze out at lower temperature) for higher density. The resulting ^{7}Li fraction is estimated using

$$Y_7 \approx \frac{Y_T Y_\alpha}{Y_p} \frac{\langle \sigma v \rangle_{T\alpha \to 7\gamma}}{\langle \sigma v \rangle_{7p \to \alpha\alpha}}, \tag{A.12}$$

where Y_T, Y_α, Y_p, and the reaction rates are evaluated at T_{9f}. For $T_{9f} = 0.34$ ($\eta_{10} = 3.0$) and assuming $Y_T = 4 \times 10^{-7}$ and $Y_\alpha = 0.063$, we find $Y_7 \approx 4 \times 10^{-11}$, in good agreement with the exact value $Y_7^{exact} = 4.8 \times 10^{-11}$. In order to do this calculation from scratch one would of course have to first estimate Y_p, Y_T, and Y_α (the values we have assumed are taken from the exact calculation at $T_9 = 0.34$).

This analysis indicates that the final abundances are dependent on the reaction rates in the vicinity of the freeze-out temperature. The freeze-out temperatures found for ^{7}Li coincide very well with range of sensitive temperatures found in the previous Section (including the dependence of T_{9f} on η). The fact that the final abundance does not depend on the reaction rate at higher temperatures can be understood by considering the QSE solution. As long as ^{7}Li is in QSE, Y_7 only depends on the ^{3}H$(\alpha,\gamma)^7$Li rate at that instant, and not early times (higher temperatures). Thus the final abundance only depends upon the ^{3}H$(\alpha,\gamma)^7$Li rate at times when the QSE condition fails. The lower limit on the sensitive temperature occurs because nuclear reactions cease completely once density and temperature are sufficiently low.

The exact solution of Equation A.6 for the final ^{7}Li fraction is given by [Dim88]

$$Y_7(\infty) = \int_0^\infty Y_T(t) Y_\alpha(t) [T\alpha \to 7\gamma](t) \exp\left\{ - \int_t^\infty Y_p(t') [7p \to \alpha\alpha](t')\, dt' \right\} dt. \quad \text{(A.13)}$$

While this equation is not practical from a computational standpoint, it does provide some insight into the dependence on the reaction rate. Since $Y_7 \ll Y_T$, Y_α, and Y_p at all times, the evolution of Y_7 is decoupled from Y_T, Y_α, and Y_p (i.e., changes in $[T\alpha \to 7\gamma]$ or $[7p \to \alpha\alpha]$ affect Y_7, but have negligible impact on Y_T, Y_α, and Y_p). Thus from Equation A.13 we would expect that multiplying the $^3\text{H}(\alpha,\gamma)^7\text{Li}$ rate by a constant factor would result in the final ^{7}Li abundance being scaled by the same factor. However, in the exact calculation we do not always see a linear relationship: observe the $T_0 \to 0$ limit in Figure A.2 ($\delta = 0.1$ is expected for a linear relationship). While the dependence is linear for $\eta_{10} = 1.0$, a less than linear dependence is seen at higher η. This result occurs because we have ignored the $^7\text{Be}(n,p)^7\text{Li}$ contribution in Equations A.6 and A.13.

Appendix B

Neutron Background

During the ^{3}H(α,γ) measurements at low energies ($E_\alpha \lesssim 400$ keV), an unanticipated neutron background was encountered (see Section 3.1). The ^{3}H(α,n) channel does not open until $E_\alpha \geq 11.13$ MeV. Furthermore, for $E_\alpha \lesssim 400$ keV, it is expected that that α-induced reactions on contaminants in the target would be negligible due to the large coulomb barrier. Initially, we suspected that the neutrons were from ^{3}H(d,n), where the incident deuterons arose from either D_2^+ or DH_2^+ contaminants in the α beam (these molecular ions have the same magnetic rigidity as α^+ ions). Also note that the cross section for this reaction is very large at low energies: $\sigma_{max} \approx 5$ b at $E_d = 110$ keV, so only a $\approx 10^{-7}$ contamination is required to explain the observed neutron yield. We attempted to minimize this problem by using high-purity He gas in the ion source, and by removing the hydrogen (natural abundance) source bottle from the ion source.

In spite of these efforts, the background remained unchanged. A neutron background was also observed in the ^{3}H(α,γ) experiment of Griffiths *et al.* [Gri61]. The authors attributed the neutrons to the ^{3}H$(^3$H$,2n)$ reaction, where the incident ^{3}H particles arose from ^{3}H$(\alpha,^3$H$)$ knock-on reactions. Similar effects have been reported for the proton bombardment of heavy-ice [Jen50, Sin59] and beryllium [Jen50] targets.

After the (α,γ) measurements using target 1, the neutron yield from the target was measured for $150 \leq E_\alpha \leq 1250$ keV, using a 4π neutron detector [Wre94] and the "45-degree" target holder. The purpose of the experiment was to quantify the neutron background, and also to profile the buildup of carbon on the target with the $^{13}C(\alpha, n)$ reaction. The efficiency of the detector was assumed to be the same as for a ^{252}Cf source.

In the calculations that follow, we show that the low-energy neutron yield is explained by the two-step process suggested by Griffiths *et al.* First, we calculated the neutron yield for the azimuthally-symmetric case of the target perpendicular to the α beam. In this case it is a reasonable approximation to ignore energy loss, and an analytic result is obtained. We then calculate the yield for the situation when the target is at an arbitrary angle with respect to the α beam. This case is more complicated (energy losses cannot be ignored), but is the case for which we have experimental data. A somewhat similar calculation has been done by Carraro *et al.* [Car90] as part of an investigation of "cluster-impact fusion."

B.1 Target Normal to Beam, Ignoring Energy Loss

The ingredients for the calculation are the: target-beam geometry, the $\alpha - {}^3$H elastic scattering cross section and kinematics, and σ_T, the $^3H(^3H, 2n)$ cross section. The geometry is displayed in Figure B.1. For sufficiently thin ^{3}H layers, the neglect of energy losses of the ^{3}H and α particles should be reasonable. The probability of neutron production, P_n, for a triton of energy E_{T0} incident on a ^{3}H layer of thickness ℓ, is then

$$P_n(E_{T0}, \ell) = 2n\ell\sigma_T(E_{T0}), \tag{B.1}$$

where n is the ^{3}H number density and the factor of 2 accounts for the fact that two neutrons are emitted per reaction. Experimental data on the $^3H(^3H, 2n)$ cross section

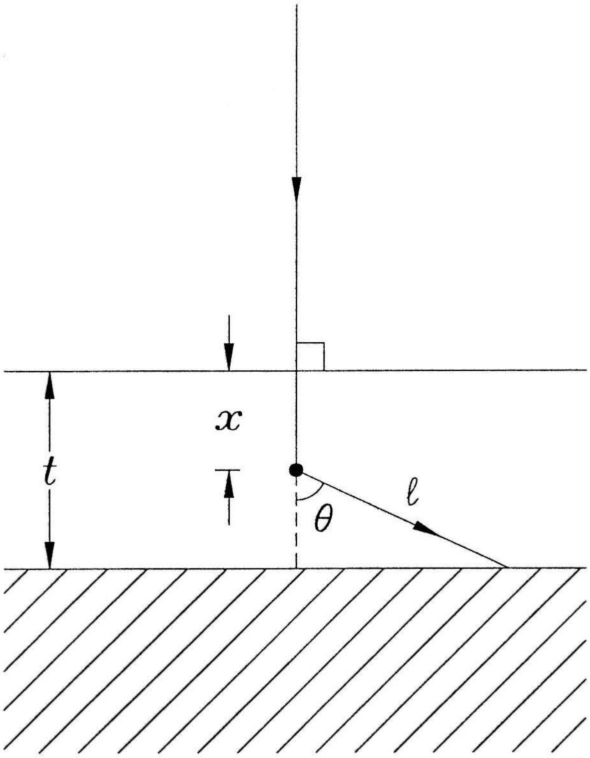

Figure B.1: Definition of variables for the normally incident case. The target is viewed perpendicular to normal.

are summarized by Typel *et al.* [Typ91]. We take the cross section to be given by

$$\sigma_T(E) = \frac{S_0}{E} exp\left(-\sqrt{\frac{E_G}{E}}\right) \tag{B.2}$$

where $E = 0.5E_T$ is center-of-mass energy, S_0 is the S-factor, and E_G is the Gamow energy (1476.6 keV for ^{3}H + ^{3}H). By choosing $S_0 = 165$ keV-b, we are able to reproduce the experimental cross sections within 20% for $E_T \leq 800$ keV.

Assuming the Rutherford formula, the differential cross section for knock-on ^{3}H scattering in the laboratory system is

$$\frac{d\sigma_{ko}}{d\Omega} = \frac{Z_T^2 Z_\alpha^2 e^4 (M_T + M_\alpha)^2}{4M_T^2 E_\alpha^2 \cos^3\theta}, \tag{B.3}$$

where Z_i and M_i are respectively the charge and mass of $i = T$ or α, e is the electronic charge, E_α is the alpha particle energy, and θ is the scattering angle with respect to the incident beam. The initial energy of the scattered triton is given by

$$E_{T0} = E_m \cos^2\theta, \tag{B.4}$$

where

$$E_m = \frac{4M_T M_\alpha}{(M_T + M_\alpha)^2} E_\alpha \tag{B.5}$$

is the maximum energy that can be transferred to the triton.

Tritons scattered at angle θ and depth x in a ^{3}H layer of thickness t, will traverse a thickness

$$\ell(x,\theta) = \frac{t - x}{\cos\theta} \tag{B.6}$$

before leaving the ^{3}H layer.

The probability of neutron production, Y_n, for an α particle of energy E_α normally incident on a ^{3}H layer of thickness t and number density n can now be evaluated:

$$Y_n = 2\pi \int_0^t n\, dx \int_0^1 dy\, \frac{d\sigma_{ko}(E_\alpha, y)}{d\Omega} P_n[E_{T0}(E_\alpha, y), \ell(x,y)], \tag{B.7}$$

where $y = \cos\theta$. Integrating over dx and changing the integration variable from y to E_T, we obtain

$$Y_n = \frac{2\pi(nt)^2 Z_T^2 Z_\alpha^2 e^4 M_\alpha^{3/2}}{(M_T + M_\alpha) M_T^{1/2} E_\alpha^{1/2}} \int_0^{E_m} \frac{\sigma_T(E_T)\, dE_T}{E_T^{5/2}}. \tag{B.8}$$

With the parameterization (B.2), the integral is elementary and we find

$$Y_n = \frac{8\pi(nt)^2 Z_T^2 Z_\alpha^2 e^4 M_\alpha^{3/2} S_0}{(M_T + M_\alpha) M_T^{1/2} E_\alpha^{1/2} (2E_G)^{5/2}} exp\left(-\sqrt{\frac{2E_G}{E_m}}\right) \sum_{k=0}^{4} \frac{4!}{k!} \left(\frac{2E_G}{E_m}\right)^{k/2}. \tag{B.9}$$

The calculated neutron yield per μC of incident beam as a function of E_α is plotted in Figure B.2, for a target with $nt = 5.52 \times 10^{17}$ ^{3}H/cm^2. Also shown is a calculation including energy losses that is described below. It is interesting to note that the yield is proportional to the *square* of the ^{3}H areal density, $(nt)^2$, as opposed to the linear dependence associated with a cross section. This proportionality will of course not be valid for targets sufficiently thick that energy losses cannot be neglected.

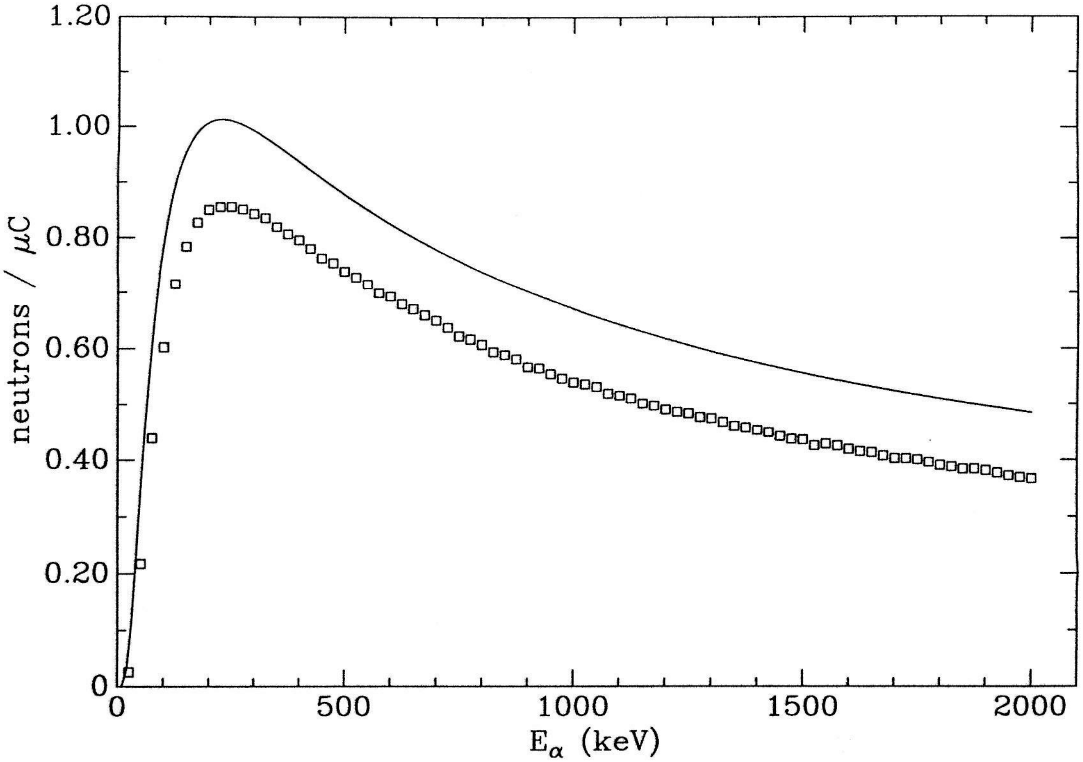

Figure B.2: The calculated neutron yield is shown as a function of the incident E_α. The solid curve corresponds to the calculation ignoring energy loss (Equation B.9), while the squares show the effect of including energy loss (Equation B.15).

B.2 Arbitrary Target Angle, Including Energy Loss

The neglect of ^{3}H energy losses is expected to have the largest effect on the neutron production in the longer trajectories. With the target normal to the incident beam, the tritons scattered $\approx$ parallel to the target plane (which have very long trajectories) correspond to $\theta \approx 90°$, and have very low energies and hence contribute little to neutron production due to the vanishing ^{3}H(^{3}H, $2n$) cross section (making the neglect of ^{3}H-energy losses a reasonable approximation).

We now consider the case when the target is tilted at an angle χ with respect to the normal direction. The geometry is displayed in Figure B.3. It is now not generally true that tritons scattered parallel to the target plane are unimportant. Let

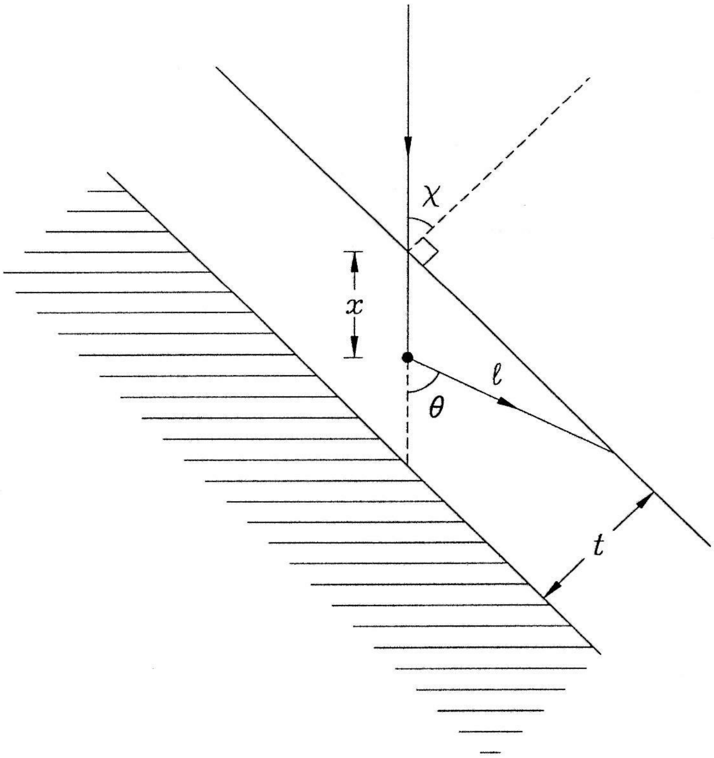

Figure B.3: Definition of variables for arbitrary angle of incidence. The target is viewed perpendicular to normal. Note that the distance ℓ is not necessarily in the plane of the paper.

us assume that the target consists of ^{3}H and Ti with $r = n(^3\mathrm{H})/n(\mathrm{Ti})$.

A more realistic calculation of P_n for a triton with incident energy E_{T0} incident on a tritium layer of thickness ℓ (compare to Equation B.1) is

$$P_n(E_{T0}, \ell) = 2 \int_0^L n\, dz\, \sigma_T[E_T(z)], \tag{B.10}$$

where L is the lesser of ℓ and the triton range. The function $E_T(z)$ is found by integrating

$$\frac{dE_T}{dz} = n[\epsilon_{\mathrm{H}}^p(E_T/3) + \frac{1}{r}\epsilon_{\mathrm{Ti}}^p(E_T/3)], \tag{B.11}$$

subject to $E_T(0) = E_{T0}$. The quantities ϵ_{H}^p and ϵ_{Ti}^p are the electronic stopping powers [Zie77] (in units of energy loss per number of target atoms per unit area) for equivalent-energy protons in hydrogen and Ti, respectively. The energy of the α

beam at depth x in the target is similarly calculated by integrating

$$\frac{dE_\alpha}{dx} = n[\epsilon_{\mathrm{H}}^{\alpha}(E_\alpha) + \frac{1}{r}\epsilon_{\mathrm{Ti}}^{\alpha}(E_\alpha)], \tag{B.12}$$

subject to $E_\alpha(0) = E_{\alpha 0}$ (the incident energy), and the quantities $\epsilon_{\mathrm{H}}^{\alpha}$ and $\epsilon_{\mathrm{Ti}}^{\alpha}$ are the electronic stopping powers [Zie77] for α's in hydrogen and Ti, respectively.

The target thickness traversed by a scattered triton now depends on the azimuthal angle ϕ, as well as the scattering angle θ, and depth x of scattering. The angle of the scattered triton with respect to the target normal is given by:

$$\cos\alpha = \cos\theta\cos\chi + \sin\theta\cos\phi\sin\chi. \tag{B.13}$$

The target thickness traversed is then

$$\ell(x,\theta,\phi) = \begin{cases} (t - x\cos\chi)/\cos\alpha & \cos\alpha > 0 \\ -x\cos\chi/\cos\alpha & \cos\alpha < 0 \end{cases} \tag{B.14}$$

where $\cos\alpha > 0$ corresponds to the case when the triton exits the target layer into the substrate, and $\cos\alpha < 0$ to the case when the triton exits from the target surface.

The neutron yield per incident α is now given by

$$Y_n = \int_0^{t/\cos\chi} n\,dx \int_0^{2\pi} d\phi \int_0^1 dy\, \frac{d\sigma_{ko}[E_\alpha(x),y]}{d\Omega} P_n[E_{T0}(E_\alpha(x),y),\ell(x,y,\phi)]. \tag{B.15}$$

The integral is evaluated using Monte Carlo techniques. The results for $nt = 5.52 \times 10^{17}$ ^{3}H/cm^2, $r = 1.89$, and the target normal to the incident beam ($\chi = 0$) are shown in Figure B.2 (these ^{3}H and Ti thickness are the values for target 1). The inclusion of energy loss is seen to decrease the calculated yield by $15 - 20\%$.

The results for $nt = 5.52 \times 10^{17}$ ^{3}H/cm^2, $r = 1.89$, and $\chi = 45°$ are shown as the solid curve in Figure B.4 (target 1 in "45-degree" target chamber). The experimental (α, n) data are shown as squares. The calculation is seen to reproduce the data very well for $E_\alpha \leq 800$ keV. The excess yield at higher energies is clearly due to

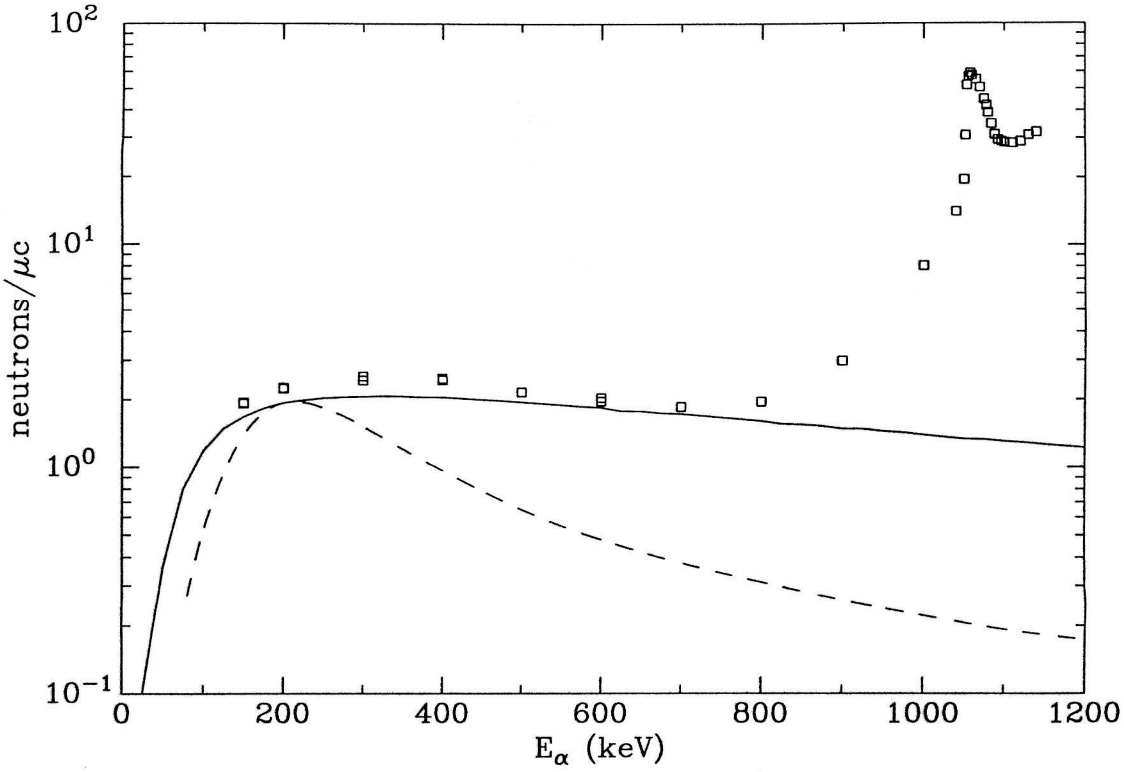

Figure B.4: The neutron yield is shown as a function of the incident E_α, with the target at 45° with respect to the incident beam. The squares are the experimental points. The solid curve is the calculation including energy loss (Equation B.15). The meaning of the dashed curve is described in the text.

the $^{13}C(\alpha, n)$ reaction, confirmed by the resonant yield seen at $E_\alpha = 1053$ keV. The dashed curve in Figure B.4 is the energy dependence expected if the neutron yield was due to $^{3}H(d, n)$ reactions from E_α-independent D_2^+ or DH_2^+ contaminants in the α^+ beam. The calculated neutron yield, for $E_\alpha = 200$ keV and $r = 1.89$, is shown as a function of target thickness in Figure B.5. The yield becomes constant for large target thicknesses due to the stoppage of all of the particles in the Ti^3H.

We have succeeded in quantitatively verifying that the neutron production for low incident α energies is due to the $^{3}H(^{3}H, 2n)$ reaction initiated by energetic tritons created by knock-on elastic α scattering. The calculation could be easily improved by including atomic and nuclear effects in the knock-on scattering cross section, and by using a more accurate representation of the $^{3}H(^{3}H, 2n)$ cross section. The inclusion of multiple scattering on the particle trajectories may also be important. Experimen-

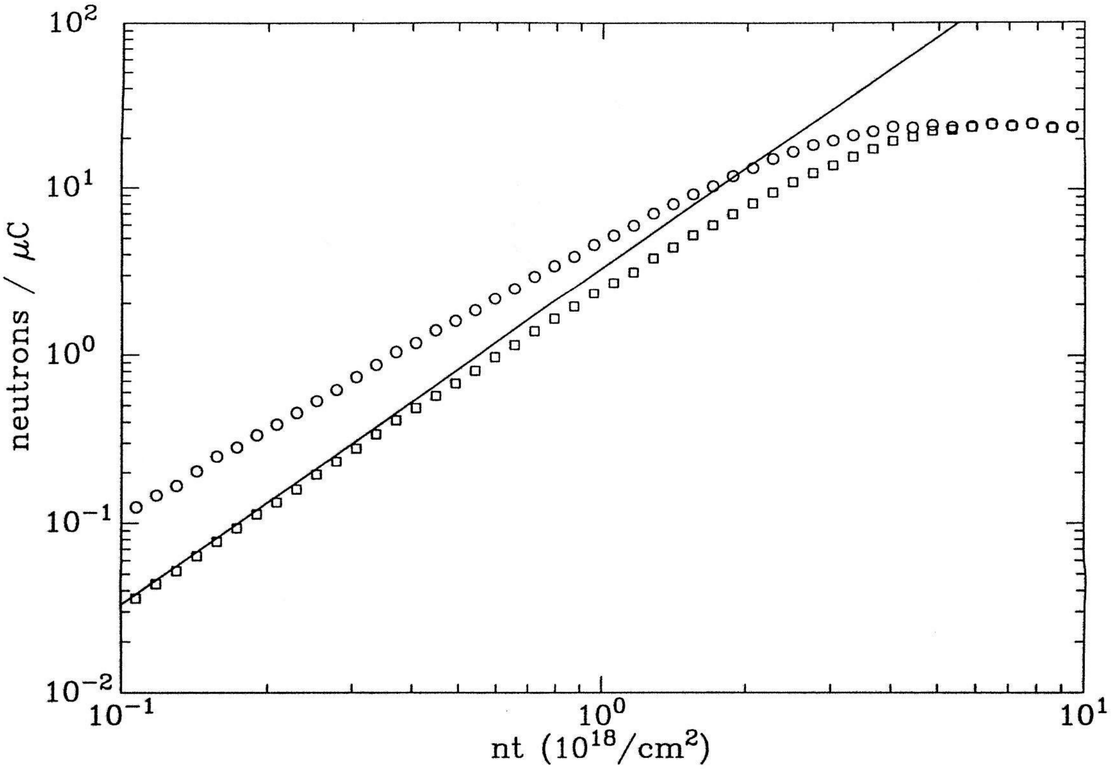

Figure B.5: The neutron yield is shown as a function of the target thickness, (nt), for $E_\alpha = 200$ keV. The squares and circles are the results using Equation B.15 for $\chi = 0°$ and $45°$, respectively. The solid curve is the result using Equation B.9 ($\chi = 0°$).

tally, the effect could be investigated by bombarding ^{2}H or ^{3}H targets with other ion beams. The effect is fundamental to any experiment using ^{3}H as a target, although it can be minimized by using a thin target [due to the proportionality to $(nt)^2$]. We note that the targets used by Griffiths *et al.* [Gri61] were $3 - 10$ times thicker than the targets used in the present experiment, so the neutron background would have been more apparent.

Appendix C

Summary of Experimental Parameters

A chronological summary of the ^{3}H(α,γ) measurements is given in this Appendix (Tables C.1, C.2, and C.3). The column labeled RUN gives the "run number" associated with each measurement. The target number and geometry (including angular position for geometry C) are given under the TAR and GEO headings, respectively. The incident α-particle energy (determined by NMR-magnetometer calibration), incident charge, and run duration are given under the E_α, Q, and Δt headings, respectively. The measured energy of the centroid of the γ_0 transition is given under $\bar{E}_{\gamma 0}$, where the number in parentheses is the statistical uncertainty in the least significant digit. The net number of counts in the γ_0, γ_1, and γ_2 peaks are given under N_0, N_1, and N_2, respectively, where the statistical uncertainties are given in parentheses.

RUN	TAR	GEO	E_α	Q	Δt	$\bar{E}_{\gamma 0}$		γ Yields	
			(keV)	(mC)	(sec)	(keV)	N_0	N_1	N_2
060	1	A	1000	9.75	1868	2919.9(2)	1054(33)	416(26)	1197(37)
061	1	A	800	12.51	1408	2827.2(2)	1145(35)	464(29)	1289(38)
062	1	A	600	15.48	2218	2735.4(2)	1018(33)	394(24)	1088(35)
063	1	A	400	33.20	3473	2645.1(2)	1047(33)	379(24)	1015(35)
064	1	A	1000	9.78	1623	2916.6(2)	1079(33)	441(27)	1120(36)
066	1	A	1600	7.50	961	3189.8(2)	1155(37)	477(29)	1268(44)
067	1	A	2000	5.15	625	3370.8(3)	873(37)	386(34)	928(59)
068	1	A	1200	7.56	1844	3007.5(2)	1000(33)	407(25)	998(35)
069	1	A	1000	9.77	1765	2916.0(2)	1085(34)	488(27)	1086(35)
070	1	A	200	292.32	20292	2554.1(2)	1019(37)	390(31)	1079(42)
071	1	A	1000	9.76	1518	2915.6(2)	1012(32)	452(26)	1109(36)
072	1	A	900	12.12	991	2869.5(2)	1151(35)	533(28)	1260(38)
073	1	A	700	14.12	1768	2778.6(2)	1065(33)	461(26)	1180(36)
074	1	A	500	24.85	2218	2687.3(2)	1081(35)	459(28)	1258(38)
075	1	A	300	81.05	5672	2597.2(2)	1115(35)	443(28)	1270(40)
076	1	A	1000	9.75	775	2914.8(2)	1124(34)	462(27)	1147(36)
077	1	A	150	617.95	33664	2530.9(3)	529(31)	227(31)	577(41)
078	1	A	1000	9.75	856	2913.6(2)	1018(33)	409(26)	1210(37)
079	1	A	250	153.07	9540	2574.8(2)	1091(36)	511(31)	1199(42)
080	1	B	1000	159.39	10527	2916.6(1)	2553(53)	1218(44)	2742(63)
083	1	B	1000	77.84	5969	2916.6(2)	1233(37)	665(32)	1298(44)
085	3	B	1000	257.76	11299	2923.1(2)	1009(33)	541(28)	996(40)
086	3	B	2000	162.07	8836	3378.6(2)	1035(39)	542(39)	966(92)
087	3	A	1000	41.03	2512	2919.2(2)	1105(34)	489(27)	1176(37)
088	3	A	700	56.77	2739	2782.4(2)	1049(33)	485(27)	1115(36)
089	3	A	500	88.43	5103	2691.4(2)	1018(33)	425(26)	1088(37)
090	3	A	900	49.14	2411	2873.4(2)	1265(36)	549(28)	1270(38)
091	3	A	1000	41.02	2031	2918.6(2)	1076(33)	471(26)	1148(37)
092	3	A	280	268.29	18739	2591.9(2)	766(33)	349(26)	884(39)
093	3	A	1000	38.83	2484	2918.3(2)	1024(33)	457(26)	1121(37)
094	3	A	1200	32.90	2266	3010.1(2)	1033(34)	441(28)	1118(39)
095	5	A	1000	15.65	3200	2926.5(2)	1080(33)	450(26)	1096(37)
096	5	A	140	782.08	41235	2534.4(1)	554(29)	248(28)	535(45)
097	5	A	1000	16.20	1126	2925.9(2)	1107(33)	419(25)	1046(34)
098	5	A	1600	12.45	961	3197.4(2)	1074(33)	423(25)	1140(36)

Table C.1: Summary of experimental parameters (see text for explanation). This Table is continued in Tables C.2 and C.3.

RUN	TAR	GEO	E_α	Q	Δt	$\bar{E}_{\gamma 0}$	γ Yields		
			(keV)	(mC)	(sec)	(keV)	N_0	N_1	N_2
099	5	B	1600	76.93	5873	3202.5(1)	1038(33)	527(25)	1073(40)
100	5	A	1600	13.10	1042	3197.2(2)	1152(35)	507(27)	1269(38)
101	5	A	2000	11.04	2190	3378.5(3)	1020(35)	407(26)	1238(44)
102	5	A	1200	14.51	1756	3017.5(2)	1126(34)	442(25)	1172(36)
103	5	A	1000	17.64	2036	2926.4(1)	1166(34)	513(27)	1251(38)
104	4	C(0)	1000	62.85	4251	2922.2(2)	1052(34)	559(29)	1170(48)
105	4	C(−45)	1000	65.76	4367	2909.5(2)	1043(34)	531(30)	1311(47)
106	4	C(−90)	1000	77.66	5064	2882.9(3)	1040(35)	473(33)	1363(53)
107	4	C(+90)	1000	79.94	4939	2883.4(3)	1157(37)	508(61)	1678(57)
108	4	C(+135)	1000	74.98	4375	2858.1(2)	1055(34)	545(36)	1474(51)
109	4	C(+135)	2000	50.65	3458	3272.7(3)	1086(34)	506(30)	1661(58)
110	4	C(0)	2000	47.38	3220	3377.2(2)	1343(39)	578(30)	1363(55)
111	4	C(−45)	2000	51.06	3347	3357.4(3)	1111(37)	577(62)	1630(54)
112	4	C(−90)	2000	58.90	3952	3314.0(3)	1028(34)	452(57)	1649(59)
113	4	C(+90)	2000	54.67	3239	3314.9(3)	1023(35)	462(58)	1980(59)
114	4	C(+90)	1600	58.95	3819	3142.5(3)	1098(36)	454(30)	1781(62)
115	4	C(+135)	1600	56.89	3773	3106.9(3)	1050(36)	473(28)	1540(57)
116	4	C(0)	1600	45.20	2722	3195.5(2)	1132(35)	568(58)	1152(47)
117	4	C(−45)	1600	51.42	3675	3179.0(3)	1042(35)	537(55)	1390(51)
118	4	C(−90)	1600	63.08	4398	3142.2(3)	1052(36)	464(29)	1469(55)
119	4	C(−90)	600	138.63	7026	2711.3(2)	1141(37)	555(36)	1264(53)
120	4	C(+90)	600	120.96	5144	2712.7(2)	1081(35)	516(34)	1352(53)
121	4	C(+135)	600	124.93	6745	2694.4(2)	1042(34)	424(32)	1218(58)
122	4	C(0)	600	131.99	6155	2740.0(2)	1367(40)	582(40)	1371(56)
123	4	C(−45)	600	117.30	4758	2731.3(2)	1069(35)	607(32)	1292(49)
124	4	C(−45)	1330	61.14	3171	3057.5(3)	1127(35)	616(52)	1468(51)
125	4	C(−90)	1330	67.07	3674	3025.0(3)	1075(34)	477(32)	1368(49)
126	4	C(+90)	1330	67.11	3313	3026.7(3)	1119(36)	533(58)	1784(54)
127	4	C(+135)	1330	62.35	4109	2996.0(2)	1085(35)	492(29)	1406(53)
128	4	C(0)	1330	54.03	2667	3072.8(2)	1218(37)	591(57)	1331(46)
129	4	C(0)	2400	37.11	3345	3561.0(2)	950(40)	470(33)	1222(59)
130	4	C(−45)	2400	42.24	3123	3536.2(3)	1011(36)	519(62)	1420(61)
131	4	C(−90)	2400	55.40	3518	3485.2(4)	1054(39)	587(69)	1639(63)
132	4	C(+90)	2400	51.88	3349	3486.9(4)	1080(38)	568(71)	1886(76)
133	4	C(+135)	2400	50.26	3364	3440.2(3)	1103(37)	609(37)	1636(67)

Table C.2: Continuation of Table C.1; continued in Table C.3.

RUN	TAR	GEO	E_α	Q	Δt	$\bar{E}_{\gamma 0}$		γ Yields	
			(keV)	(mC)	(sec)	(keV)	N_0	N_1	N_2
134	4	C(+135)	2790	45.09	3854	3601.5(3)	1080(35)	426(32)	1636(69)
135	4	C(0)	2790	41.39	2998	3737.9(2)	1199(39)	566(32)	1473(70)
136	4	C(−45)	2790	42.81	3175	3710.8(4)	1022(36)	486(68)	1453(66)
137	4	C(−90)	2790	54.38	3797	3652.8(4)	1107(36)	599(73)	1800(69)
138	4	C(+90)	2790	48.81	3509	3655.8(4)	1039(37)	528(71)	1768(94)
139	4	C(+90)	1000	80.00	3736	2884.7(3)	1075(35)	558(57)	1660(54)
140	4	C(+90)	800	86.96	4406	2799.0(3)	1063(34)	542(35)	1451(56)
141	4	C(+135)	800	98.24	3786	2776.4(2)	1109(36)	516(40)	1393(51)
142	4	C(0)	800	86.09	3038	2831.2(2)	1214(37)	635(57)	1216(49)
143	4	C(−45)	800	89.66	3228	2821.2(2)	1093(36)	570(31)	1439(49)
144	4	C(−90)	800	106.09	3768	2797.6(3)	1101(37)	570(35)	1410(49)
145	4	C(−90)	290	523.67	27348	2581.8(2)	858(40)	484(38)	999(46)
146	4	C(0)	290	514.69	22983	2601.1(2)	961(36)	490(33)	1054(46)
147	4	C(−45)	290	521.90	23692	2596.1(2)	880(41)	398(30)	1076(48)
148	4	C(+135)	290	708.95	30758	2571.8(2)	1072(38)	492(41)	1307(55)
149	4	C(+90)	290	639.70	27168	2584.0(2)	917(39)	467(41)	1044(45)
150	4	C(+90)	1000	134.93	6516	2886.6(3)	1177(37)	504(54)	1665(45)

Table C.3: Continuation of Tables C.1 and C.2.

Appendix D

Attenuation Factors

The calculated angular-distribution attenuation factors are presented in this Appendix. The photopeak attenuation factors, Q^{ϵ}_{ℓ}, and total attenuation factors, Q^{η}_{ℓ}, are shown in Figures D.1–D.3 and D.4–D.6, respectively, for geometries A, B, and C. The data points are the results from the EGS4 simulations; the error bars reflect the estimated statistical error. The solid curves are empirical fits used in subsequent data analysis.

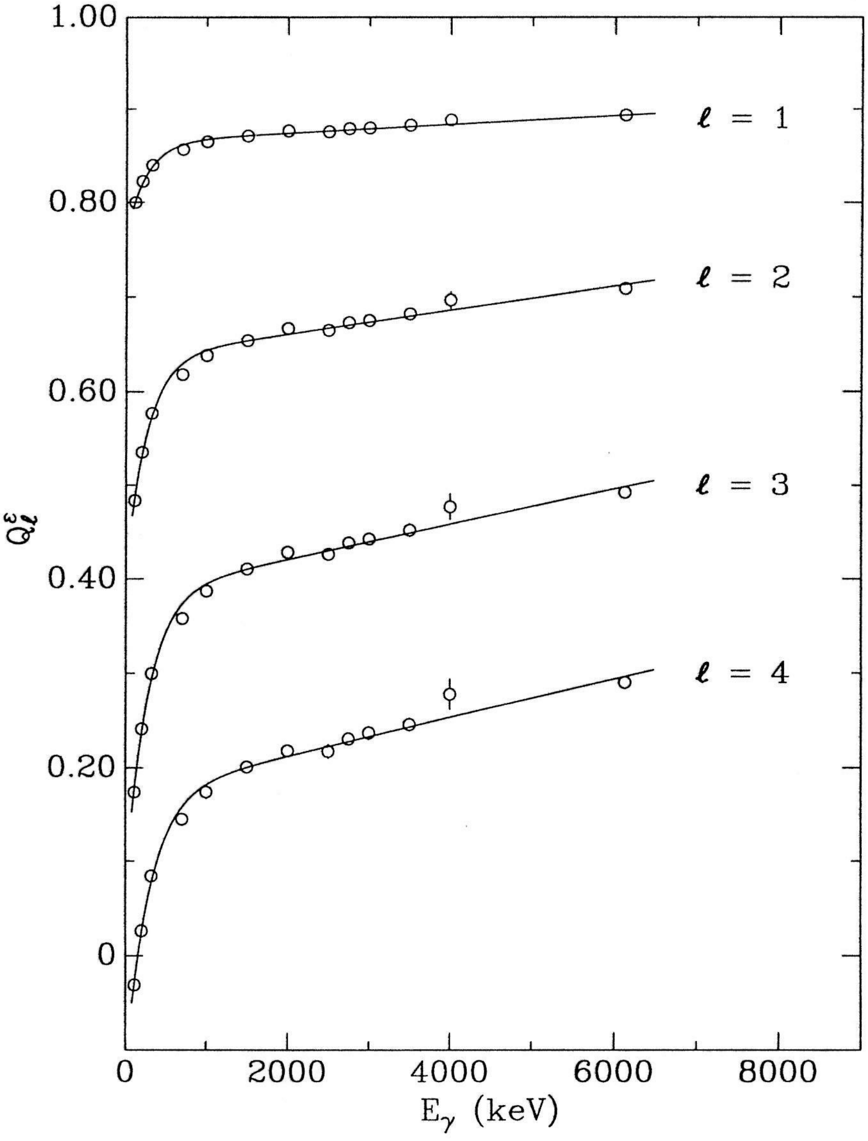

Figure D.1: Photopeak attenuation factors, geometry A.

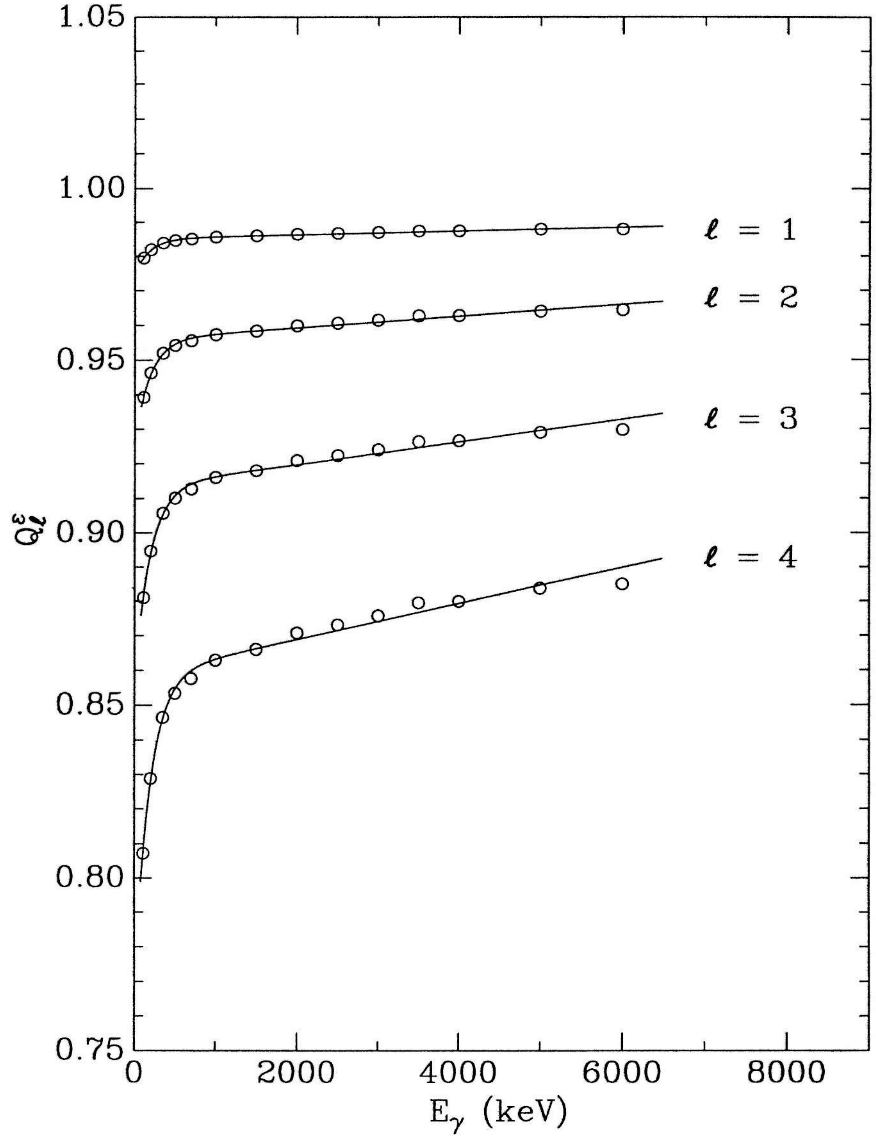

Figure D.2: Photopeak attenuation factors, geometry B.

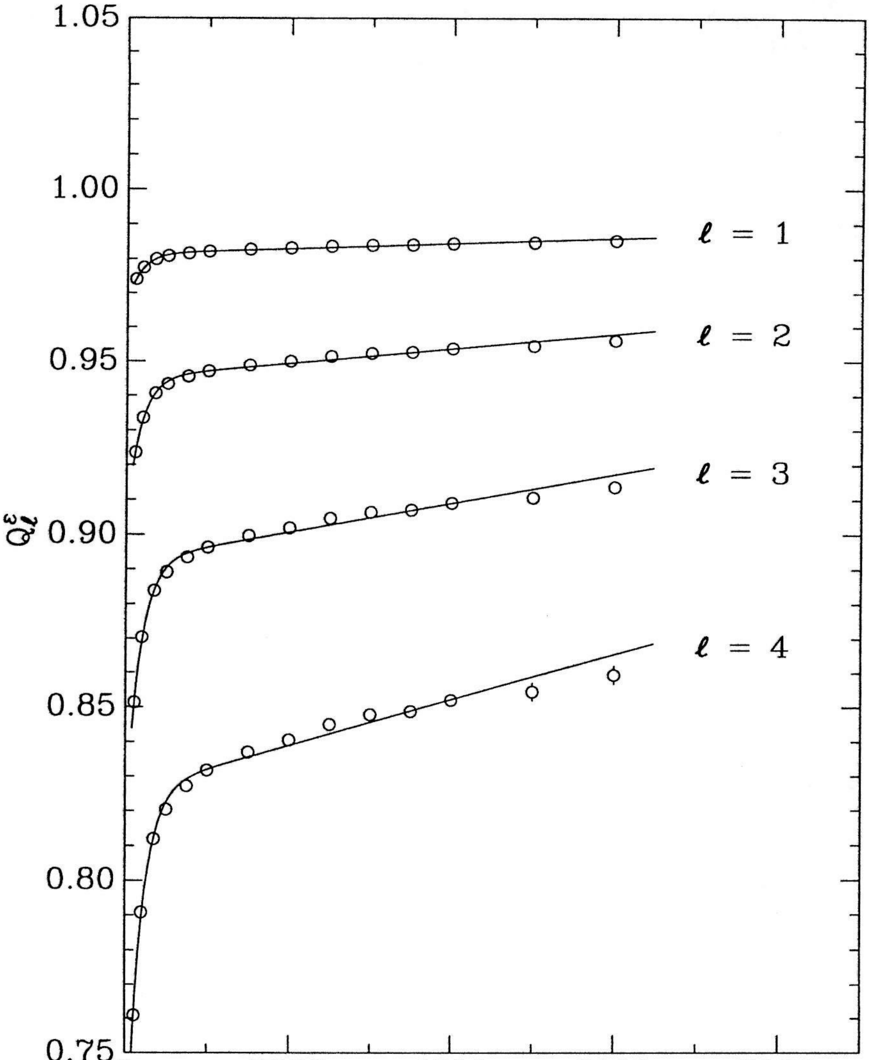

Figure D.3: Photopeak attenuation factors, geometry C.

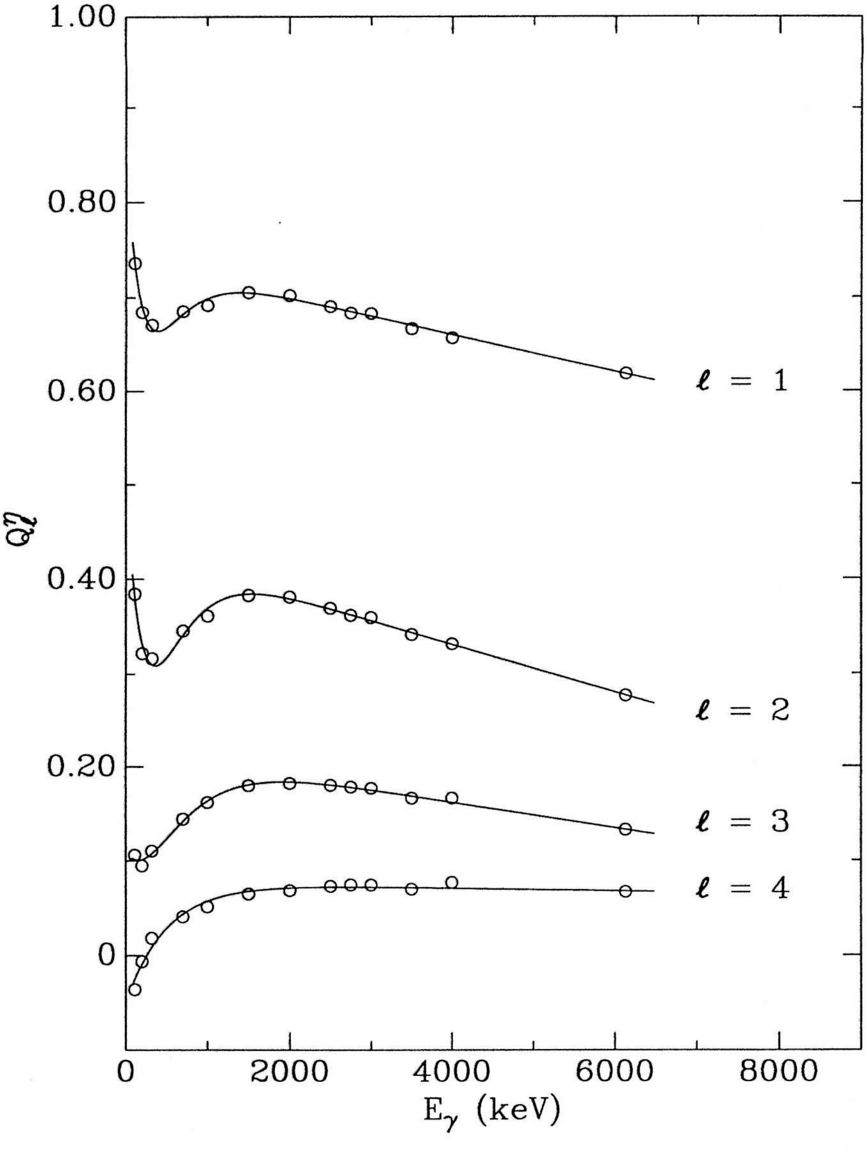

Figure D.4: Total attenuation factors, geometry A.

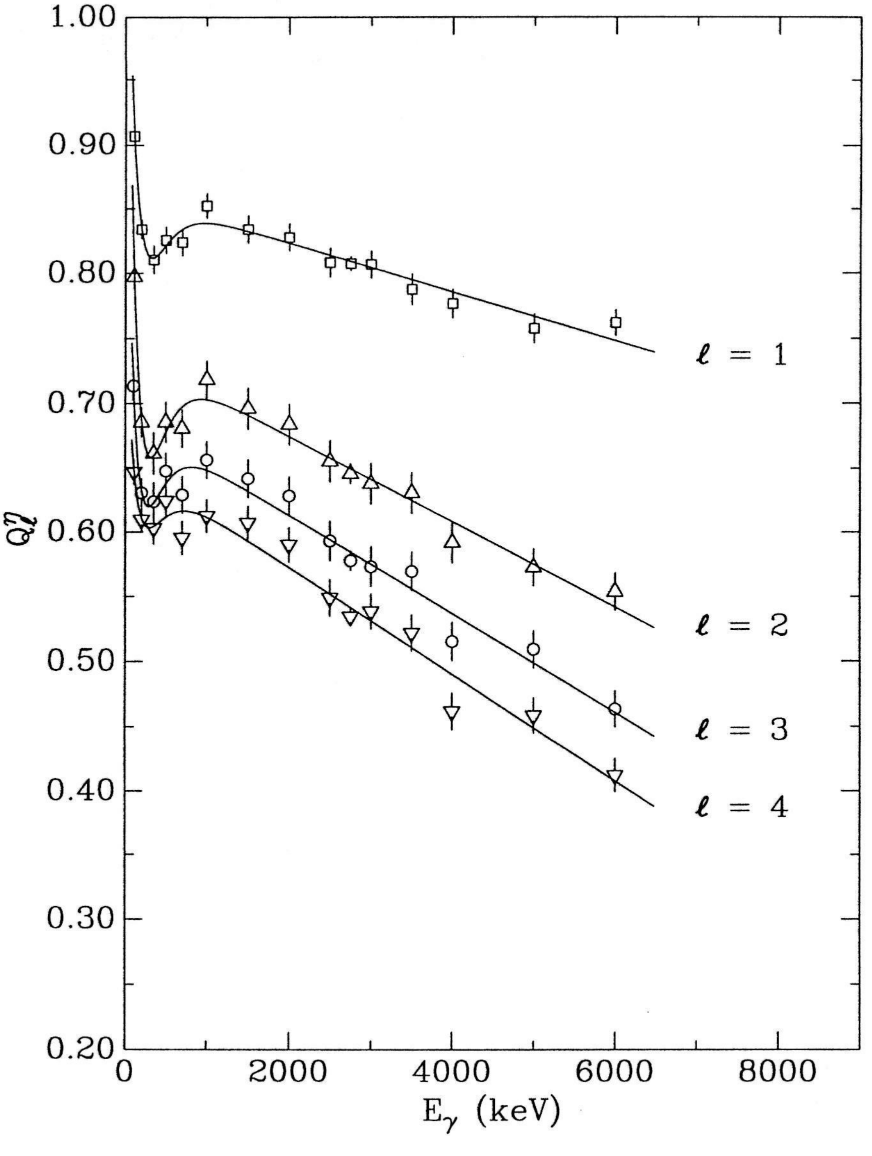

Figure D.5: Total attenuation factors, geometry B.

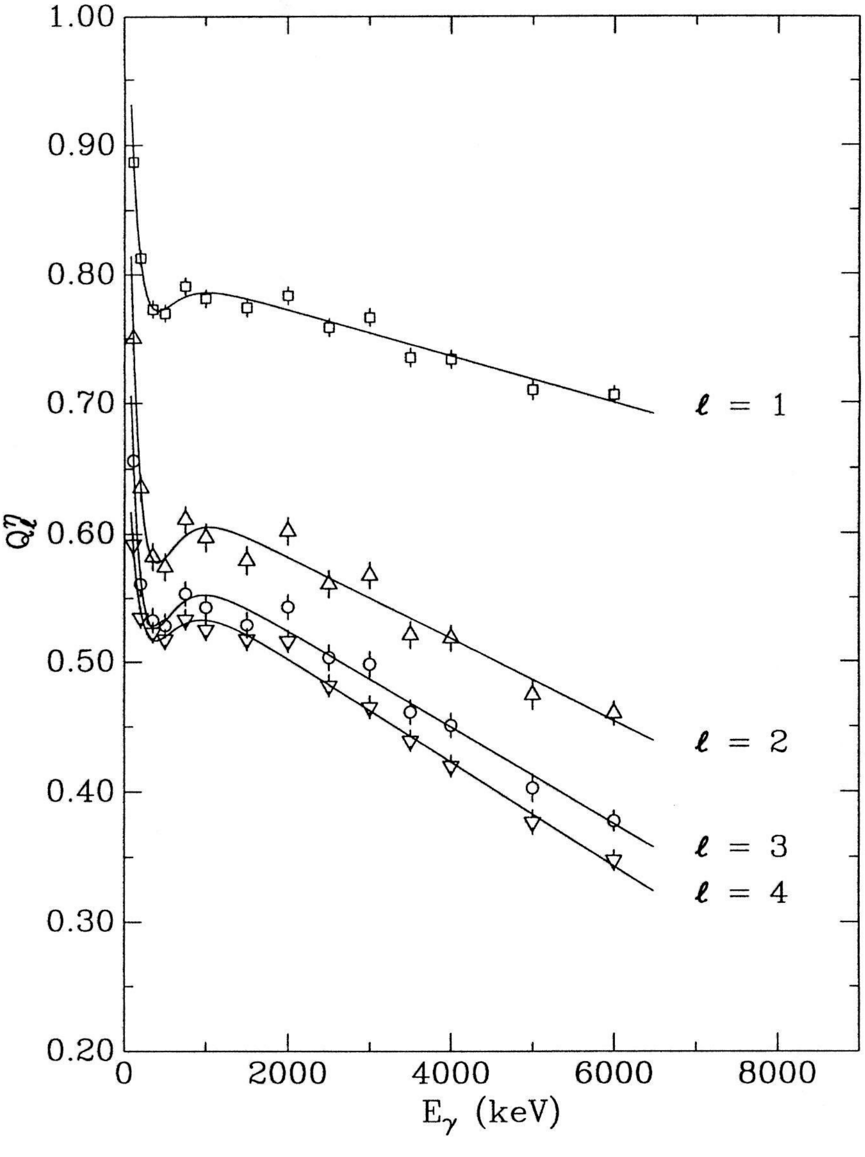

Figure D.6: Total attenuation factors, geometry C.

Appendix E

Photopeak Efficiency

The measured photopeak efficiencies for each geometry are given in this Appendix. The results for geometry A are shown in Figure E.1, for geometry B in Figure E.2, and for geometry C (at each angle) in Figures E.3–E.7. The points are the results (corrected for coincident summing effects) measured with the indicated radioactive sources. The solid curves are empirical fits used in subsequent data analysis.

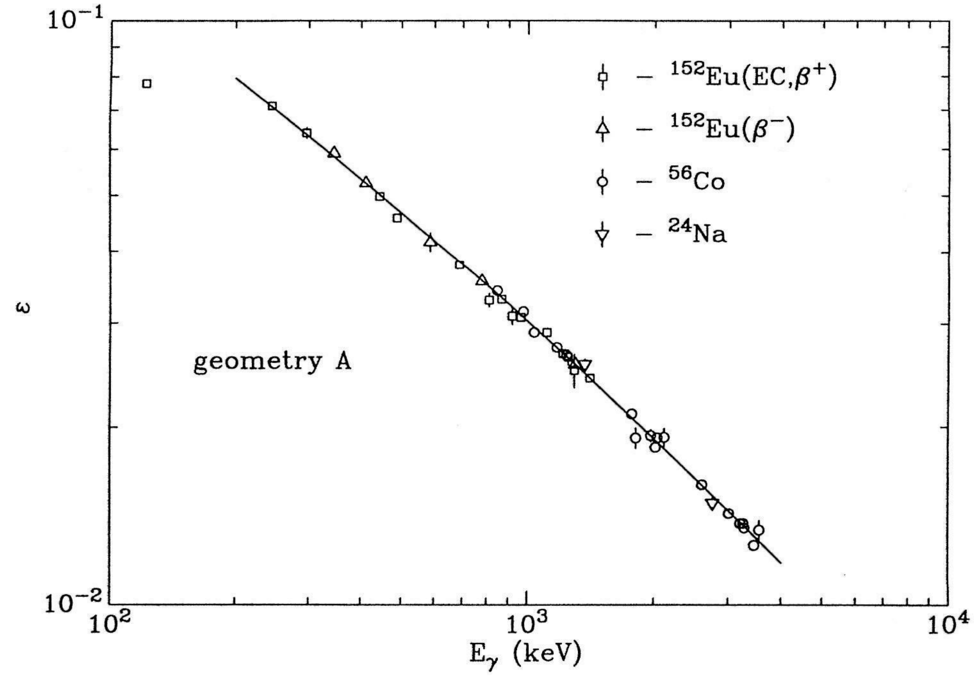

Figure E.1: Photopeak efficiency, geometry A.

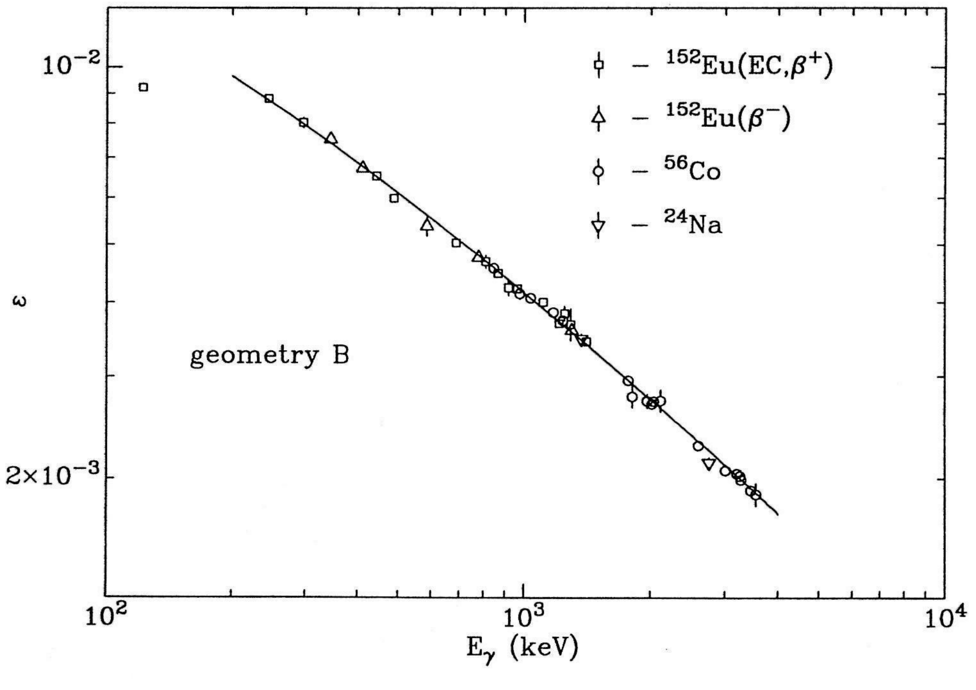

Figure E.2: Photopeak efficiency, geometry B.

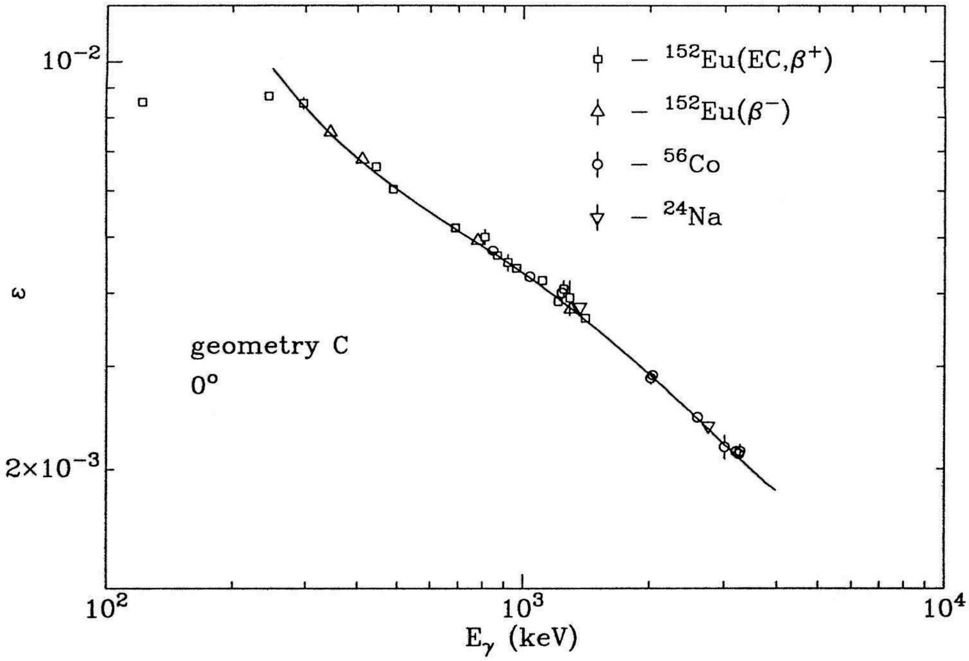

Figure E.3: Photopeak efficiency, geometry C, 0°.

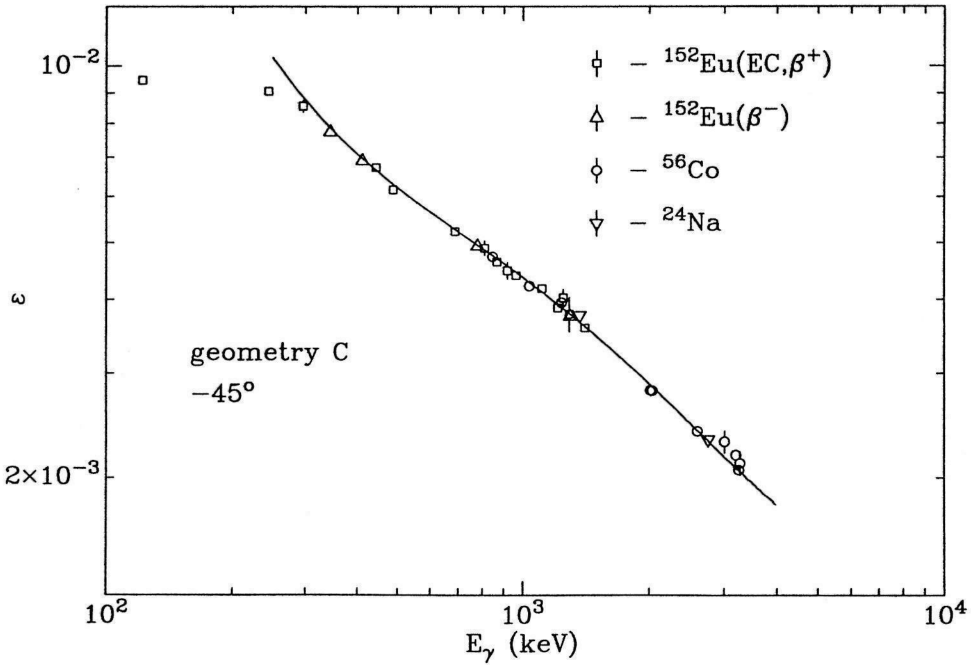

Figure E.4: Photopeak efficiency, geometry A, −45°.

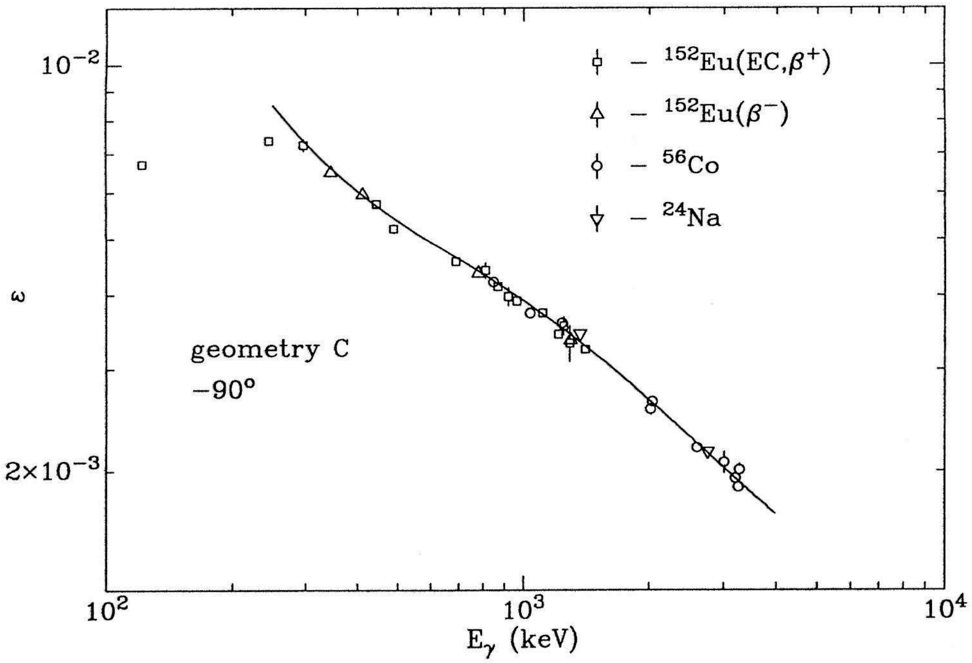

Figure E.5: Photopeak efficiency, geometry C, −90°.

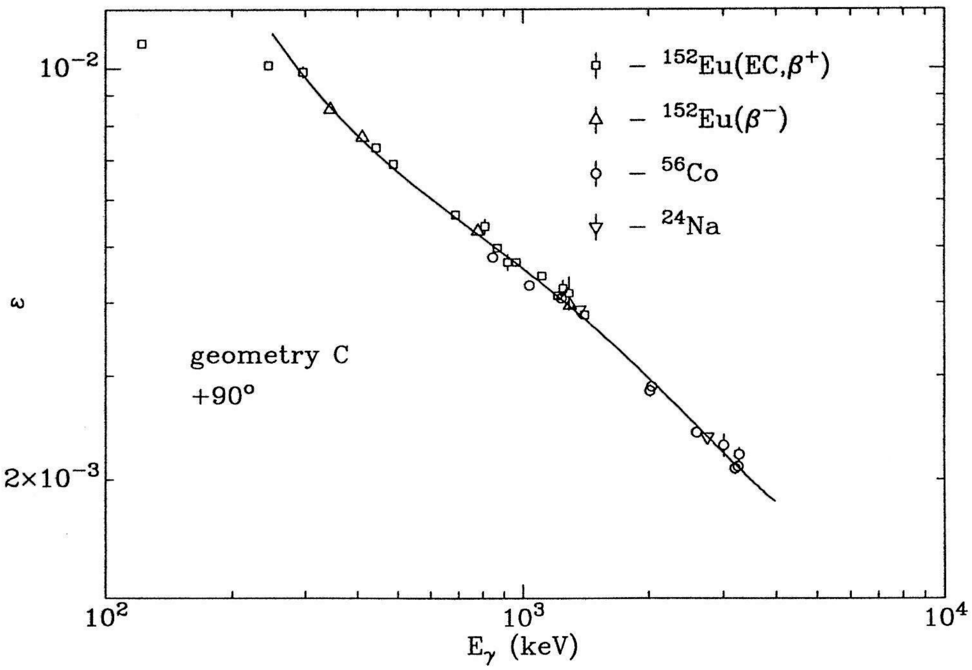

Figure E.6: Photopeak efficiency, geometry C, +90°.

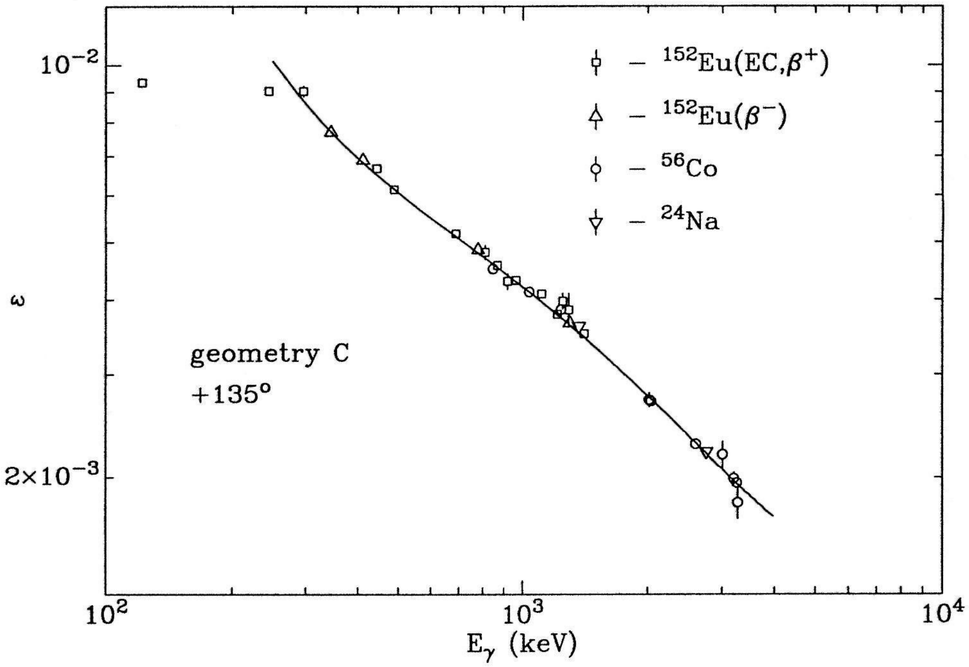

Figure E.7: Photopeak efficiency, geometry C, +135°.

Appendix F

Summary of Experimental Results

F.1 *S* and *R* From Each Run

The measured values S and R for each run are given in Tables F.1 and F.2. The run number (or range of run numbers for angular-distribution measurements) is given under the RUN heading. The "explicitly included" errors described in Subsection 4.4.3 are given in parentheses for the least significant digits of S and R. The additional systematic errors S and R are estimated to be 6% and 4%, respectively (see Table 4.2). These S data points are plotted in Figure 5.1.

RUN	E (keV)	S (keV-b)	R
060	419.3	0.0614(14)	0.461(19)
061	331.2	0.0677(15)	0.461(19)
062	244.2	0.0741(18)	0.435(19)
063	159.1	0.0795(21)	0.395(17)
064	416.1	0.0621(14)	0.434(18)
066	676.3	0.0610(15)	0.450(20)
067	848.9	0.0613(20)	0.443(29)
068	502.6	0.0622(15)	0.420(19)
069	415.6	0.0624(15)	0.431(18)
070	74.3	0.0881(42)	0.424(21)
071	415.2	0.0601(14)	0.461(20)
072	371.3	0.0623(14)	0.465(19)
073	285.1	0.0691(16)	0.461(19)
074	198.8	0.0737(19)	0.474(20)
075	114.3	0.0857(26)	0.454(19)
076	414.4	0.0658(15)	0.428(18)
077	53.2	0.0944(79)	0.444(38)
078	413.3	0.0632(17)	0.480(20)
079	93.5	0.0849(33)	0.458(21)
080	412.3	0.0631(14)	0.450(13)
083	412.4	0.0629(17)	0.460(19)
085	418.5	0.0604(15)	0.440(20)
086	850.2	0.0619(20)	0.439(30)
087	418.6	0.0636(15)	0.450(19)
088	288.7	0.0683(16)	0.453(19)
089	202.6	0.0759(19)	0.441(19)
090	375.0	0.0673(15)	0.428(16)
091	418.0	0.0621(14)	0.450(19)
092	109.4	0.0848(32)	0.473(27)
093	417.7	0.0632(15)	0.461(20)
094	505.1	0.0632(16)	0.451(20)
095	425.5	0.0646(15)	0.428(18)
096	56.4	0.0951(70)	0.413(35)
097	425.0	0.0653(19)	0.396(17)
098	683.6	0.0600(17)	0.434(18)

Table F.1: Summary of S and R for each run (see text for details). This Table is continued in Table F.2.

RUN	E (keV)	S (keV-b)	R
099	683.2	0.0614(18)	0.447(19)
100	683.3	0.0623(18)	0.458(18)
101	856.2	0.0607(19)	0.473(22)
102	512.1	0.0647(19)	0.430(17)
103	425.4	0.0659(19)	0.452(18)
104–108	416.6	0.0613(8)	0.471(11)
109–113	848.3	0.0595(9)	0.503(12)
114–118	676.0	0.0581(10)	0.472(12)
119–123	245.3	0.0708(17)	0.440(11)
124–128	559.5	0.0616(18)	0.460(11)
129–133	1021.2	0.0647(21)	0.477(13)
134–138	1189.4	0.0669(23)	0.464(13)
140–144	331.4	0.0674(27)	0.469(11)

Table F.2: Continuation of Table F.1.

F.2 Legendre Coefficients

E (keV)	a_1^0	a_2^0	a_3^0	a_1^1	a_2^1	a_3^1
116.1	0.01(5)	-0.05(9)	0.09(12)	0.06(8)	-0.28(13)	0.35(17)
245.3	0.04(3)	0.05(4)	0.06(6)	0.21(6)	0.05(9)	-0.28(11)
331.4	0.03(3)	0.06(4)	0.08(6)	0.12(7)	0.00(9)	0.10(13)
416.6	0.02(3)	0.10(4)	-0.04(6)	0.00(6)	0.26(9)	-0.10(11)
559.5	0.01(3)	0.13(4)	0.10(6)	0.10(6)	0.24(10)	-0.11(18)
676.0	0.04(3)	0.13(4)	0.10(6)	0.12(7)	0.29(9)	-0.04(21)
848.3	-0.02(3)	0.25(4)	0.10(6)	0.00(7)	0.36(13)	-0.18(19)
1021.2	-0.02(3)	0.19(4)	-0.08(7)	-0.07(7)	0.17(13)	-0.09(19)
1189.4	-0.05(3)	0.20(4)	0.05(6)	0.11(8)	-0.06(16)	0.18(24)

Table F.3: Measured γ_0 and γ_1 Legendre coefficients. The statistical errors in the least significant digits are given in parentheses. The results are displayed in Figures 5.6 and 5.7.

F.3 Final Results for S and R

E (keV)	S (keV-b)	R
55.1	0.0929(62)	0.427(26)
74.3	0.0887(42)	0.424(21)
93.5	0.0855(33)	0.458(21)
112.4	0.0855(23)	0.458(12)
159.1	0.0800(21)	0.395(17)
200.7	0.0748(14)	0.457(14)
244.8	0.0731(12)	0.439(9)
286.9	0.0687(11)	0.457(13)
331.2	0.0682(13)	0.467(10)
373.1	0.0647(10)	0.444(12)
417.4	0.0625(4)	0.448(4)
506.0	0.0626(9)	0.433(11)
559.5	0.0624(18)	0.460(11)
679.2	0.0592(6)	0.457(7)
849.8	0.0605(7)	0.484(9)
1021.2	0.0655(21)	0.477(13)
1189.4	0.0678(23)	0.463(13)

Table F.4: The final results for S and R found by combining the data in Tables F.1 and F.2. The "explicitly included" errors described in Subsection 4.4.3 are given in parentheses for the least significant digits of S and R. The additional systematic errors S and R are estimated to be 6% and 4%, respectively (see Table 4.2). These results are plotted in Figures 5.3 and 5.5.

F.4 Angular Distribution Plots

The measured γ_0 (circles) and γ_1 (squares) yields with statistical errors are plotted as a function of detector angle in Figures F.1–F.9. The results are not corrected for center-of-mass motion and finite detector size. The solid curves are the fits described in Subsection 4.4.1, used to extract the Legendre coefficients. The absolute scale of the 116-keV data (Figure F.1) is only approximate, as the data at each angle were renormalized to make the center-of-mass γ_2 yield isotropic.

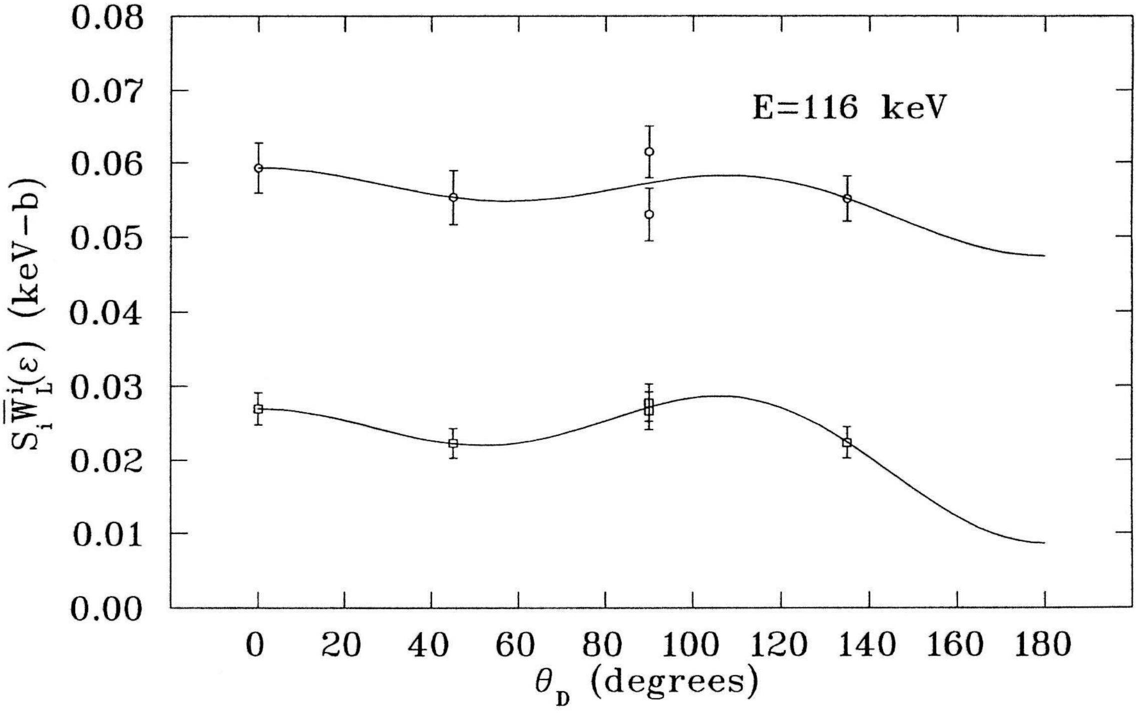

Figure F.1: $E = 116$ keV Angular Distribution.

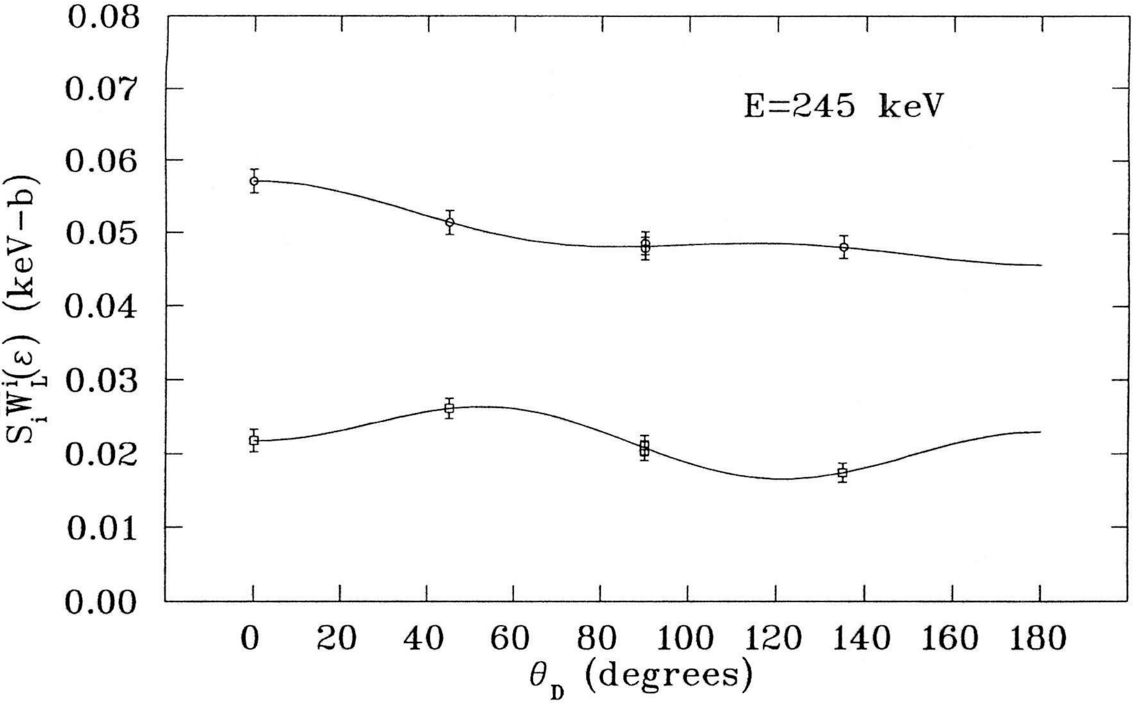

Figure F.2: E = 245 keV Angular Distribution.

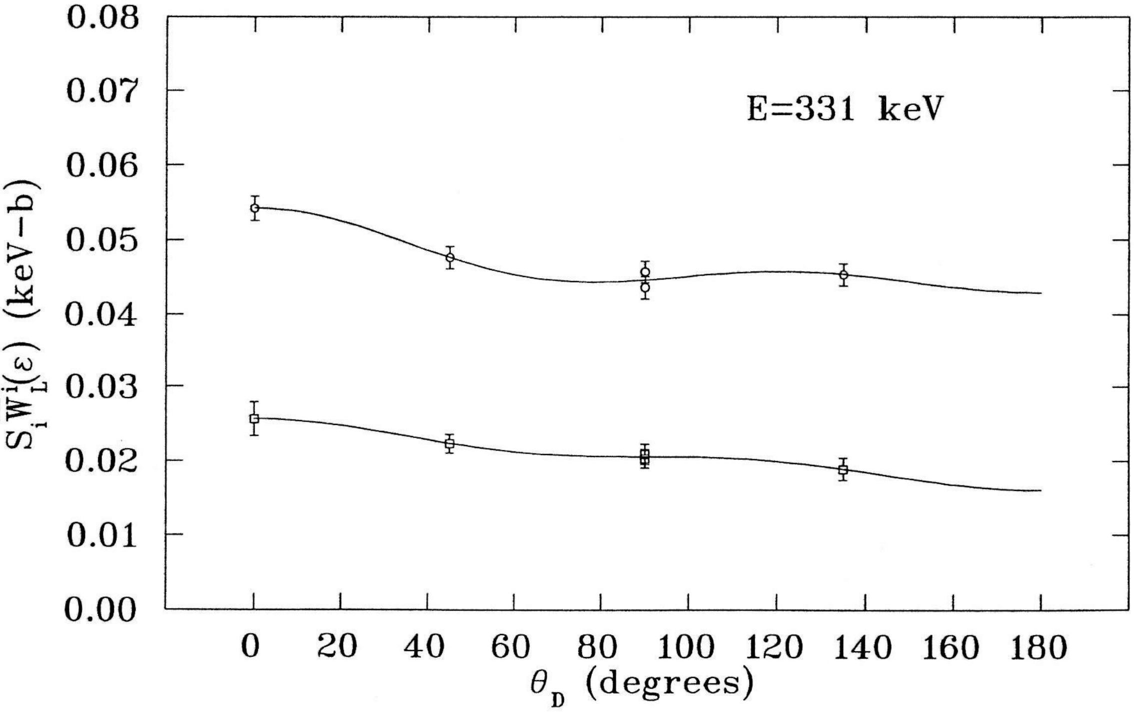

Figure F.3: E = 331 keV Angular Distribution.

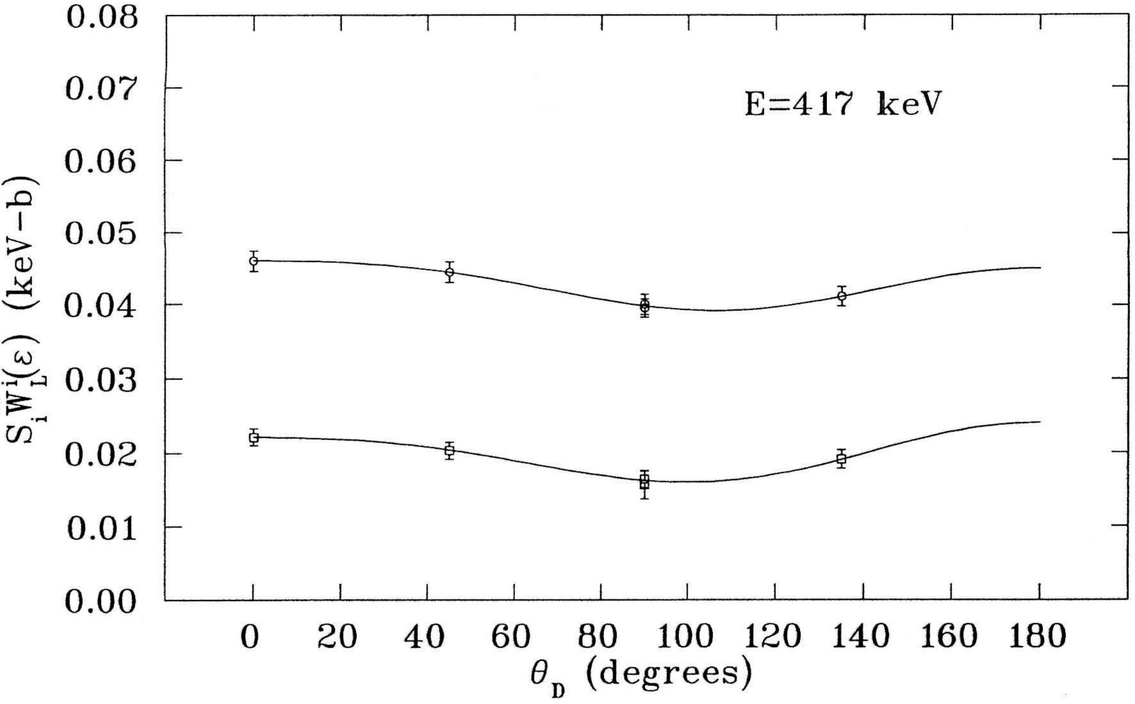

Figure F.4: $E = 417$ keV Angular Distribution.

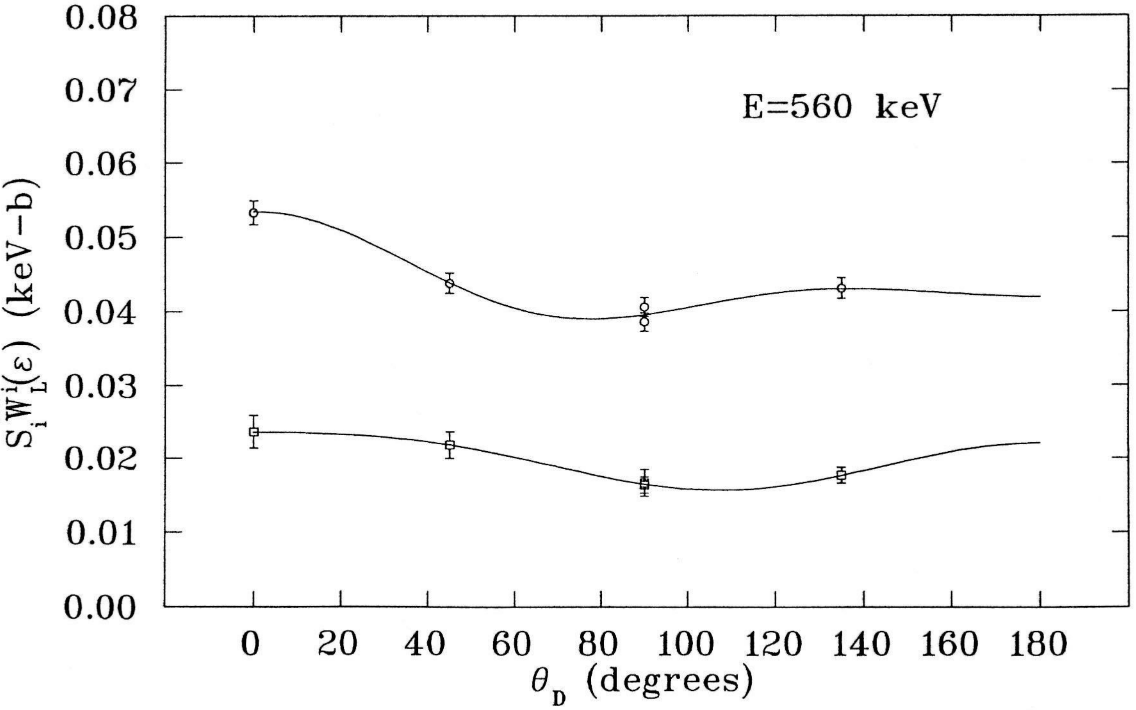

Figure F.5: $E = 560$ keV Angular Distribution.

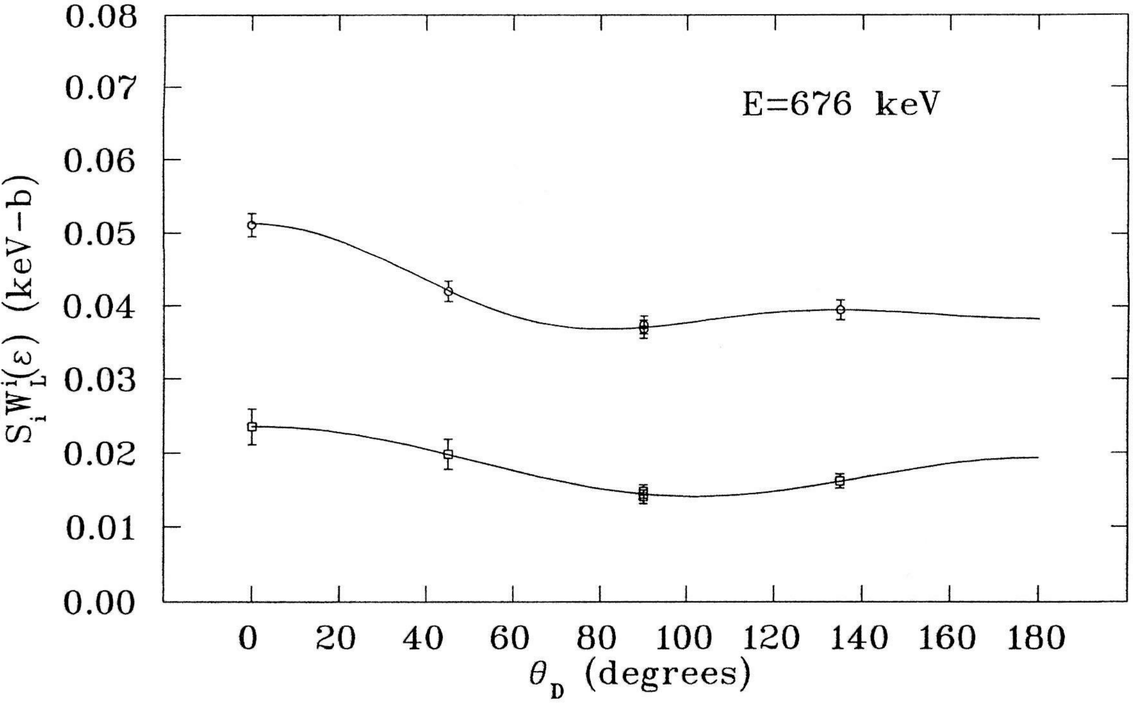

Figure F.6: E = 676 keV Angular Distribution.

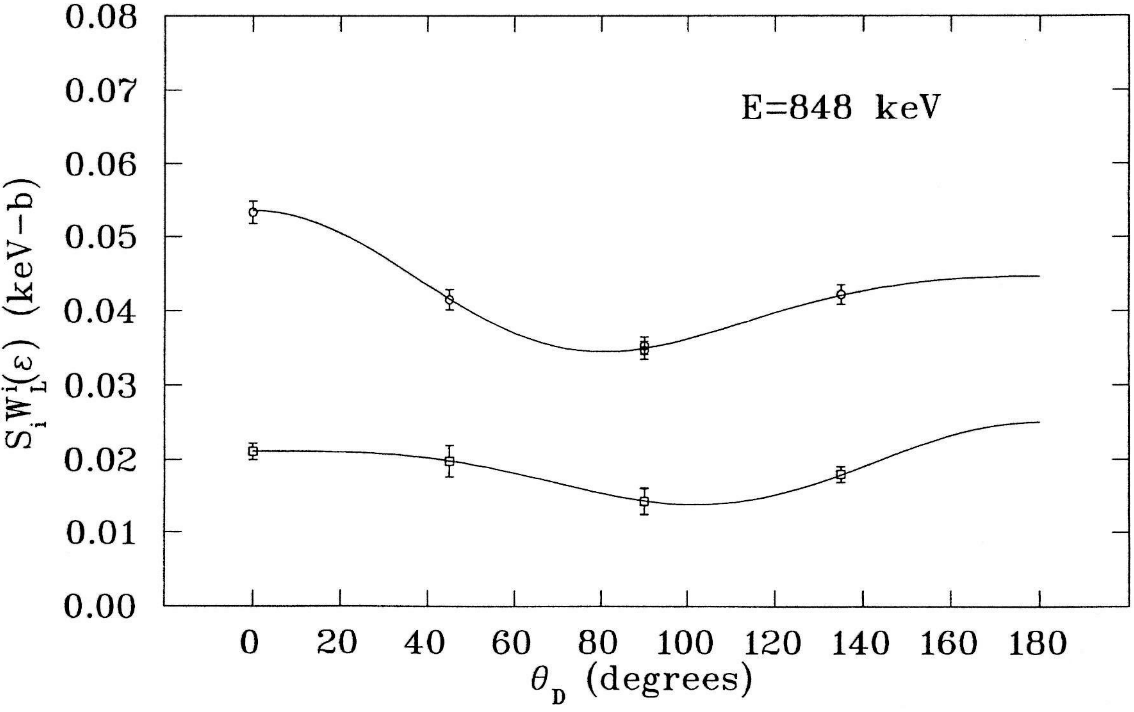

Figure F.7: E = 848 keV Angular Distribution.

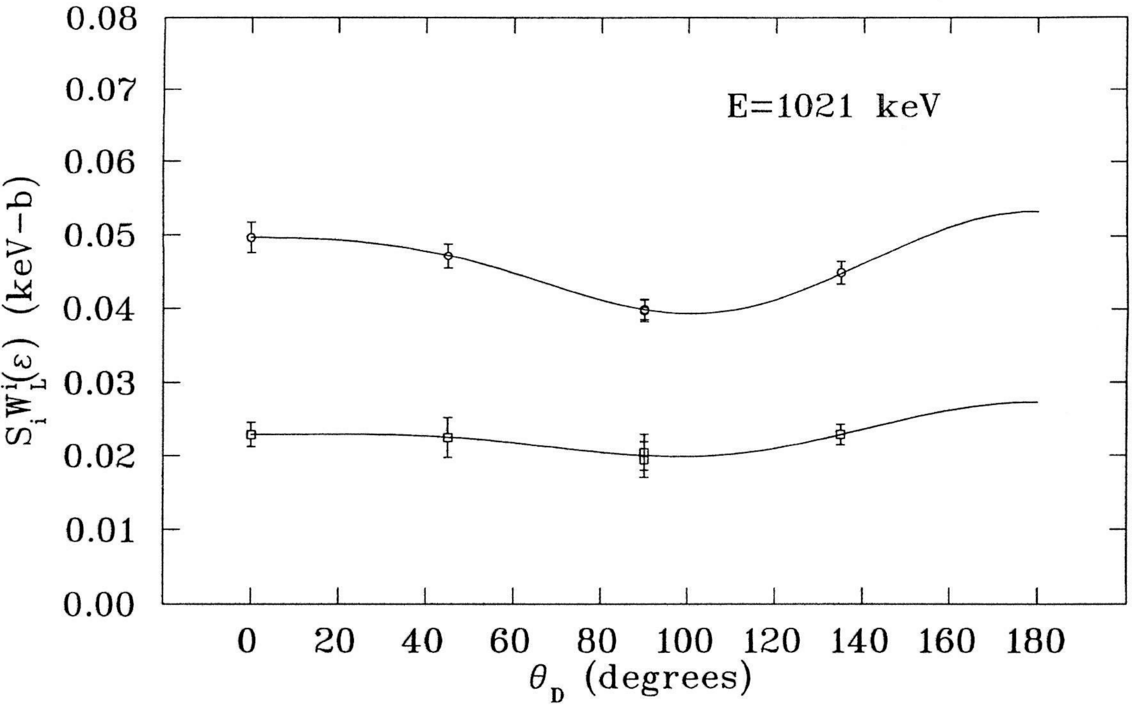

Figure F.8: $E = 1021$ keV Angular Distribution.

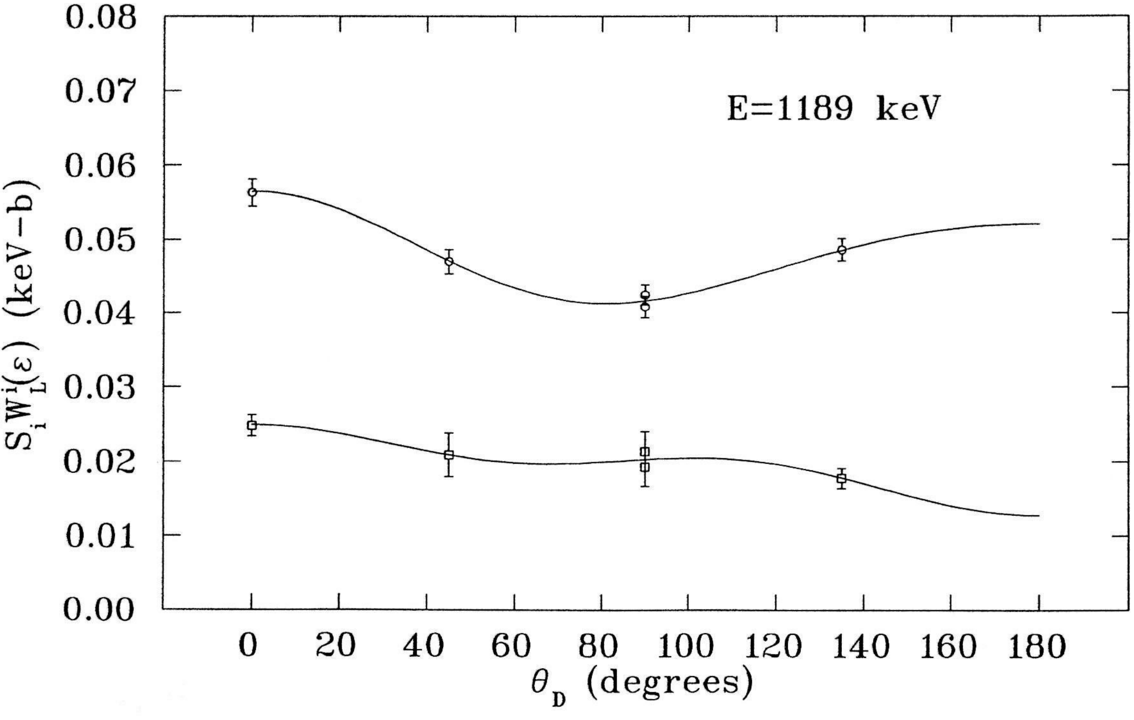

Figure F.9: $E = 1189$ keV Angular Distribution.

Bibliography

[Ajz87] F. Ajzenberg-Selove, Nucl. Phys. **A475**, 1 (1987).

[Ajz88] F. Ajzenberg-Selove, Nucl. Phys. **A490**, 1 (1988).

[All58] S. K. Allison, Rev. Mod. Phys. **30**, 1137 (1958).

[Alp48] R. A. Alpher, H. Bethe, and G. Gamow, Phys. Rev. **73**, 803 (1948).

[Alp53] R. A. Alpher, J. W. Follin, and R. C. Herman, Phys. Rev. **92**, 1347 (1953).

[Alt88] T. Altmeyer, E. Kolbe, T. Warmann, K. Langanke, and H. J. Assenbaum, Z. Phys. A **330**, 277 (1988).

[Ber90] C. A. Bertulani and M. S. Hussein, Nucl. Phys. **A524**, 306 (1990).

[Bru91] C. R. Brune, R. W. Kavanagh, S. E. Kellogg, and T. R. Wang, Phys. Rev. C **43**, 875 (1991).

[Bru92] C. R. Brune and R. W. Kavanagh, Phys. Rev. C **45**, 1382 (1992).

[Buc88] B. Buck and A. C. Merchant, J. Phys. G **14**, L211 (1988).

[Bur87] S. Burzynski, K. Czerski, A. Marcinkowski, and P. Zupranski, Nucl. Phys. **A473**, 179 (1987).

[Car90] C. Carraro, B. Q. Chen, S. Schramm, and S. E. Koonin, Phys. Rev. A **42**, 1379 (1990).

[Cau85] G. R. Caughlan, W. A. Fowler, M. J. Harris, and B. A. Zimmerman, At. Data Nucl. Data Tables **32**, 197 (1985).

[Cau88] G. R. Caughlan and W. A. Fowler, At. Data Nucl. Data Tables **40**, 283 (1988).

[Cho89] L. L. Chopovsky, Phys. Lett. B **229**, 316 (1989).

[Chr61] R. F. Christy and I. Duck, Nucl. Phys. **24**, 89 (1961).

[Con52] J. P. Conner, T. W. Bonner, and J. R. Smith, Phys. Rev. **88**, 468 (1952).

[Coo60] J. H. Coon, in *Fast Neutron Physics*, Part 1, eds. J. B. Marion and J. L. Fowler (Interscience, New York, 1960) pp. 687-700.

[Dav80] J. A. Davies and P. R. Norton, Nucl. Instrum. Methods **168**, 611 (1980).

[Del89] C. P. Deliyannis, P. Demarque, S. D. Kawaler, L. M. Krauss, and P. Romanelli, Phys. Rev. Lett. **62**, 1583 (1989).

[Del93] C. P. Deliyannis, M. H. Pinsonneault, and D. K. Duncan, Astrophys. J. **414**, 740 (1993).

[Dim88] S. Dimopoulos, R. Esmailzadeh, L. J. Hall, and G. D. Starkman, Astrophys. J. **330**, 545 (1988). Our equation is a special case of Equation (A2).

[Dro87] M. Drosg and O. Schwerer, in *Handbook on Nuclear Activation Data* (International Atomic Energy Agency, Vienna, 1987), p. 83.

[End90] P. M. Endt, Nucl. Phys. **A521**, 1 (1990).

[Esm91] R. Esmailzadeh, G. D. Starkman, and S. Dimopoulos, Astrophys. J. **378**, 504 (1991).

[Fel90] G. Feldman, M. J. Balbes, L. H. Kramer, J. Z. Williams, H. R. Weller, and D. R. Tilley, Phys. Rev. **42**, R1167 (1990).

[Fer65] A. J. Ferguson, *Angular Correlation Methods in Gamma-Ray Spectroscopy* (North-Holland, Amsterdam, 1965).

[Fow67] W. A. Fowler, G. R. Caughlan, and B. A. Zimmerman, Annu. Rev. Astron. Astrophys. **5**, 525 (1967).

[Gaz92] S. B. Gazes, J. E. Mason, R. B. Roberts, and S. G. Teichmann, Phys. Rev. Lett **68**, 150 (1992).

[Gra49] E. R. Graves, A. A. Rodrigues, M. Goldblatt, and D. I. Meyer, Rev. Sci. Inst. **20**, 579 (1949).

[Gre79] R. C. Greenwood, R. G. Helmer, and R. J. Gehrke, Nucl. Instrum. Methods **159**, 465 (1979).

[Gri61] G. M. Griffiths, R. A. Morrow, P. J. Riley, and J. B. Warren, Can. J. Phys **39**, 1307 (1961).

[Gol67] V. Ya. Golovnya, A. P. Klyucharev, B. A. Shilyaev, and N. A. Shlyakhov, Sov. J. Nucl. Phys. **4**, 547 (1967).

[Gus90] H. P. Gush, M. Halpern, and E. H. Wishnow, Phys. Rev. Lett. **65**, 537 (1990).

[Hay50] C. Hayashi, Prog. Theor. Phys. **5**, 224 (1950).

[Hol59] H. D. Holmgren and R. L. Johnston, Phys. Rev. **113**, 1556 (1959).

[Hoy64] F. Hoyle and R. J. Tayler, Nature (London) **203**, 1108 (1964).

[Iva68] M. Ivanovich, P. G. Young, and G. G. Ohlsen, Nucl. Phys. **A110**, 441 (1968).

[Iwa84] Y. Iwata, M. Yasuhara, K. Maeda, and Y. Yoshizawa, Nucl. Instrum. Methods **219**, 123 (1984).

[Jen50] B. Jennings, K. H. Sun, and H. A. Leiter, Phys. Rev. **80**, 109 (1950).

[Jun87] H. Junde, H. Dailing, Z. Chunmei, H. Xiaoling, H. Baohua, and W. Yaodong, Nucl. Data Sheets **51**, 1 (1987).

[Kaj84] T. Kajino and A. Arima, Phys. Rev. Lett. **52**, 739 (1984).

[Kaj86] T. Kajino, Nucl. Phys. **A460**, 559 (1986).

[Kaj87] T. Kajino, H. Toki, and S. M. Austin, Astrophys. J. **319**, 531 (1987); *ibid.* **327**, 1060(E) (1988).

[Kaj88a] T. Kajino, G. F. Bertsch, and K.-I. Kubo, Phys. Rev. C **37**, 512 (1988).

[Kaj88b] T. Kajino, H. Toki, K.-I. Kubo, and I. Tanihata, Phys. Lett. B **202**, 475 (1988).

[Kaj88c] T. Kajino, in *Origin and Distribution of the Elements*, edited by G. J. Mathews (World Scientific, Singapore, 1988), pp. 700-714.

[Kaj89] T. Kajino, G. J. Mathews, and K. Ikeda, Phys. Rev. C **40**, 525 (1989).

[Kaw88] L. Kawano, D. Schramm, and G. Steigman, Astrophys. J. **327**, 750 (1988).

[Kaw92] L. Kawano, Caltech preprint OAP-714 (1992); FERMILAB-PUB-92/04-A (1992).

[Kha89] P. K. Khabibullaev and B. G. Skorodumov, *Determination of Hydrogen In Materials: Nuclear Physics Methods* (Springer-Verlag, Berlin, 1989).

[Kob89] E. H. Kobisk, D. W. Ramey, W. S. Aaron, J. A. Tompkins, K. W. Haff, J. R. Devore, and H. L. Adair, Nucl. Instrum. Methods **A282**, 329 (1989).

[Kol90] E. W. Kolb and M. S. Turner, *The Early Universe* (Addison-Wesley, New York, 1990).

[Kra90] L. M. Krauss and P. Romanelli, Astrophys. J. **358**, 47 (1990).

[Lan86] K. Langanke, Nucl. Phys. **A457**, 351 (1986).

[Led78] C. M. Lederer and V. S. Shirley, *Table of Isotopes*, 7th ed. (Wiley, New York, 1978).

[Lil51] A. B. Lillie and J. P. Conner, Rev. Sci. Inst. **22**, 210 (1951).

[Liu81] Q. K. K. Liu, H. Kanada, and Y. C. Tang, Phys. Rev. C **23**, 645 (1981).

[Maa78] J. W. Maas, A. J. C. D. Holvast, A. Baghus, H. J. M. Aarts, and P. M. Endt, Nucl. Phys. **A301**, 213 (1978).

[Mal93] R. A. Malaney and G. J. Mathews, Phys. Rep. **229**, 145 (1993).

[Mas57] B. J. Massey, Oak Ridge National Laboratory Report No. ORNL-2237 (1957).

[Mer86] T. Mertelmeier and H. M. Hofmann, Nucl. Phys **A459**, 387 (1986).

[Moh93] P. Mohr, H. Abele, R. Zwiebel, G. Staudt, H. Krauss, H. Oberhummer, A. Denker, J. W. Hammer, and G. Wolf, Phys. Rev. C **48**, 1420 (1993)

[Mol80] W. Möller and F. Besenbacher, Nucl. Instrum. Methods **168**, 111 (1980).

[Nel85] W. R. Nelson, H. Hirayama, and D. W. O. Rodgers, *The EGS4 Code System*, SLAC-Report-265 (1985).

[Osb83] J. L. Osborne, Ph.D. thesis, California Institute of Technology, 1983.

[Par63] P. D. Parker and R. W. Kavanagh, Phys. Rev. **131**, 2578 (1963).

[Pau66] P. Paul, J. B. Thomas, and S. S. Hanna, Phys. Rev. **147**, 774 (1966).

[Pee66] P. J. E. Peebles, Phys. Rev. Lett. **16**, 410 (1966).

[Pek89] L. K. Peker, Nucl. Data Sheets **58**, 93 (1989).

[Pen65] A. A. Penzias and R. W. Wilson, Astrophys. J. **142**, 419 (1965).

[Per55] J. E. Perry, Jr., and S. J. Bame, Jr., Phys. Rev. **99**, 1368 (1955).

[Reb88] R. Rebolo, P. Molaro, and J. E. Beckman, Astron. Astrophys. **192**, 192 (1988).

[Ril91] S. P. Riley and J. M. Irvine, J. Phys. G **17**, 35 (1991).

[Roc52] R. S. Rochlin, Rev. Sci. Inst. **23**, 100 (1952).

[Rol91] C. Rolfs, private communication (1991).

[Ros53] M. E. Rose, Phys. Rev. **91**, 610 (1953).

[Sar82] D. G. Sargood, Phys. Rep. **93**, 61 (1982).

[Sch87] U. Schröder, A. Redder, C. Rolfs, R. E. Azuma, L. Buchmann, C. Campbell, J. D. King, and T. R. Donoghue, Phys. Lett. B **192**, 55 (1987).

[Sco59] V. D. Scott and L. W. Owen, Br. J. Appl. Phys. **10**, 91 (1959).

[Sem90] T. M. Semkow, G. Mehmood, P. P. Parekh, and M. Virgil, Nucl. Instrum Methods **A290**, 437 (1990).

[Sin59] P. P. Singh, G. M. Griffiths, Y. I. Ssu, and J. B. Warren, Can. J. Phys **37**, 866 (1959).

[Ske84] R. T. Skelton and R. W. Kavanagh, Nucl. Phys. **A414**, 141 (1984).

[Smi48] D. P. Smith, *Hydrogen in Metals* (University of Chicago Press, Chicago, 1948), p. 162.

[Smi67] D. L. E. Smith, U. K. Atomic Energy Authority Report No. AWRE 0-52/67 (1967).

[Smi93] M. S. Smith, L. H. Kawano, and R. A. Malaney, Astrophys. J., Suppl. Ser. **85**, 219 (1993).

[Spi67] R. J. Spiger and T. A. Tombrello, Phys. Rev. **163**, 964 (1967).

[Spi82] M. Spite and F. Spite, Nature (London) **297**, 483 (1982).

[Tom61] T. A. Tombrello, and G. C. Phillips, Phys. Rev. **122**, 224 (1961).

[Tom63] T. A. Tombrello and P. D. Parker, Phys. Rev. **131**, 2582 (1963).

[Trz90] W. H. Trzaska, Nucl. Instrum. Methods **A297**, 223 (1990).

[Typ91] S. Typel, G. Blüge, K. Langanke, and W. A. Fowler, Z. Phys. A **339**, 249 (1991).

[Typ93] S. Typel, in *Nuclei in the Cosmos*, edited by F. Käppeler and K. Wisshak (Institute of Physics, Bristol, 1993), pp. 323-328.

[Uts90] H. Utsunomiya, Y.-W. Lui, D. R. Haenni, H. Dejbakhsh, L. Cooke, B. K. Srivastava, W. Turmel, D. O'Kelly, R. P. Schmitt, D. Shapira, J. Gomez del Campo, A. Ray, and T. Udagawa, Phys. Rev. Lett. **65**, 847 (1990); *ibid.* **69**, 863(E) (1992).

[Wag67] R. V. Wagoner, W. A. Fowler, and F. Hoyle, Astrophys. J. **148**, 3 (1967).

[Wal91] T. P. Walker, G. Steigman, D. N. Schramm, K. A. Olive, and H.-S. Kang, Astrophys. J. **376**, 51 (1991).

[Wan91] T. R. Wang, R. B. Vogelaar, and R. W. Kavanagh, Phys. Rev. C **43**, 883 (1991); *ibid.* **44**, 1226(E) (1991).

[Wap93] A. H. Wapstra, private communication (1993).

[Wil81] R. D. Williams and S. E. Koonin, Phys. Rev. C, **23**, 2773 (1981).

[Win76] H. F. Winters, in *Radiation Effects on Solid Surfaces*, edited by M. Kaminsky (American Chemical Society, Washington, D. C., 1976), pp. 1-29.

[Wre94] P. R. Wrean, C. R. Brune, and R. W. Kavanagh, Phys. Rev. C **49**, 1205 (1994).

[Yos80] Y. Yoshizawa, Y. Iwata, T. Kaku, T. Katoh, J.-Z. Ruan, T. Kojima, and Y. Kawada, Nucl. Instrum. Methods **174**, 109 (1980).

[Zie77] J. F. Ziegler, *The Stopping and Ranges of Ions In Matter* (Pergamon, New York, 1977) Vols. 3 and 4.